



HAL
open science

Automatic segmentation and shape analysis of human hippocampus in Alzheimer's disease

Kaikai Shen

► **To cite this version:**

Kaikai Shen. Automatic segmentation and shape analysis of human hippocampus in Alzheimer's disease. Other [cs.OH]. Université de Bourgogne, 2011. English. NNT : 2011DIJOS072 . tel-00703099

HAL Id: tel-00703099

<https://theses.hal.science/tel-00703099>

Submitted on 31 May 2012

HAL is a multi-disciplinary open access archive for the deposit and dissemination of scientific research documents, whether they are published or not. The documents may come from teaching and research institutions in France or abroad, or from public or private research centers.

L'archive ouverte pluridisciplinaire **HAL**, est destinée au dépôt et à la diffusion de documents scientifiques de niveau recherche, publiés ou non, émanant des établissements d'enseignement et de recherche français ou étrangers, des laboratoires publics ou privés.

UNIVERSITE DE BOURGOGNE
U.F.R. SCIENCES ET TECHNIQUES

THESE

Présentée et soutenue publiquement pour l'obtention du grade de

Docteur de l'université

Spécialité : Instrumentation et Informatique de l'Image

par

Kai-kai SHEN

le 30 septembre 2011

Automatic Segmentation and Shape Analysis of Human Hippocampus in Alzheimer's Disease

Directeur de thèse : Professeur Fabrice Mériaudeau

Co-directeur de thèse : Dr. Pierrick Bourgeat

JURY

Rapporteurs :

RUAN, Su, Professeur, LITIS-Quantif, Université de Rouen, Rouen, FRANCE

VRAY, Didier, Professeur, CREATIS, INSA de Lyon, Villeurbanne, FRANCE

Examineurs :

RUAN Su, Professeur, Université de Rouen

VRAY Didier, Professeur, INSA Lyon

MERIAUDEAU Fabrice, Professeur, Université de Bourgogne

BOURGEAT Pierrick, Research Scientist, CSIRO, Australie

LALIGANT Olivier, Professeur, Université de Bourgogne

LANDRE Jérôme, Maître de conférences, Université de Reims

Acknowledgements

The research in this thesis is undertaken mainly with the Biomedical Imaging Group at the Australian e-Health Research Centre, CSIRO ICT Centre, Australia, in collaboration with the LE2I CNRS UMR 5158, Université de Bourgogne, France, under the direction of Prof. Fabrice Mériaudeau, and Dr. Pierrick Bourgeat.

I would like to express my great gratefulness to my family and *Doktorväter* for their unwavering support and tenacious commitment every moment during the past three years. Dr. Olivier Salvado, Group Leader of the Biomedical Imaging Group at the Australian e-Health Research Centre offered invaluable advice and generous help during my stay at his laboratory. Dr. Jurgen Fripp shared unreservedly his wisdom and insight on most problems encountered during my Ph.D. research. Present and past members at the laboratory: Dr. Oscar Acosta Tamayo, Neil Burdett, Dr. Shekhar Chandra, Dr. Tim Coles, Dave Conlan, Dr. Vincent Doré, Dr. Jason Dowling, Dr. Nicholas Dowson, Dr. Cédric Dumas, Josh Passenger, Dr. Parnesh Raniga, Dr. Hans de Visser, Dr. Di Xiao, and Dr. Luping Zhou all contributed their time and provided assistance without which the completion of this thesis would be impossible. In the most pleasant collaboration with Dr. Sébastien Ourselin, Dr. Kelvin K. Leung, and Dr. Gaël Chételat, the reward I received is more than knowledge. My thanks also go to fellow students and alumni of the laboratory: Alexandre Bilger, Erik Bonner, Juan Carlos Borda Carulla, Daan Broekhuizen, Josh Butler, Mario Cheng, Jérémy Coatelen, Dr. Olivier Comas, Zoé Dubois Dit Laroy, Quentin Duché, Amir Fazlollahi, Jean-Baptiste Fiot, Florence Gris, Aleš Neubert, Anthony Paproki, David Raffelt, William Alberto Romero Ramirez, Andrea Rueda-Olarte, Christoph Russ, Aznul Qalid Md Sabri, Pierre Schmitt, Ying Xia. I thank Luca Giancardo for providing the typesetting tools for this thesis, and my learned friends Tian-cong Chen and Wei Liu for their counsel on various topics.

The Australian Imaging, Biomarker & Lifestyle Flagship Study of Ageing (AIBL) study provided the part of the MR image data of healthy elderly subjects and Alzheimer's disease patients used in this thesis.

The hippocampal volume data used this thesis are collected and shared by the Alzheimer's Disease Neuroimaging Initiative (ADNI) (National Institutes of Health Grant U01 AG024904). ADNI data are disseminated by the Laboratory for Neuro Imaging at the University of California, Los Angeles.

Résumé

L'objectif de cette thèse est l'étude des changements de la forme de l'hippocampe due à l'atrophie causée par la maladie d'Alzheimer. Pour ce faire, des algorithmes et des méthodes ont été développés pour segmenter l'hippocampe à partir d'imagerie structurale par résonance magnétique (IRM) et pour modéliser les variations dans sa forme.

Nous avons utilisé une méthode de segmentation par propagation de multiple atlas pour la segmentation de l'hippocampe, méthode qui a été démontrée comme étant robuste dans la segmentation des structures cérébrales. Nous avons développé une méthode supervisée pour construire une base de données d'atlas spécifique à la population d'intérêt en propageant les parcellations d'une base de données génériques d'atlas. Les images correctement segmentées sont inspectées et ajoutées à la base de données d'atlas, de manière à améliorer sa capacité à segmenter de nouvelles images. Ces atlas sont évalués en termes de leur accord lors de la segmentation de nouvelles images. Comparé aux atlas génériques, les atlas spécifiques à la population d'intérêt obtiennent une plus grande concordance lors de la segmentation des images provenant de cette population.

La sélection d'atlas est utilisée pour améliorer la précision de la segmentation. La méthode classique de sélection basée sur la similarité des images est ici étendue pour prendre en compte la pertinence marginale maximale (MMR) et la régression des moindres angles (LAR). En prenant en considération la redondance parmi les atlas, des critères de diversité se montrent être plus efficace dans la sélection des atlas dans le cas où seul un nombre limité d'atlas peut-être fusionné.

A partir des hippocampes segmentés, des modèles statistiques de la forme (SSM) sont construits afin de modéliser les variations de la forme de l'hippocampe dans la population. La correspondance entre les hippocampes est établie par une optimisation d'ensemble des surfaces paramétriques. Les paramétrages sphériques des surfaces sont aplatis pour faciliter la reparamétrisation et l'interpolation. Le reparamétrage est régularisé par une contrainte de type fluide visqueux, qui est effectué à l'aide d'une implémentation basée sur la transformées en sinus discrète.

Afin d'utiliser le SSM pour décrire la forme d'une nouvelle surface hippocampique, nous avons développé un estimateur des paramètres du modèle de la forme basée sur l'espérance-maximisation de l'algorithme du plus proche voisin itéré (EM-ICP). Un terme de symétrie est inclus pour forcer une consistance entre la transformée directe et inverse entre le modèle et la forme, ce qui permet une reconstruction plus précise de la forme à partir du modèle. La connaissance a priori sur la forme modélisé par le SSM est utilisée dans l'estimation du maximum a posteriori des paramètres de forme. Cette méthode permet de forcer la continuité spatiale et éviter l'effet de sur-apprentissage.

Dans l'étude de l'hippocampe dans la maladie d'Alzheimer, nous utilisons le SSM pour modéliser le changement de forme de l'hippocampe entre les sujets sains et des patients souffrant d'Alzheimer. Nous identifions les régions touchées par l'atrophie dans la maladie d'Alzheimer en évaluant la différence entre les groupes de contrôle et ceux d'Alzheimer sur chaque point correspondant sur la surface. L'analyse des changements de la forme est restreinte aux régions présentant des différences significatives entre les groupes, ce qui a pour effet d'améliorer la discrimination basée sur l'analyse en composantes principales (ACP) du SSM. Les composantes principales décrivant la variabilité de la forme à l'intérieur des régions discriminantes ont une corrélation plus fortes avec le déclin des scores de mémoire épisodique liée à la pathologie de l'hippocampe dans la maladie d'Alzheimer.

Mots clés : imagerie médicale, analyse d'images, segmentation d'image, segmentation basée sur multiple atlas, analyse de forme, modèle de forme statistique, hippocampe, maladie d'Alzheimer

Abstract

The aim of this thesis is to investigate the shape change in hippocampus due to the atrophy in Alzheimer’s disease (AD). To this end, specific algorithms and methodologies were developed to segment the hippocampus from structural magnetic resonance (MR) images and model variations in its shape.

We use a multi-atlas based segmentation propagation approach for the segmentation of hippocampus which has been shown to obtain accurate parcellation of brain structures. We developed a supervised method to build a population specific atlas database, by propagating the parcellations from a smaller generic atlas database. Well segmented images are inspected and added to the set of atlases, such that the segmentation capability of the atlas set may be enhanced. The population specific atlases are evaluated in terms of the agreement among the propagated labels when segmenting new cases. Compared with using generic atlases, the population specific atlases obtain a higher agreement when dealing with images from the target population.

Atlas selection is used to improve segmentation accuracy. In addition to the conventional selection by image similarity ranking, atlas selection based on maximum marginal relevance (MMR) re-ranking and least angle regression (LAR) sequence are developed for atlas selection. By taking the redundancy among atlases into consideration, diversity criteria are shown to be more efficient in atlas selection which is applicable in the situation where the number of atlases to be fused is limited by the computational resources.

Given the segmented hippocampal volumes, statistical shape models (SSMs) of hippocampi are built on the samples to model the shape variation among the population. The correspondence across the training samples of hippocampi is established by a groupwise optimization of the parameterized shape surfaces. The spherical parameterization of the hippocampal surfaces are flatten to facilitate the reparameterization and interpolation. The reparameterization is regularized by viscous fluid, which is solved by a fast implementation based on discrete sine transform.

In order to use the hippocampal SSM to describe the shape of an unseen hippocampal surface, we developed a shape parameter estimator based on the expectation-maximization iterative closest points (EM-ICP) algorithm. A symmetric data term is included to achieve the inverse consistency of the transformation between the model and the shape, which gives more accurate reconstruction of the shape from the model. The shape prior modeled by the SSM is used in the maximum a posteriori estimation of the shape parameters, which is shown to enforce the smoothness and avoid the effect of over-fitting.

In the study of the hippocampus in AD, we use the SSM to model the hippocampal shape change between the healthy control subjects and patients diagnosed

with AD. We identify the regions affected by the atrophy in AD by assessing the spatial difference between the control and AD groups at each corresponding landmark. Localized shape analysis is performed on the regions exhibiting significant inter-group difference, which is shown to improve the discrimination ability of the principal component analysis (PCA) based SSM. The principal components describing the localized shape variability among the population are also shown to display stronger correlation with the decline of episodic memory scores linked to the pathology of hippocampus in AD.

Keywords : Medical Imaging, Image Analysis, Image Segmentation, multi-atlas based segmentation, Shape Analysis, Statistical Shape Model, Hippocampus, Alzheimer's Disease



TABLE DES MATIÈRES

Acknowledgements	iii
Résumé	v
Abstract	vii
1 Introduction	1
1.1 Background	2
1.1.1 Alzheimer’s disease	2
1.1.2 Hippocampus and its role in AD	6
1.1.3 MRI in AD studies	9
1.1.3.1 MRI	10
1.1.3.2 Structural MR in AD	12
1.2 Plan of the thesis	14
2 Literature Review	17
2.1 Segmentation of hippocampus in MR images	17
2.1.1 Hippocampal atlases and segmentation protocols	19
2.1.2 Survey of segmentation algorithms	23
2.1.2.1 Region growing and deformable models	23
2.1.2.2 Shape and appearance based methods	24
2.1.2.3 Atlas based methods	25
2.1.3 Evaluation of segmentation	29
2.2 Quantitative analysis of shapes	30
2.2.1 Representation of shapes	32
2.2.2 Alignment of point sets	33
2.2.3 Establishment of correspondence	35
2.2.4 Dimension reduction	37
2.3 Measuring the hippocampal atrophy	37
2.3.1 Volume measurement	38
2.3.2 Shape analysis	39
2.4 Approach adopted in this thesis	40

3	Hippocampal segmentation using multiple atlases	43
3.1	Basic version of multi-atlas based segmentation propagation	44
3.1.1	Atlas registration	45
3.1.1.1	Affine registration	46
3.1.1.2	Non-rigid registration	47
3.1.2	Similarity based atlas selection	47
3.1.2.1	Image mutual information	48
3.1.2.2	Correlation coefficient	49
3.1.3	Label fusion	50
3.2	Supervised construction of population-specific atlas	51
3.2.1	Construction of atlas set	51
3.2.2	Evaluation of atlas set	53
3.2.2.1	Entropy of probability image	54
3.2.2.2	Partial moment of histogram	55
3.3	Atlas selection by re-ranking	55
3.3.1	MMR re-ranking	56
3.3.1.1	Atlas similarity and image similarity	56
3.3.1.2	Atlas selection by MMR algorithm	57
3.3.2	Least angle regression	58
3.4	Results and discussion	60
3.4.1	Supervised atlas construction	61
3.4.1.1	Materials	61
3.4.1.2	Results	63
3.4.1.3	Discussion	63
3.4.2	Atlas selection strategies	65
3.4.2.1	Materials	65
3.4.2.2	Experimental results	66
3.4.2.3	Discussion	67
3.5	Summary	69
4	Statistical shape model of Hippocampus	71
4.1	Building the shape model	72
4.1.1	Parameterization of the shape surfaces	74
4.1.1.1	Initial parameterization by diffusion	75
4.1.1.2	Distortion minimization	76
4.1.2	Reparameterization by rotation	78
4.1.3	Groupwise optimization on shape images	80
4.1.3.1	Image representation and manipulation of shapes	81
4.1.3.2	MDL cost function and its gradient	83
4.1.3.3	Fluid regularization	85
4.1.3.4	Optimization process	87
4.1.4	Validation and evaluation of shape models	87
4.1.4.1	Compactness	90
4.1.4.2	Generalization ability	90

4.1.4.3	Specificity	90
4.2	Extrapolation of testing cases	91
4.2.1	Gaussian mixture model and EM algorithm	92
4.2.2	Estimation with symmetrical consistency and shape priors	94
4.3	Experimental results	97
4.3.1	SSM Building	97
4.3.2	SSM parameter estimation	102
4.3.3	Results and discussion	103
4.4	Summary	107
5	Quantitative shape analysis of hippocampus in AD	109
5.1	Overview of the method	110
5.2	Shape analysis using SSM	113
5.2.1	Localization step	114
5.2.2	Shape modeling step	115
5.3	Disease classification based on localized shape analysis	116
5.4	Correlating the shape variation with memory performance	119
5.5	Experimental Results	119
5.5.1	Materials	119
5.5.2	SSM	119
5.5.3	Disease classification of AD using regional SSM	121
5.5.4	Correlation of hippocampal SSM descriptors with memory scores	124
5.6	Discussion	125
5.6.1	Shape model and correspondences	125
5.6.2	Identification of atrophy affected subregions	126
5.6.3	Disease classification using SSM	128
5.6.4	Correlation analysis	132
5.7	Summary	133
6	Conclusions	137
6.1	Contributions of this thesis	137
6.1.1	Multi-atlas based segmentation	138
6.1.2	Statistical shape models	138
6.1.3	Shape analysis of hippocampus in Alzheimer's disease	139
6.2	Future works	140
6.2.1	Non-local approach to the atlas based image segmentation	140
6.2.2	Groupwise shape correspondence by optimization	140
6.2.3	Shape analysis of biological objects	141
	List of publications	143
	Bibliography	145



LISTE DES TABLES

3.1	Demographics of selected atlases	63
3.2	Entropy H_P of probability images, the bold indicates the best case in NC and AD respectively, for each structure.	64
3.3	Partial moment μ_2 of probability image histogram, the bold indicates the best case in NC and AD respectively, for each structure.	64
4.1	Accuracy of shape parameter estimation.	103
5.1	Demographic information of subjects used in the study.	120
5.2	Choices of alignment in SSMs	120



LISTE DES FIGURES

- 1.1 Cortical atrophy in Alzheimer’s brain, as compared with the normal brain. 3
- 1.2 Generation of amyloid- β from the amyloid precursor protein (APP). 4
- 1.3 Limbic system. 7
- 1.4 Coronal section of the hippocampal body after intravascular India ink injection. 8
- 1.5 A theoretical model of natural progression of cognitive and biological markers of Alzheimer disease and the sensitivity of markers to disease state. 13
- 1.6 Coronal section of Alzheimer’s brain with mild ventricular dilatation, and hippocampal atrophy. 14

- 2.1 Samples of Talairach labelings. 19
- 2.2 AAL labeling overlayed on collins27. 20
- 2.3 Delineation of hippocampus in the labelings from the Internet Brain Segmentation Repository (IBSR). 21
- 2.4 Hierarchy of shape spaces. 31
- 2.5 Tracing hippocampal volume. 38

- 3.1 Diagram demonstrating the process segmentation using multiple atlases. 46
- 3.2 Diagram demonstrating the process building a set of population specific atlases. 53
- 3.3 Least angle regression (LAR) with the first 2 covariates/atlas. . . 59
- 3.4 Probability images of hippocampus of an NC subject in AIBL data. 61
- 3.5 Comparison of result hippocampal segmentation of one example NC case by fusing 31 atlases selected according to different criteria. 65
- 3.6 The average Dice similarity coefficient (DSC) of left and right hippocampi using locally weighted voting (LWV) on the normal control (NC) atlas set with varying power of the MSD function in the atlas weight. 67

3.7	The average Dice similarity coefficient (DSC) of left and right hippocampi using locally weighted voting (LWV) on the normal control (NC) atlas set. The atlases selected by maximal marginal relevance (MMR) re-ranking. The parameter λ varies from 0.1 to 0.9. The case of $\lambda = 1$ is equivalent to the selection by NMI ranking.	68
3.8	The average Dice similarity coefficient (DSC) of left and right hippocampi using locally weighted voting (LWV) on the normal control (NC) atlas set. The atlases are selected according to image similarity ranking, maximal marginal relevance (MMR) re-ranking and least angle regression sequence.	69
4.1	Parameterizations and reparameterizations of the shape surfaces and correspondences.	73
4.2	Parameterization of quadrilateral.	78
4.3	Multi-resolution subsampling by icosahedron subdivision.	80
4.4	Cutting the octahedron and unfold to a plane.	81
4.5	The construction of a shape image, from shape to sphere to embedded octahedron to final shape image.	82
4.6	Reparameterization on the spherical parameterization and on the shape image.	83
4.7	Six possible choices of reorientation and unfolding of the octahedron.	88
4.8	The compactness of the Statistical Shape Model (SSM).	98
4.9	The behavior of the Specificity(M) in the groupwise optimization of the Statistical Shape Model (SSM), using the first $M = 15$ principal components, the number of trials in the simulation $N = 1000$	99
4.10	The descendance of Generalisability(M) in the groupwise optimization of the Statistical Shape Model (SSM), using the first $M = 15$ principal components.	100
4.11	The shape variation in the first 3 modes of the left hippocampal shape model (± 2 standard deviations).	101
4.12	The precision of the model reconstruction with the estimated shape parameter.	104
4.13	An example of reconstruction from estimated shape parameters.	105
4.14	An example of regularization on symmetric shape parameter estimation.	106
5.1	The pipeline of local shape descriptor extraction.	112
5.2	The significance map of local difference on hippocampal surface by Hotelling's T^2 test.	121
5.3	Thresholded significance map, by thresholding p -values in the significance map Figure 5.2.	122
5.4	The percentage of landmarks selected, with varying thresholds in the landmark selection on the significance map of Hotelling's T^2 test.	123
5.5	The training accuracy of the disease classification using bagged support vector machines (SVMs) with varying thresholds in the landmark selection.	124

5.6	The accuracy of the disease classification using bagged support vector machines (SVMs) with varying thresholds in the landmark selection on a separated testing set.	125
5.7	The out-of-bag (OOB) estimates of sensitivity of the disease classification using bagged support vector machines (SVMs) with varying thresholds in the landmark selection.	126
5.8	The sensitivity of the disease classification using bagged support vector machines (SVMs) with varying thresholds in the landmark selection on a separated testing set.	127
5.9	The out-of-bag (OOB) estimates of specificity of the disease classification using bagged support vector machines (SVMs) with varying thresholds in the landmark selection.	128
5.10	The specificity of the disease classification using bagged support vector machines (SVMs) with varying thresholds in the landmark selection on a separated testing set.	129
5.11	Bar plots of Spearman's ρ of the correlation between the memory indices and the principal components from each model.	130
5.12	Variation modes captured by Principal Component Analysis (PCA) on hippocampal subregions best correlated to memory indices (logical memory, AVLT, ADAS memory), color-coded map showing the magnitude of variation described by the mode.	131
5.13	Three-dimensional representation of hippocampal subfields by La Joie et al., 2010	132
5.14	The variation along the direction of mean difference between the normal control (NC) group and the Alzheimer's disease (AD) group, rigidly aligned model.	134
5.15	The variation along the direction of mean difference between the normal control (NC) group and the Alzheimer's disease (AD) group, similarity aligned model.	135

Introduction

Advancements in biomedical sciences and engineering tremendously expanded the field of view of the researchers in health care and medicine. The advent of biomedical imaging provided a unique approach to human anatomy and physiology, which would otherwise have remained under the cover. The development of neuroimaging methods in particular has abundantly enriched the knowledge about the structure, organization and function of the nervous system. In the studies into the neurological and psychiatric disorders, imaging now becomes an indispensable tool for the assessment of diseases, especially in the investigations into Alzheimer's disease (AD), which is an area where imaging techniques have been successfully applied.

Structural magnetic resonance (MR) imaging technology has been widely equipped in clinical settings. It has played an increasingly important role in the diagnosis of AD, and the early detection of the structural changes linked to the onset of the disease. Hippocampus is one of the neuroanatomical structures which suffers from the effect of the disease at an early stage, thus becomes the target of special interest in the current research. Image based measurement of hippocampal atrophy is one promising indicator for the progression of the disease. The hippocampal volume reduction, and shape changes can both be assessed from the structural MR brain images. The aim of the thesis is to develop the methodology and techniques for MR image analysis from the segmentation of MR images to the shape analysis of hippocampus which leads to better understanding of AD.

The research in this thesis is undertaken mainly with the Biomedical Imaging Group at the Australian e-Health Research Centre, CSIRO ICT Centre, Australia, in collaboration with the LE2I CNRS UMR 5158, Université de Bourgogne, France.

In the following sections of the introduction, we first introduce the background of the image analysis in AD studies, and then set forth the outline for the thesis.

1.1 Background

The image analysis methodologies developed and discussed in the scope of this thesis are mainly applied in the study of hippocampus in AD. We outline briefly the background of AD and the role of hippocampus in the disease in this section. The current developments in the neuroimaging investigations into the disease are also introduced.

1.1.1 Alzheimer's disease

Alzheimer's disease is a progressive neurodegenerative disorder, characterized by the loss of memory, cognitive deterioration, impairment of independent living ability, and other psychosocial and behavior symptoms. The term was first introduced in Emil Kraepelin's psychiatry textbook (1910), originally limited to the presenile dementia. Now this distinction is no longer recommended, since the majority of senile dementia is found to be caused by similar, or identical pathological changes in the presenile condition (Roth et al., 1966; Blessed et al., 1968; Tomlinson et al., 1968, 1970; Hachinski et al., 1974). Approximately 60 to 80% of cases of dementia among the elderly population are caused by AD (Alzheimer's Association, 2011), which is to be differentiated from other forms of dementia, such as vascular dementia, Lewy body dementia, frontotemporal dementia, dementia caused by Parkinson's disease among others.

With aging being the main risk factor of the disease, the probability of being affected doubles every 5 years after the age of 65. It becomes a major public

health problem as the population ages, and the cost of caring increases. The *World Alzheimer Report 2010* (Wimo and Prince, 2010) estimated the global prevalence of 35.6 million people affected by the Alzheimer's disease and other forms of dementia in 2010, and predicted the number to double every twenty years, to 65.7 million by 2030 and 115.4 million by 2050. In France, the prevalence of dementia is estimated to be 754 000 people in 2010, and would rise to 1.8 million in 2050 (Mura et al., 2010).



FIGURE 1.1: Cortical atrophy in Alzheimer's brain (right), as compared with the normal brain (left). Image source: Pathology Education Instructional Resource (PEIR) Digital Library (Pathology image database). © Dr. Peter Anderson, University of Alabama at Birmingham, Department of Pathology.

The knowledge about the disease has been greatly advanced since Dr. Alois Alzheimer (1864–1915) first described his eponymous condition in 1906 (Alzheimer, 1911). The patient, Auguste D, with dementia symptoms, was 51 years old when admitted by Alzheimer (For an account of the case see Maurer et al., 1997). The necropsy revealed neuritic plaques, neurofibrillary tangles, which are now recognized as the hallmarks of the AD. The main component of the plaque has been

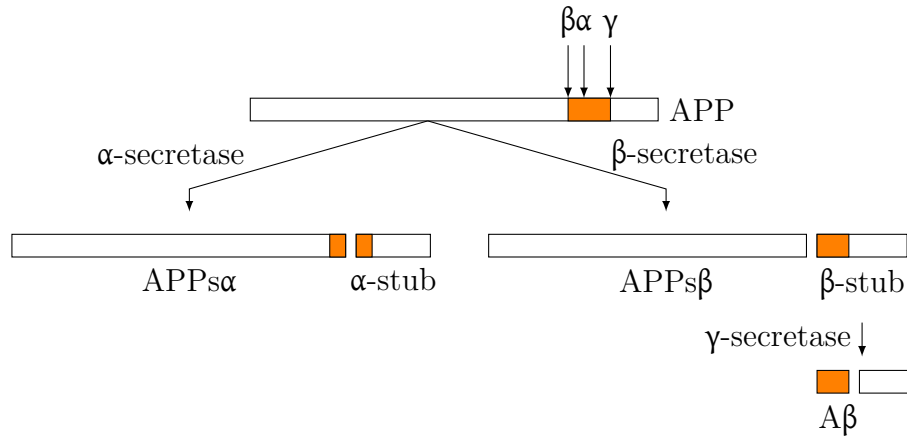


FIGURE 1.2: Generation of amyloid- β from the amyloid precursor protein (APP). Adapted from Goedert and Spillantini (2006).

identified to be amyloid- β (A β), and the tangle is made of tau. The current amyloid cascade hypothesis suggests the disease is caused by excessive deposition of A β which will be briefly summarized as follows (for an up-to-date review of the current development in the pathogenesis and related issues of Alzheimer's disease, see Blennow et al., 2006; Goedert and Spillantini, 2006; Murphy and LeVine, 2010; Ballard et al., 2011).

Amyloid- β is the secreted peptide of 40 or 42 amino acids from larger transmembrane amyloid precursor protein (APP), with the physiological function still unknown. During the amyloidogenic cleavage, APP is processed by β - and γ -secretase subsequently, releasing A β peptide. In the alternative pathway, APP is cleaved by α -secretase within the A β domain first, which is therefore non-amyloidogenic. The A β product is degraded and cleared in normal metabolism. Observing in the familial Alzheimer's disease that the mutations in the *APP* gene causes preference of β -secretase, and that the mutations in *presenilin* genes associated with the secretase enzymes increase the production of A β_{42} , being more ready to aggregate to plaque, the current amyloid cascade hypothesis suggests that synaptic dysfunction and neuronal death are triggered by the A β deposition and oligomers aggregated from A β . In sporadic AD, the $\epsilon 4$ allele of apolipoprotein E (*APOE- $\epsilon 4$*) associated with the failure of A β clearance has been identified as the main genetic factor that increases the risk of AD 3.8 times (Alzgene database, see Bertram et al., 2007).

The intracellular neurofibrillary tangle is composed of the hyperphosphorylated tau. Tau is a microtubule-associated protein, which promotes tubulin assembly and microtubule stability. The abnormal hyperphosphorylation of tau leads to the disassembly of microtubules inhibiting and disrupting the axonal transport. The aggregation of tau into paired helical filaments forms the neurofibrillary tangles. As the consequence, neuronal and synaptic function is impaired with neurotransmitter deficit, and the growth of tangles results in the neuron death. According to the amyloid cascade hypothesis, the alternation in tau and the tangle formation result from the A β deposition, though the link between A β and tau is still not fully understood.

The load of plaque and tangles starts to accumulate before the clinical onset of the AD. Non-demented patients in the transitional stage with memory complaints are usually diagnosed with mild cognitive impairment (MCI), which is a heterogeneous entity including memory decline due to normal aging, or prodrome of other forms of dementia and disorders. Approximately 10–15% of the MCI cases convert into AD every year, while the rate is 1–2% in general population (Petersen et al., 1999).

In research and clinical practices, the diagnosis of the disease commonly follows the criteria of ‘probable’ AD developed by National Institute of Neurological and Communicative Disorders and Stroke and the Alzheimer’s Disease and Related Disorders Association (NINCDS-ADRDA, McKhann et al., 1984), and that of *Statistical Manual of Mental Disorders, Fourth Edition* (DSM-IV, American Psychiatric Association, 1994; *Text Revision*, DSM-IV-TR, American Psychiatric Association and Task Force on DSM-IV, 2000). The definitive diagnosis requires *post mortem* histopathological examination. Revisions of the NINCDS-ADRDA have been proposed to keep it update with new findings in the biomarkers, and the growth of knowledge about the disease since its first publication, especially the advancement in the neuroimaging with structural MRI, molecular imaging with PET, and cerebrospinal fluid analysis of A β and tau (Dubois et al., 2007).

1.1.2 Hippocampus and its role in AD

Hippocampus has been the subject of particular interests to physiologists and neuroscientists due to its role in the memory, as well as its involvement in the neurological disorders such as AD and epilepsy. Information concerning its function and anatomy maybe found in texts and reference works on neurology and neuroanatomy of the subject (Duvernoy, 2005; Andersen et al., 2006; Taupin, 2008). Hippocampal formation, including hippocampus proper (also known as *cornu Ammonis*¹, CA), subiculum, and dentate gyrus, is located in the limbic lobe on the medial aspect of the hemisected brain. It belongs to the most primitive archicortex of the cerebral cortex. In the description by Santiago Ramón y Cajal (1911; for English translations, see Ramón y Cajal, 1995, also Ramón y Cajal, 1968), the hippocampal proper is stratified into alveus, stratum oriens, stratum pyramidale, stratum radiatum, stratum lacunosum, and stratum moleculare, which are usually grouped into three archicortical layers, viz. molecular (stratum radiatum, stratum lacunosum and stratum moleculare), pyramidal (stratum pyramidale), and polymorphic layers (stratum oriens), from deep to superficial, with ventricular surface covered by the alveus.

Based on the cell morphology, Lorente de Nó (1934) divided the hippocampus proper into 4 subfields, namely CA1–4 (see Figure 1.4). CA1, extending from subiculum, is the largest subfield, characterized by pyramidal cells with triangular cell body, in contrast to larger and ovoid cell bodies in CA2 and CA3. CA1 is also known as the ‘vulnerable sector’ or Sommer’s sector, because of its inordinate sensitivity to ischemia and hypoxia, while CA3 as the ‘resistant sector’ or Spielmeyer sector. CA2 is a narrow region between CA1 and CA3, of which the characterization and the distinct existence have been subject to discussion, while now can be distinguished by molecular and genetic criteria (Lein et al., 2005; Mercer et al., 2007). The CA4 subfield originally described by Lorente de Nó is the polymorphic layer of the dentate gyrus, consisting of interneurons.

¹Latin for ‘Ammon’s horn’, after the Egyptian deity *imn* ‘Ammon’.

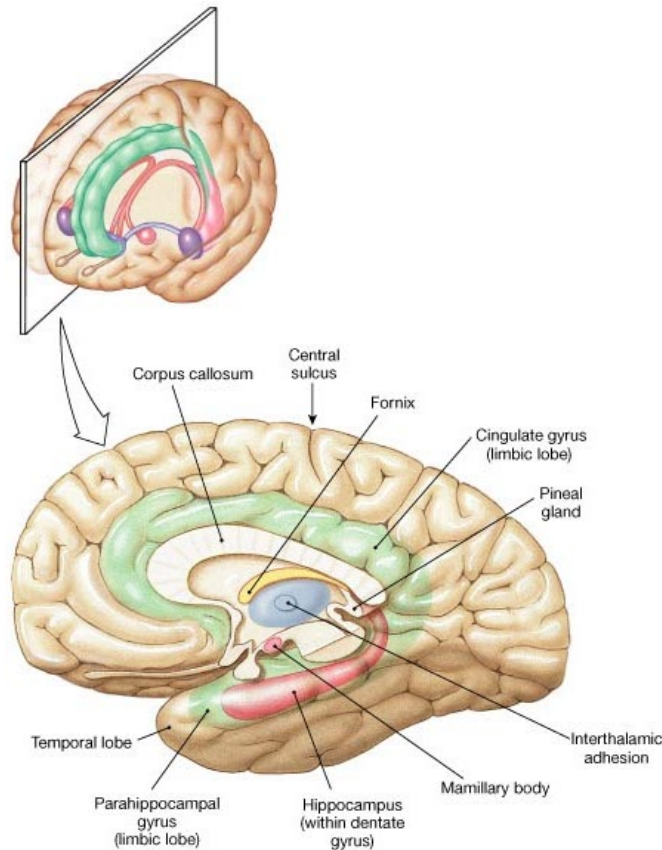


FIGURE 1.3: Limbic system, location of hippocampus (red), medial view. Image source: Martini et al. (2002).

The dentate gyrus consists of a superficial molecular, the granular in the middle, and the polymorphic being the deepest. The subiculum is connected to the three layers of the hippocampus proper, while develops into a six-layered structure to the end close to the parahippocampal neocortex.

Hippocampus is accessed by the association areas of cortex through the entorhinal cortex, which provides the major input to the hippocampal formation. Other afferents to the hippocampus include indusium griseum, cingulate gyrus, spetal nuclei, and parahippocampal gyrus. The efferent fibers carrying the principal output from hippocampus follow the fiber through the alveus, fimbria and fornix. The two contralateral hippocampi on each hemisphere are interconnected by fornix commissure. A full description of the synaptic organization of the hippocampus is provided by Johnston and Amaral (1997).

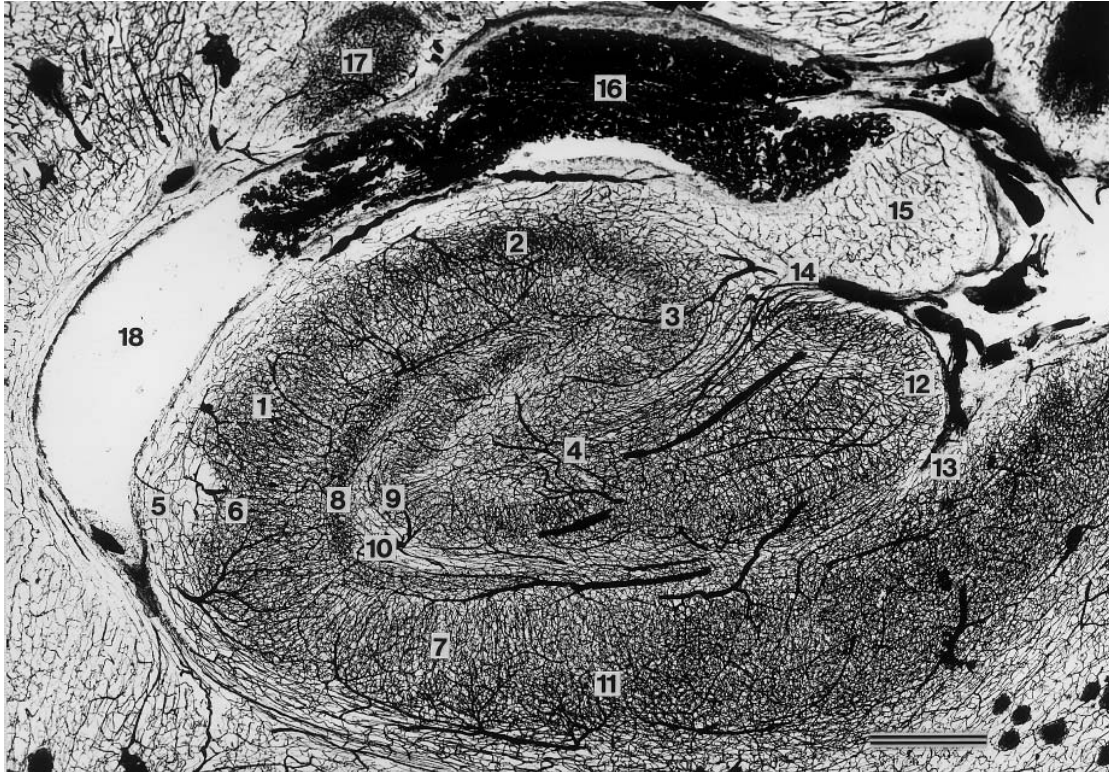


FIGURE 1.4: Coronal section of the hippocampal body after intravascular India ink injection. Bar= 1.5mm. 1–4, CA1–CA4 (fields of the cornu Ammonis). Sublayers of CA1: 5, alveus; 6, stratum pyramidale; 7, strata radiatum and lacunosum; 8, stratum moleculare. Gyrus dentatus: 9, stratum moleculare; 10, vestigial hippocampal sulcus; 11, subiculum; 12, margo denticulatus; 13, superficial hippocampal sulcus; 14, fimbriodentate sulcus; 15, fimbria; 16, choroid plexuses; 17, tail of caudate nucleus; 18, temporal (inferior) horn of the lateral ventricle. Source: Duvernoy (2005).

The polysynaptic (trisynaptic) circuit (Andersen et al., 1971) describes the intrinsic connection of the hippocampal formation. The axons from entorhinal cortex perforates to the molecular layer of the dentate gyrus via the perforant pathway. An alternative alvear pathway reaches CA1 from entorhinal cortex via alveus. The dendrites of the granule cells in the dentate gyrus synapse with the afferent fibers, and their axons (mossy fibers) extend to CA3, where the pyramidal cells emit the Schaffer collaterals projecting to CA1. The circuit completes as the axons from CA1 reaches subiculum, which projects to the entorhinal cortex.

The intrinsic circuitry is involved in the important role of of hippocampus in forming and consolidating long-term memory. The perforant pathway demonstrates the long-term potentiation (LTP), a form of neuroplasticity, which enhances the

synaptic efficacy after rhythmic stimulation and persists after a long period of time. It is now thought to be the mechanism underlying the memory process (Lynch, 2004).

In Alzheimer's disease, hippocampus and entorhinal cortex are affected at an early stage. Amyloid deposit is present in CA1 and subiculum in Braak stage B (Braak and Braak, 1991). Deficits in LTP and memory have been found following injection of A β in region of hippocampus and the aggregation of amyloid (Stéphan et al., 2001; Walsh and Selkoe, 2004) The tau pathology first develops in the transentorhinal region (Braak stage I), and soon spread to hippocampus (Braak stage II). As result of the damage caused by the tangles, the hippocampal formation experiences significant loss of neurons, especially in the CA1 and subiculum, as the severity of disease progresses.

1.1.3 MRI in AD studies

The advancement in modern imaging technologies provides an approach to the internal structures and functioning in the studies of the anatomy, physiology and pathology. A variety of modalities have been developed, and become important tool in clinical diagnosis. The computational and algorithmic development facilitating the signal processing, quantitative analysis, and visualization also prove to be valuable in the biomedical studies.

Various forms of structural and functional imaging modalities have been employed in the AD studies and diagnosis (Villemagne et al., 2005; Ebmeier et al., 2005; Vitali et al., 2008; Tartaglia et al., 2011; Barkhof et al., 2011). Among the structural imaging methods, although CT is widely used in clinical practice, patients are screened by CT mainly to exclude other dementia of treatable causes such as tumor and haematoma. Structural MRI is the more common choice due to its higher resolution and better contrast in soft tissues. The structural MRI based atrophy measures are established as valid marker for AD.

Functional neuroimaging usually adds diagnostic value when structural imaging result is equivocal. MR based measurements such as perfusion imaging, MR spectroscopy, diffusion weighted imaging (DWI), and functional MRI (fMRI), are more sensitive to the functional decline preceding the structural changes, and show potential for markers for early diagnosis. Molecular imaging using emission tomographies such as positron emission tomography (PET) and single-photon emission computed tomography (SPECT) are also used to assess the biology underlying the neurodegeneration process.

In current clinical practices, structural MRI and PET are most commonly deployed. In this thesis, the data dealt with are mainly the structural MR brain images, therefore we will only introduce the brief background of structural MRI and its application in the AD studies.

1.1.3.1 MRI

The physical principle underlying the MRI is nuclear magnetic resonance, which describes the dynamics and manipulates the behavior of nuclear spins or other magnetic systems possessing angular momentum in an external magnetic field (for the physical background of the nuclear resonance, see Slichter, 1990; Levitt, 2008). In MRI, the predominant effect giving rises to the MR signal comes from the proton of hydrogen atom with $\frac{1}{2}$ spin. The spin moments aligned either in parallel or anti-parallel to the external field \mathbf{B}_0 split into two distinct energy levels, conforming to the Boltzmann distribution at thermal equilibrium, with more spinors in the same direction of \mathbf{B}_0 . The net effect of the spin excess is the magnetization that can be detected.

The phenomenon of Larmor precession in classical electromagnetism is retained in quantum mechanics. By applying an additional oscillating radiofrequency (rf) magnetic field tuned to the Larmor frequency of the proton, the magnetization vector can be tipped away from its original longitudinal direction parallel to \mathbf{B}_0 by $\frac{\pi}{2}$, such that the magnetization rotates in the transverse plane perpendicular to

\mathbf{B}_0 . The rotation of the transverse magnetization induces voltage in the receiving coil which turns into electric signal.

Because of the spin-lattice interaction, the rf signal decays as the magnetization tend to re-align to the direction of the static field \mathbf{B}_0 . The decay is characterized by the spin-lattice relaxation time T_1 . The interacting nuclei of different spin state lead to the spin-spin relaxation, in which the individual spins fan out, or dephase, and the net transverse component of magnetization decreases at a rate controlled by the spin-spin relaxation time T_2 . In practice the magnetization undergoes T_2' relaxation due to the inhomogeneities in the external magnetic field. The overall T_2^* decay is combined effect of T_2 and T_2' . The values of T_1 and T_2 depend on the physical property of the material, which varies among the population according to the tissue type and condition.

The suppression caused by field inhomogeneities can be avoided by an additional flip of spins by π using rf pulses, creating an 'echo' of the signal. By tuning the interval T_R over which the recovered longitudinal magnetization is periodically tipped to the transverse plane by the rf pulse, and the echo time T_E when the echo is detected, the result images displays different forms of contrast. A T_1 weighted image acquired with $T_R \leq T_1$, and T_E relatively short to T_2 highlights the differences in T_1 within the sample, while the T_2 weighted image produced by a setting of relatively long T_1 and $T_E \simeq T_2$ enhances the contrasts between materials with different T_2 . With relatively long T_R and short T_E , the spin density or proton density weighted image displays only the density of spin without contrast in T_1 or T_2 .

In imaging experiments, a spatial gradient in the magnetic field is used to encode the spins in the sample with varying frequency and phase at different location. The signal acquired is thus in the k-space of wave vector, which is a Fourier transform of the spatial information. An inverse Fourier transform can be applied to reconstruct the spatial content from the reciprocal domain of k-space, forming the image of the sample. A thorough treatment of the subject from its physical

background to sequence design is found in the classical introduction by Haacke et al. (1999).

1.1.3.2 Structural MR in AD

Clinical and research of structural MRI imaging marker in AD are recently reviewed by Frisoni et al. (2010) and McEvoy and Brewer (2010). The identification of medial temporal lobe atrophy and especially hippocampal atrophy of particular interest in MR studies into AD, which are well established markers of the neurodegeneration process in Alzheimer's disease. Pathologically, the development of hippocampal atrophy is correlated with the deposition of neurofibrillary tangles (Whitwell et al., 2008; Vemuri et al., 2008b, 2009), and neuronal counts (Bobinski et al., 1999; Gosche et al., 2002; Jack et al., 2002). In terms of neuropsychological measurements, the degree of atrophy is also found linked to the memory decline (Thompson et al., 2004; Morra et al., 2009; Kovacevic et al., 2009; Walhovd et al., 2010).

In high resolution MR images, visible changes of atrophies are observed. Visual rating on T_1 -weighted MR image is one way to assess the hippocampal lobe atrophy (Scheltens et al., 1992; Korf et al., 2004; DeCarli et al., 2007; Duara et al., 2008). Quantitative measurements on MR images with manual tracing or automated segmentation show a reduction of hippocampal volume by 15-30% in AD in contrast to 10-15% in MCI (van der Flier et al., 2005; Shi et al., 2009). Longitudinally, the rates of hippocampal atrophy measured in AD are 4.66% (95% confidence interval 3.92, 5.40) and 1.41% (0.52, 2.30) for MCI subjects (Barnes et al., 2009a).

Apart from hippocampus, whole brain atrophy (Fox et al., 1999; Josephs et al., 2008; Schott et al., 2008; Sluimer et al., 2008, 2010) and ventricular enlargement (Jack et al., 2003; Thompson et al., 2004; Jack et al., 2004; Ridha et al., 2008) also indicate the progression of the neurodegeneration. Higher rate of atrophy and faster expansion of ventricle are present in advance of the onset of dementia.

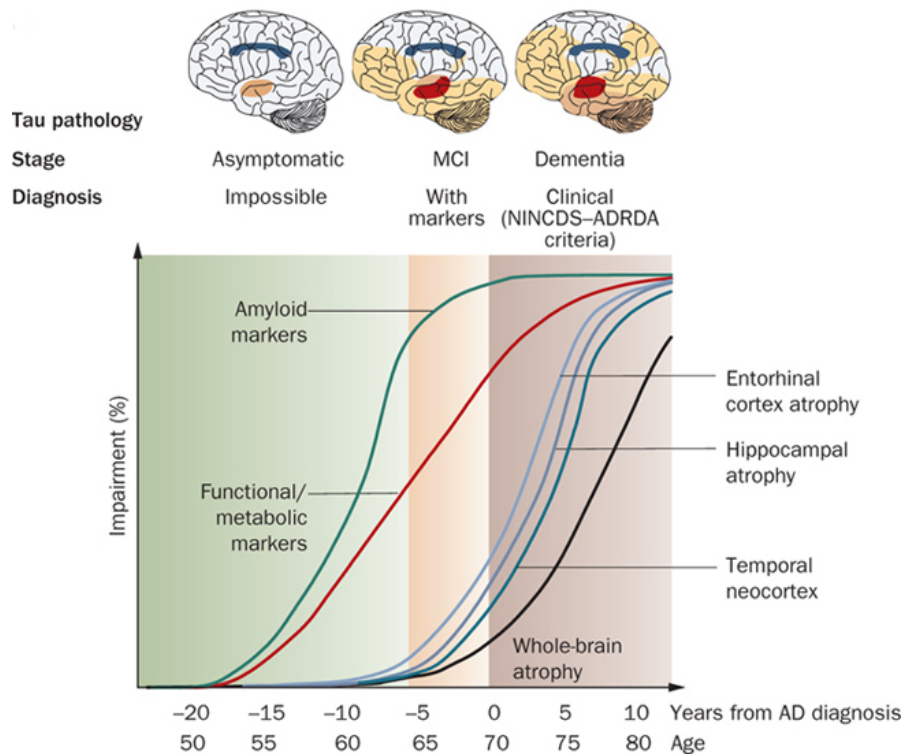


FIGURE 1.5: A theoretical model of natural progression of cognitive and biological markers of Alzheimer disease and the sensitivity of markers to disease state. Amyloid markers (cerebrospinal fluid amyloid- β_{42} and PET amyloid tracer uptake) represent the earliest detectable changes in the Alzheimer disease course but have already plateaued by the MCI stage. Functional and metabolic markers detected by task-dependent activation on functional MRI and ^{18}F -fluorodeoxyglucose PET are abnormal by the MCI stage and continue to change well into the dementia stage. Structural changes come later, following a temporal pattern mirroring tau pathology deposition. Source: Frisoni et al. (2010).

Based on the structural MR imaging markers of medial temporal lobe and hippocampal atrophy, the prediction of MCI patients converting into AD gives on average 81% sensitivity and 73% specificity (see meta-analysis by Yuan et al., 2009). However, it has been pointed out that other markers, such as CSF biomarkers, have to be taken into consideration for the diagnosis due to the lack of specificity in predicting AD at MCI stage solely on the ground of medial temporal lobe atrophy. Hippocampal atrophy, as well as whole brain atrophy and ventricular enlargement, is not specific to AD, and may well occur in the natural process of normal aging. Patterns of atrophy in hippocampal subfields and cortical areas may provide specificity to the disease. Because of the non-linearity in the progress of the atrophy, the rate of atrophy accelerates in the transition stage from MCI to AD, and slows



FIGURE 1.6: Coronal section of Alzheimer's brain with mild ventricular dilatation, and hippocampal atrophy (arrow). Image modified from Barkhof et al. (2011).

down in moderate AD (Frisoni et al., 2009). The structural markers are more sensitive to the change from MCI to dementia in AD.

1.2 Plan of the thesis

In the following chapters, this thesis will discuss the topics on MR image segmentation, shape modeling of biological objects, the shape analysis of hippocampus, and the detection of the hippocampal shape changes in AD.

In Chapter 2, the relevant literature on the segmentation of hippocampus, especially the development of atlas-based methods, the statistical modeling of shapes,

and the statistical analysis of hippocampal volume and shape in AD studies are reviewed.

In Chapter 3, we will introduce the hippocampal segmentation method on MR images using multiple atlases. A supervised method to build a population specific atlas set is developed. The issue of atlas selection in multi-atlas based segmentation is discussed. Two alternative criteria for atlas selection are proposed and evaluated.

In Chapter 4, we detailed the construction of the statistical shape models (SSMs) for hippocampus and the establishment of correspondence by groupwise optimization. We also developed the extrapolation of the SSM to the unseen point set and the shape parameter estimation based on expectation-maximization algorithm.

In Chapter 5, we used the SSMs to perform the shape analysis on the hippocampus and to detect the hippocampal shape changes in AD. We used statistical test to select hippocampal landmarks exhibiting significant difference between the control and the AD groups. We then developed shape analysis method to model the shape variability on the subregions identified by the statistical tests, in order to improve the discrimination ability of the shape analysis using SSM, and correlation of the hippocampal shape description with decline of episodic memory in AD.

The thesis concludes in Chapter 6, which summarizes the work presented in the preparation of this thesis, and outlines the possible future works.

Literature Review

In this chapter, a brief survey of the state-of-the-art in the field of hippocampal segmentation and measurements of hippocampal atrophy in terms of its volume and shape are presented. We first briefly review the methods used in the literature for the segmentation of hippocampus on magnetic resonance (MR) images, with emphasis on the atlas based methods. Then the development of shape analysis and methods in shape modeling are surveyed. Thirdly, the measurement of hippocampal atrophy by volumetry and the application of shape analysis are discussed. Finally, we propose the approach we adopt in this thesis.

2.1 Segmentation of hippocampus in MR images

In medical imaging, the goal of segmentation is to assign meaningful labels to the voxels in the image, such that the regions of different structural or functional units are classified and may provide interpretable results. It is a crucial step in the medical image analysis pipeline. The quality of segmentation directly affects the effect of visualization, the accuracy in the subsequent analysis, and the planning of intervention. Separating white matter, gray matter and CSF, parcellating cortical areas, labeling neuroanatomical nuclei, and detecting boundaries of lesions such as tumours are common examples of segmentation in neuroimaging.

Depending on the application and imaging modalities used in acquisition, a wide range of segmentation methods has been developed in order to deal with images of different parts of body. With respect to the level of human involvement, these methods can be classified into three categories:

- manual segmentation
- semi-automatic segmentation
- automatic segmentation.

Manual segmentation is usually performed by trained experts following certain protocols defining regions of interest (ROIs) on the image. The anatomical knowledge of the expert contributes to the segmentation when the boundaries of the structures are difficult to detect solely based on image features. Although expert-delineated segmentations are regarded as the ground truth or the golden standard, in practice, manual approaches are subjected to both intra- and inter-rater variability induced by the the human factor. Considerable variability may result in low reproducibility of the manual segmentation. In addition, manually tracing the structures of interest by experts is a laborious task, which can be time consuming and expensive. It might take more than one hour per structure for the expert to manually define the boundary of the structure of interest in the volume, which is impractical and inefficient, especially when large data set is involved. Computer softwares are usually used to assist manual tracing and the edition of the boundaries, such as the publicly available MRICron (Rorden and Brett, 2000), imageJ (Abramoff et al., 2004), 3D Slicer (Pieper et al., 2006) and ITK-SNAP (Yushkevich et al., 2006).

Computerized automatic and semi-automatic methods are introduced to reduce the subjectivity in the manual segmentation, and to increase the efficiency and reproducibility. Semi-automatic segmentation still requires manual operations to introduce prior knowledge, provide guidance to the process, or correct the segmentation results. The correction of boundaries sometimes can take as long as manual

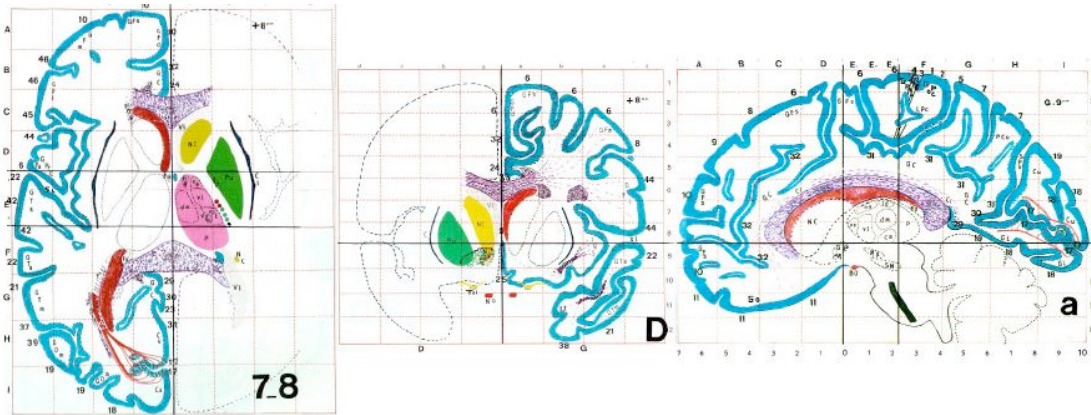


FIGURE 2.1: Samples of labelings from Talairach and Tournoux (1988). From left to right: axial, coronal, sagittal section.

segmentation. In fully automatic methods, the segmentation protocol is translated into the algorithms, and its demand of interaction with the user/operator is minimal. Both semi-automatic and fully automatic segmentations introduce bias arising from the setting of algorithms which tends to segment the image with consistent systematic error. Automatic methods may also be less robust against the presence of unseen pathologies and artefacts, if these influences are not explicitly compensated by the algorithm.

2.1.1 Hippocampal atlases and segmentation protocols

Atlases in medical image analysis are labeled images that are validated to define the boundary or the area of anatomical or functional structures on the image. One atlas defining the brain anatomical regions widely used in neuroimaging studies was published by Talairach and Tournoux (1988), in which a dissected brain was photographed with the labeling of Brodmann's area (see for example Figure 2.1). Later, Montreal Neurological Institute (MNI) defined a new standard brain by averaging series of brain MR scans of normal controls. Based on 305 linearly registered MR scans, the MNI305 brain was created by averaging the intensity of all the images (Evans et al., 1993; Collins, 1994). The ICBM152 template was created by averaging 152 affinely registered brain scans (Mazziotta et al., 2001). Due to the neuroanatomical variability beyond linear transformation, and the

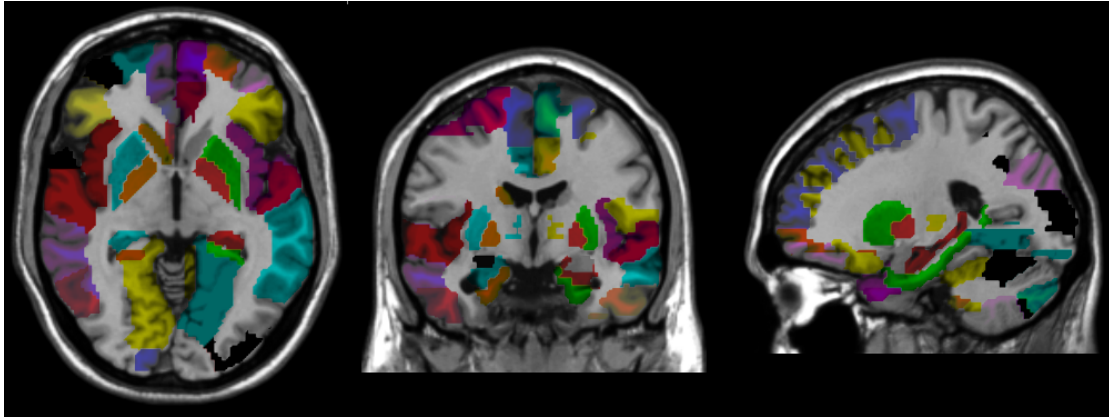


FIGURE 2.2: AAL labeling overlaid on collins27. From left to right: axial, coronal, sagittal section.

effect of averaging, the blurred boundary in these atlases represents the probability of structural labeling at a given coordinate in the normalized space. A single subject template collins27 from MNI with more structural details was created by repeated acquisitions of the same young male subject for 27 times, which were then normalized to the same space of MNI305 to produce an average image. The automated anatomical labeling (AAL, Tzourio-Mazoyer et al., 2002, see Figure 2.2) has been developed on the MNI single subject image, identifying 45 anatomical volumes of interest in each hemisphere. In the definition by AAL, the hippocampal region was defined on the sagittal views as the gray matter under the inferior horn of the lateral ventricle. The dentate gyrus, the uncus, and the hippocampus proper are included. The posterior boundary is limited by the parahippocampal ramus of the collateral fissure.

Besides the standard labelings of AAL, the Internet Brain Segmentation Repository (IBSR)¹ also provides the segmented data of 18 subjects, which are labeled by trained experts into 43 individual regions including subcortical structures such as caudate, hippocampus, pallidum, putamen, thalamus, amygdala, etc. The hippocampal segmentations in IBSR are to be used as atlases in the preparation of this thesis. The segmentations are manually traced using intensity contour line with manual editing (Makris et al., 2004). The hippocampus-amygdala border is traced in the sagittal view by drawing a sulci line in the middle of the inferior ventricle.

¹Available at <http://www.cma.mgh.harvard.edu/ibsr/>.

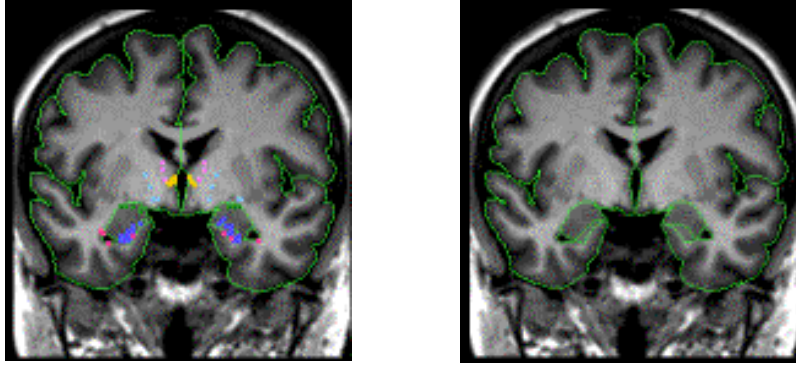


FIGURE 2.3: Delineation of hippocampus in the labelings from the Internet Brain Segmentation Repository (IBSR). Image source: Makris et al. (2004).

The inferior medial border includes the subiculum, most of the presubiculum, and approximately a quarter of the parasubiculum. The fimbria posterior to the commissure is excluded. The lateral ventricle is used as the external landmark where the hippocampal tail terminates.

Other protocols translating the anatomical definition and description into the image domain are developed to make the manual tracing of the hippocampus individual MR images operable. Although hippocampus is a complex structure convoluted inside the medial limbic lobe, its boundary is recognizable under high resolution MR where it borders with adjacent white matter and CSF. While its boundary with amygdala is more difficult to distinguish. The manual delineation of the hippocampi is usually performed on both the left and the right side of the image, while sometimes the image is flipped such that both hippocampi traced on the same side to avoid the laterality bias (Schott et al., 2003; Scahill et al., 2003). Different anatomical guidelines used by various volumetric studies defining the hippocampus on the MR image contributes to the variance among the results reported, which have been reviewed by Geuze et al. (2004). An up-to-date review by Konrad et al. (2009) surveyed 71 published protocols in neuroimaging literature, which identified five main areas where the protocols differ:

- inclusion/exclusion of the white matter such as alveus and fimbria;
- the anterior hippocampus-amygdala border;
- the posterior border to which the hippocampal tail extends;

- the inferior medial border;
- and the use of arbitrary lines.

One of the most widely adopted protocol (15% of the studies reviewed by Geuze et al., 2004) was developed by Watson et al. (1992), with high inter-rater reliability reported (di Sclafani et al., 1998; Du et al., 2001). It defines the hippocampus comprising the hippocampus proper, subicular complex, dentate gyrus, and including the white matter structures of alveus and fimbria. According to this protocol, the hippocampus is traced on the coronal plane. The head of hippocampus is separated from amygdala by the inferior horn of the lateral ventricle (mainly CSF), which extends to the deep part of the uncus forming the uncal recess. If the inferior horn is not visible in the image, the following three alternatives may be used to outline the hippocampus-amygdala boundary: the alveus, an arbitrary line from the inferior horn of lateral ventricle to the sulcus at the inferior margin of the semilunar gyrus, or from straight horizontal line connecting the plane of the inferior horn of the lateral ventricle with the surface of the uncus. The posterior border is defined by the section with the crus of fornix separating the hippocampus from the fimbria. The inferior border is drawn to include the subicular complex and uncal cleft, separating from the parahippocampal gyrus by the angle between the most medial extent of subiculum and parahippocampal gyrus. This protocol is estimated to include 90-95% of the total volume of hippocampal formation.

The protocol set forth by Watson et al. (1992) has been used to validate the automatic segmentations provided by Alzheimer's Disease Neuroimaging Initiative (ADNI)². The automatic segmentation uses the high-dimensional brain mapping tool SNT (Surgical Navigation Technologies), which is commercially available from Medtronic Surgical Navigation Technologies (Louisville, Colorado, USA). The validation was been performed on the normal aging, MCI and AD subjects (Hsu et al., 2002). The hippocampal volumes from ADNI used in the preparation of this thesis are segmented using the SNT tool, with corrections by qualified reviewers. Compared to the manual segmentation protocol, the automated SNT segmentation

²Available at www.loni.ucla.edu/ADNI. For a description of the data provided by ADNI, see §3.4.2.1.

does not include alveus and fimbria, and the volume is 10% less than the volume measured on the manual segmentation.

2.1.2 Survey of segmentation algorithms

Earlier developments in image segmentation are usually solely based on image features, such as thresholding of image intensity, textual analysis, region growing etc. Artificial neural network (ANN) has been used by Pérez de Alejo et al. (2003) for hippocampal segmentation, in which a tissue classification is obtained by an ANN-based vector quantization, and subsequently a supervised multi-layer perceptron on a selected ROI is used to segment the anatomical structure of hippocampus. Methodologies incorporating anatomical templates and atlases modeling the shape and appearance of anatomical structures are later developed to deal with objects such as hippocampus. Apart from the segmentation *per se*, a *meta*-segmentation method using AdaBoost classifiers (Freund and Schapire, 1995) has been developed by (Wang et al., 2011) to detect and correct systematic error in the segmentation based on the spatial, contextual and intensity patterns of the error.

2.1.2.1 Region growing and deformable models

Region growing and deformable model methods usually start from a initial set of seed points, which deforms or grows to match the structure to be segmented. In Ashton et al. (1997), the region starts from a line of seeds along the long axis of the hippocampus, and deforms elastically constrained by the surface tension, deviation from expected surface normal and the force from surrounding tissues. Driven by gray level gradient and internal forces from surface curvature, an initial stack of polygons localizing the hippocampus on parallel slices was used by Ghanei et al. (1998, 2001) and Ghanei and Soltanian-Zadeh (2002). The *Segmentation Automatisée Compétitive de l'Hippocampe et de l'Amygdale* (SACHA) algorithm developed by Chupin et al. (2007, 2009) segments simultaneously hippocampus and

amygdala structures. It is initialized by the manual definition of a bounding box ROI and the seeds placed by the operator in each of the structures. The region growing is guided by the landmark and boundary detection based on extensive use of anatomical priors and image features. The deformation of the region is regularized by Markov random field (MRF), solved using iterative conditional modes algorithm (Besag, 1993). With the automatic definition of the seed point, the fast marching for automated segmentation of the hippocampus (FMASH) by Bishop et al. (2011) propagates the region along the path with smallest resistance defined by a potential function of image intensity using the 3D fast marching method (Sethian, 1996; Deschamps and Cohen, 2000).

2.1.2.2 Shape and appearance based methods

Active shape models (ASM, Cootes et al., 1995) are used in medical image segmentation by fitting a parametric shape model to automatically detected image features or manually defined landmarks (Shen et al., 2002). Using shape information, the elastic deformation of the model to match the intensity profile can be restricted to a prior shape subspace learned from the training set (Kelemen et al., 1999). Knowledge of relative position and distance between anatomical structures, and texture descriptors have also been added to the ASM segmentation of hippocampus (Pitiot et al., 2004). A shape-intensity joint prior model for both hippocampus and amygdala (Yang and Duncan, 2004) has been developed with neighbor constraints and the level set formulation of shape (Yang et al., 2004).

The active appearance model (AAM, Cootes et al., 2001) is a generative model that accounts for the image intensity and texture, i.e. the ‘appearance,’ in addition to the shape structure of the landmarks. Using the image intensity profile along the normal of the structure boundary, the profile appearance model (Babalola et al., 2007, 2008, 2009) produces the segmentation by matching the model to the image minimizing the square of residual differences. A Bayesian approach for AAM method models the conditional distribution of intensity given shape, and the segmentation is obtained by the MAP estimation of the shape given image

intensities (Patenaude et al., 2011; the implementation is available from FMRIB Software Library, Smith et al., 2004; Woolrich et al., 2009)

The state-of-the-art segmentation method publicly available in the FreeSurfer package (Dale et al., 1999; Fischl et al., 1999) labels 37 areas for the whole brain, including 18 subcortical structures. Based on the nonstationary anisotropic MRF modeling of the segmentation, it uses the spatial information from a template in the Talairach space, and a nonlinear transform to account for the inter-subject anatomical variability (Fischl et al., 2002). Forward models of the imaging process are embedded in the segmentation method to achieve the sequence independence (Fischl et al., 2004).

2.1.2.3 Atlas based methods

Atlas based segmentation methods are widely employed in medical image analysis. Using manually delineated atlas as gold standard, this method transform the label map of the atlas to the query image by the registration algorithms from the atlas to the query. Registration methods such as elastic (Miller et al., 1993; Iosifescu et al., 1997; Christensen and Johnson, 2001), fluid (Haller et al., 1996, 1997; Hogan et al., 2000; Crum et al., 2001), and optical flow based registration (Baillard et al., 2001; Dawant et al., 1999; Hartmann et al., 1999) have been involved in matching the image with the atlas. In ANIMAL framework (Collins et al., 1995; Collins and Evans, 1997), the subject image is used as the source, and the atlas as the target in the non-rigid registration, and the mapping of the labels is achieved by the inverse transformation recovered by ANIMAL. Based on an initial FreeSurfer labeling, the method by Khan et al. (2008) uses the Large Deformation Diffeomorphic Metric Mapping (LDDMM, Beg et al., 2005) to search for optimal nonlinear transform between the image and the atlas. Appearance model based methods have been proposed to guide the deformation (Duchesne et al., 2002; Klemencic et al., 2004). Besides the atlas of segmented individual, probabilistic atlases are also used in segmentation, providing the spatial priors such as in the Bayesian

methods (Murgasova et al., 2006, 2007), and FreeSurfer whole brain segmentation (Fischl et al., 2002).

The use of multiple atlases manually traced by experts improves the accuracy of the segmentation based on a single atlas (Rohlfing et al., 2004a,b; Heckemann et al., 2006), by reducing the bias towards each single atlas, and taking the advantage of *a priori* knowledge encoded in the atlas set. Multiple atlases are transformed from the coordinates in the space of atlas to the target image to be segmented by pairwise non-rigid registration (NRR). The labeling of each voxel in the target image is then determined by fusing the warped segmentations of the candidate atlases, usually by a vote rule. The errors made by individual atlas may be corrected by other atlases in the label fusion. It has been shown to be a viable approach to the delineation of subcortical structures in brain MR images (Babalola et al., 2008).

The inter-subject variability may exceed the transformation space searched by the NRR algorithms, such that the error of mismatch between the image and the atlas may be propagated to the segmentation result. Registration failure will lead to the mislabeling. The errors in the result of multi-atlas segmentation thus arise either from the atlases used, or due to the misregistration. In practice, the accuracy of the method depends on the following design choices

- the initial atlas set
- the registration algorithms
- the atlas selection strategy after the registration
- and the label fusion method.

A representative but unbiased set of atlases is usually chosen to target the population of interest. Cohort atlases from the population are found to perform better than using a single standard atlas (Carmichael et al., 2005). Though it is not always readily available, a larger atlas set to cope with the variability in a diverse population (Wolz et al., 2010) or a specific sub-population (Shen et al., 2010). It can be obtained by propagation from a smaller set of manually segmented atlases.

In the registration step, commonly used NRR framework based on maximization of context-free image similarity measure does not ensure correct correspondences between the image-pair (Crum et al., 2003). The mismatch of features is propagated into the result, leading to segmentation errors. In the comparison by Carmichael et al. (2005), NRR methods (Friston et al., 1995; Woods et al., 1998; Chen, 1999) fit better to the complex shape of hippocampus than using only affine transformations (Friston et al., 1995; Woods et al., 1998; Jenkinson et al., 2002). The use of multiple atlases with ANIMAL techniques has been described by Collins and Pruessner (2010). Yassa and Stark (2009) evaluated current registration methods, including Talairach alignment and 3dWarpDrive in AFNI (Cox, 1996), normalization in SPM (Ashburner and Friston, 1999, 2005), LDDMM (Beg et al., 2005; Miller et al., 2005), Diffeomorphic Anatomical Registration Through Exponential Lie Algebra (DARTEL, Ashburner, 2007), and Demons (Thirion, 1998; Vercauteren et al., 2009), in terms of their performance in aligning the structures in the medial temporal lobe. The Demons algorithm was found to perform the best in aligning the hippocampus.

The issue of multi-atlas selection has been discussed by Aljabar et al. (2007, 2009), in which the similarity based atlas selection strategies are classified into three categories, namely segmentation similarity, image similarity, and demographics, with the selection by image similarity ranking being the most popular in applications. The overlap between the segmentation result and the ground truth in multi-atlas segmentation, measured by DSC, reaches its peak when approximately 10 to 20 similarity ranked atlases are selected, and combined by a vote rule (Aljabar et al., 2007), as opposed to the convergence of the DSC, as the number of the atlases randomly selected increases. When less similar atlases are fused to the segmentation result, the information relevant to the segmentation is outweighed by the misalignment propagated to the result.

With regard to the label fusion, the basic method is to combine the transformed label maps by voxel-wise majority voting, and the final labeling of the voxel is

determined by consensus of the voting (Heckemann et al., 2006). A more sophisticated approach is to weight the votes from each atlas based on their performance, such as in simultaneous truth and performance level estimation (STAPLE, Warfield et al., 2004) which estimates the performance level of the atlases using an expectation-maximization (EM) algorithm. In contrast to STAPLE, in which the weights are globally evaluated on the atlas, locally weighted fusion (Commowick et al., 2009; van Rikxoort et al., 2010; Coupé et al., 2010) were developed to reduce the error in the lower ranked atlases by selecting the regions or voxels locally more similar to the target image. Utilizing the intensity information of the target and the atlas images in the fusion step, the local weighted voting (Artaechevarria et al., 2009) method weights each atlas in the voting based on their local similarity to the target. Both global and local weighting are special cases under a generative probabilistic framework developed by Sabuncu et al. (2010). In general, local weighting achieves higher accuracy than global weighting. Applying MRF smoothing to the STAPLE results may improve the performance of the fusion (Leung et al., 2010).

Statistical learning based methods are introduced in the multi-atlas based segmentation to infer the performance of each atlas and to weight the atlases. The segmentation accuracy map (Sdika, 2010) estimates the average accuracy of each voxel in the atlas on the training set, and this estimation is used as the weight in the label fusion. In the fusion by supervised learning and dynamic information (SuperDyn, Khan et al., 2011), the accuracy weights are learned by a linear regression of segmentation accuracy with Tikhonov regularization, which is combined with local estimates of registration accuracy most similar to that of Artaechevarria et al. (2009).

The multi-atlas segmentation has also been developed in combination with approaches. In the work of van der Lijn et al. (2008), the multi-atlas method is used to generate the probability map as the spatial prior, which is then combined with the intensity model and neighborhood model to formulate the energy function. The structures are segmented by minimizing the energy function using a graph cut algorithm (Kolmogorov and Zabini, 2004). The intensity model is refined by

Wolz et al. (2009) and an EM approach is proposed to optimize the energy function (Lötjönen et al., 2010).

2.1.3 Evaluation of segmentation

The segmentation algorithms are usually evaluated in terms of their accuracy, volume,

The accuracy of the segmentation can be measured by the overlap between the segmentation result and the ground truth. The Dice similarity coefficient (DSC, Dice, 1945), also known as the Kappa coefficient in some literature, indicates the percentage of the overlap between two segmentations

$$\text{DSC} = \frac{2|D_S \cap D_R|}{|D_S| + |D_R|}, \quad (2.1)$$

where D_S is the segmented region, and D_R is the reference region (e.g. manually segmented by experts, ground truth). Similar to DSC, the Jaccard index is also a measurement of the overlap, which is defined as

$$\text{JI} = \frac{|D_S \cap D_R|}{|D_S \cup D_R|}. \quad (2.2)$$

If the voxels in the reference D_R are regarded as the actual positives, we can define the sensitivity

$$\text{sensitivity} = \frac{|D_S \cap D_R|}{|D_R|}, \quad (2.3)$$

and the specificity

$$\text{specificity} = \frac{|D_S^C \cap D_R^C|}{|D_R^C|}, \quad (2.4)$$

where D_R^C corresponds to the voxels outside D_R , i.e. the actual negative, and D_S^C corresponds to the voxels not labeled in D_S .

In the applications that are interested in measuring the volume of a given anatomical structure, the normalized volume difference

$$\Delta V = \frac{|D_S| - |D_R|}{|D_R|}, \quad (2.5)$$

is also an important index assessing the accuracy of the segmentation.

Hausdorff distance measures the distance between the boundaries of two regions

$$d_H = \max \left(\sup_{y \in \partial D_S} \inf_{x \in \partial D_R} d(x, y), \sup_{x \in \partial D_R} \inf_{y \in \partial D_S} d(x, y) \right) \quad (2.6)$$

where ∂D_S and ∂D_R are the boundaries of the D_S and D_R respectively, and $d(\cdot, \cdot)$ is the Euclidean distance between the voxels.

2.2 Quantitative analysis of shapes

The quantitative study into the shape of biological objects may date back to the publication of *On Growth and Form* (1917, 1942) by Sir D'Arcy Wentworth Thompson, mathematician, zoologist and classicist, which laid the mathematical ground for zoology and morphology, in a unified account of 'the science of Form and Number.' Subjects such as the magnitude and surface/volume ratio, the forms of cells, tissues and skeletons, shapes of horns and teeth, and their mechanical aspects are investigated. One of the long withstanding contribution of the book is the description of deformation and homologies among species using a Cartesian grid or coordinates in the radial system, as well as the mathematical theory of transformations, which inspired later researchers over the following decades.

Multivariate morphometrics (Reyment et al., 1984) is one traditional way in shape analysis, which performs multivariate analysis on the measurements such as the angles, distances between the landmarks, and the ratio between measurements. The principal component analysis (PCA) is applied to measured covariables, with the first principal component usually the size variation confounded with shape

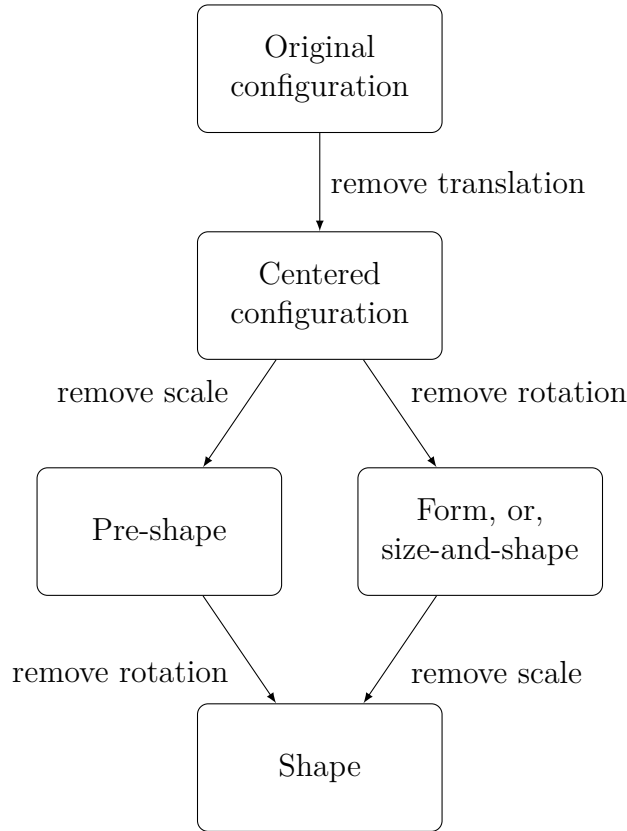


FIGURE 2.4: Hierarchy of shape spaces. Adapted from Dryden and Mardia (1998).

changes (Jolicoeur and Mosimann, 1960). Allometric study (Huxley, 1932; Mosimann, 1970) is another approach to shape analysis that assesses the shape variations associated with the size and growth via the power-law relation.

Recent advancement in mathematical shape theory arises from the seminal work by Kendall (1977) on the Brownian motion in the complex projective spaces, which is later developed in more details (Kendall, 1984, 1989), and the algorithmic development of Thompson's grid method and the statistics of deformation by Bookstein (1978b,a, 1986). Up-to-date introduction on this subject may be found in the monographs by Bookstein (1991), Small (1996), Dryden and Mardia (1998), and Kendall et al. (1999).

We follow the notions and definitions of shape spaces used by Dryden and Mardia (1998) and Kendall et al. (1999) in this thesis. A *configuration* X of k landmarks in the m -dimension Euclidean space can be represented by its $k \times m$ Cartesian coordinates. The *configuration space* comprises of all nondegenerate k -ads, which

is identified with $\mathbb{R}^{k \times m} \setminus \{0\}$. Centering the configuration at its gravity centre filters out the translation, such that the centered landmarks in X_C do not depend on the choice of the origin for the coordinate systems. The centered *pre-shape* Z_C is defined by normalizing X_C of its centroid size $S(X_C)$. The *pre-shape space* S_m^k is equivalent to the unit sphere $S^{(k-1)m-1}$ in the $(k-1)m$ -space. The *size-and-shape* $[X]_S$, also known as the *form*, is the orbit of the centered landmarks under the rotation group $\text{SO}(m)$

$$[X]_S = \{\Gamma(X_C) : \Gamma \in \text{SO}(m)\}, \quad (2.7)$$

with the *size-and-shape space* $S\Sigma_m^k$ defined as the quotient space $\mathbb{R}^{(k-1)m}/\text{SO}(m)$. The *shape* $[X]$ is defined as the remaining geometrical information when both scale $S(X)$ and the rotation are filtered

$$[X] = \{\Gamma(Z_C) : \Gamma \in \text{SO}(m)\}, \quad (2.8)$$

and the *shape space* $\Sigma_m^k \equiv S^{(k-1)m-1}/\text{SO}(m)$ is the orbit of configurations under the action of Euclidean similarity transformations. The hierarchy of different shape spaces are shown in Figure 2.4. Due to the scope of this thesis and the application in biomedical imaging, the dimension m will be limited to 3 here.

2.2.1 Representation of shapes

In biomedical imaging applications, statistical shape analysis is usually carried out on the surface and on landmarks extracted from volume data. Marching cubes algorithm is most commonly used to convert the segmented image volume into surface mesh (Lorenson and Cline, 1987; for a survey of the methods, see Newman and Yi, 2006). For a set X of k landmarks in the 3D Euclidean space, it can be represented by a concatenation of the coordinates of its k landmarks as a $3k$ -vector

$$X = (x^1, y^1, z^1, x^2, y^2, z^2, \dots, x^k, y^k, z^k)^T \in \mathbb{R}^{3k}. \quad (2.9)$$

The triangulation of these landmarks forms a surface mesh of the anatomical object of interest. In general, the shape modeling by SSMs is based on this representation. In the context where the topology of the mesh is less relevant, shape information is adequately described by the landmark representation, giving rise to the name ‘Point Distribution Model’ (PDM, Cootes et al., 1992), which covers the majority of current shape models (for survey, see Heimann and Meinzer, 2009).

Apart from the representation by a set of landmarks, other approaches have been proposed in the literature of image registration, segmentation, and shape analysis. By taking advantage of the fact that most biological objects are homeomorphic to a sphere, one popular method for shape representation is the decomposition of the landmark coordinates into spherical harmonics (SPHARM, Brechbühler et al., 1995; Matheny and Goldgof, 1995), which are the eigen-functions for the angular part of the Laplacian operator. Wavelet technique on contour (Davatzikos et al., 2003) and sphere (Laga et al., 2006; Nain et al., 2007) has also been suggested for shape description. Medial representation (M-rep, Pizer et al., 1999, 2003; Yushkevich et al., 2003b) models geometry of the object by the skeleton of its medial locus with spokes normal to surface representing the boundary. Other representations include spline based methods (Tsagaan et al., 2001, 2002), level set (Tsai et al., 2003; Pohl et al., 2006).

2.2.2 Alignment of point sets

For a given configuration of landmarks, its shape, or the size-and-shape, forms an equivalence class associated with a Euclidean similarity, or rigid transformation group respectively. Without loss of generality, the shape or size-and-shape of the landmarks can be represented by one representative from its respective equivalence class. It may be translated to the origin and aligned to a specified orientation to preserve its size-and-shape, and scaled to a particular size for the analysis of its shape. Procrustes analysis and iterative closest point (ICP) are two major approaches to align the configuration point sets in shape analysis.

Procrustes analysis (for review, see Gower and Dijksterhuis, 2004; Gower, 2010) is used to solve the alignment problem of corresponding points (Goodall, 1991). The ordinary Procrustes analysis refers to the least square estimation of alignment between two configurations. While the translation can be estimated by difference between the two gravity centres, the rotation matrix can be solved by a singular value decomposition (SVD), and the scale can be calculated by the centroid size of two configurations. In the Generalized Procrustes Analysis (GPA, Gower, 1975), a group of configurations are aligned collectively to minimize the sum of squared distances between pairwise configurations. The GPA starts with an arbitrary configuration in the collection as the initial mean, and iteratively aligns all the configurations to the current estimate of the mean, which is updated at each iteration until convergence. The configurations can be aligned via similarity transformations, or rigid transformations depending on the application. Alternative criteria of L_1 - and L_∞ -norms have been proposed for an alignment more resistant to noises (Larsen et al., 2001).

In contrast to Procrustes analysis, the ICP algorithm aligns two point sets without the assumption of given correspondence between them. The basic version of ICP was originally proposed by Chen and Medioni (1992), Besl and McKay (1992), and Zhang (1994), and became widely used and adapted by the imaging and computer vision community due to its simplicity. It establishes the correspondence between two point sets by searching for the closest point of each point from another set, and computes the transformation between the two sets minimizing the distances between the corresponding points. This process is iterative. The search for correspondence and the computation of the transformation are repeated until convergence. The correspondence by closest point may lead to the algorithm in the suboptimal local minimum. Instead of matching the whole point sets, subset matching has been developed by Zhang (1994) in order to make the algorithm more robust against outliers, disappearance, and occlusion. Multitude of variants have been proposed for ICP (Rusinkiewicz and Levoy, 2001), along with improvements in robustness and efficiency (e.g. Simon et al., 1995; Jost and Hugli, 2003; Sharp et al., 2002; Granger and Pennec, 2002; Fitzgibbon, 2003).

2.2.3 Establishment of correspondence

In order to build a shape model for the landmark data, the correspondence across the data set has to be established first. A detailed review of the issue of shape correspondence in building the shape model has been discussed in the review by Heimann and Meinzer (2009), under the categories of mesh-to-mesh registration, mesh-to-volume registration, volume-to-volume registration, parameterization-to-parameterization registration, and population-based optimization. The former three are registration-based methods without explicitly parameterizing the shape data, while the latter two are parameterization-based.

The determination of transformation in registration or alignment, and the correspondence problem are closely interrelated. The reciprocity between them is manifest in the development and the presentation of the ICP algorithm. The search for correspondence is expressed or implied in most registration algorithms. Pairwise point set registration methods, such as ICP-like closest points (Brett and Taylor, 2000; Vos et al., 2004) and non-rigid registration (Subsol et al., 1998; Fleute and Lavallée, 1998; Shelton, 2000; Paulsen and Hilger, 2003) are used to generate the correspondence. The model construction method by Hufnagel et al. (2009) is based on the EM algorithm, which views the probabilistic assignments correspondence as hidden variables. Self-organizing network is used by Ferrarini et al. (2007) to solve the point correspondence problem in the shape modeling and analysis.

The deformation field produced by volumetric registration between images are also used to define the landmark correspondences (Frangi et al., 2001, 2002). The landmarks are defined by an atlas to which the training images are registered, and the landmarks are propagated back to the image via the inverse of the deformation from each image to the atlas, resulting in a set of corresponding landmarks. Instead of defining and propagating the landmarks, the Statistical Deformation Model (SDM, Rueckert et al., 2003) performs the statistical analysis directly on the deformation field from the volumetric registration.

In parameterization based methods, the shape landmarks are mapped to the parameter space bijectively, which establishes a correspondence between each landmark point and a parameter. Depending on the topology of the object, the underlying domain of parameters is usually chosen to be a simpler space homeomorphic to the representation of the shape. The correspondence between different shapes is then defined by associating the landmark points with the same parameter. Most common genus 0 surfaces (i.e. homeomorphic to the sphere S^2) are usually parameterized by spherical coordinates mapping the landmarks to the points on the unit sphere. Commonly used parameterization algorithms are angle-preserving conformal mapping (Haker et al., 2000; Gu and Yau, 2003; Gu et al., 2004), and area-preserving mapping (Brechtbühler et al., 1995). Based on the spherical parameterization, the correspondence can be determined by aligning the first order ellipsoid of the SPHARM shape decomposition (Kelemen et al., 1999). Since the parameterization of each shape is independent, there is no guarantee of ‘optimal’ correspondence between two parameterizations. Reparameterization, i.e. transformation in the parameterization space, is needed to improve the correspondence.

For a shape model with given correspondence, the determinant of the covariance matrix is used by Kotcheff and Taylor (1998) as an objective function for the optimization the model correspondence and compactness. The minimum description length (MDL, Davies et al., 2002) based on information theoretic principles is used as the cost function in search for optimal correspondence, which is to be solved by genetic algorithm (Davies et al., 2002) or Nelder-Mead simplex (Davies et al., 2003). A simplified MDL by Thodberg (2003) gives comparable performance as the original, with analytic form that can be minimized more efficiently using the steepest gradient (Ericsson and Åström, 2003; Hladůvka and Bühler, 2005). To reduce the computational complexity of reparameterization on the sphere, the ‘shape image’ technique is developed by embedding the sphere to a rectangular region, such that the interpolation can be carried out on a 2D grid (Davies et al., 2008b). Full details of the SSM optimization has been published as a monograph (Davies et al., 2008a).

2.2.4 Dimension reduction

In statistical modeling using SSM, PCA is usually used to determine a lower dimensional subspace that accounts for most of the variance observed in a training set (Cootes et al., 1992). High dimensional representation of shape data eq. (2.9) is projected to the subspace, and reconstructed as the approximation of the original shape in the valid space of the shapes of interest. To use PCA for shape analysis requires the corresponding point being aligned to remove the false variation. The principal shape components can be computed by an eigenanalysis on the covariance matrix or an SVD on the data matrix. In practice, the first principal components explaining approximately 90–98% of the total variance span a subspace in which every valid shape can be approximated (Heimann and Meinzer, 2009).

Apart from PCA, independent component analysis (ICA, for review, see Hyvärinen et al., 2001) using joint approximated diagonalization of eigenmatrices (Cardoso, 1999) has been used in shape modeling, which permits more localized variations (Üzümcü et al., 2003; Suinesiaputra et al., 2004). Nonlinear modeling using kernel PCA (Schölkopf et al., 1998) has also been applied in the shape analysis (Twining and Taylor, 2001).

2.3 Measuring the hippocampal atrophy

The MRI studies into AD are interested in the atrophy of hippocampus in particular. Assessment of hippocampal atrophy on the MR images can be carried out at a single time point by comparing the hippocampal volume with the average of the population, or longitudinally tracking the progression of the disease and its effect on the hippocampus. The volume reduction and shape change associated with the atrophy are observable and can be quantified on high-resolution MR images.

2.3.1 Volume measurement

Usual methods to assess hippocampal atrophy are based on the manual or automatic segmentation (e.g. Hsu et al., 2002; Chupin et al., 2009) of the hippocampal volume. The volume of hippocampus can be measured by the count of voxels directly on the segmentation. Due to the difference in the head size which correlates with the hippocampal volume (Free et al., 1995), the hippocampal volumes are often normalized by the total intracranial volume (TIV, e.g. Yavuz et al., 2007) or the intracranial coronal area (ICA, e.g. Järvenpää et al., 2004). Decreased volume in hippocampus and asymmetry in the volume reduction has been reported (for review, see Barnes et al., 2009b; Shi et al., 2009).

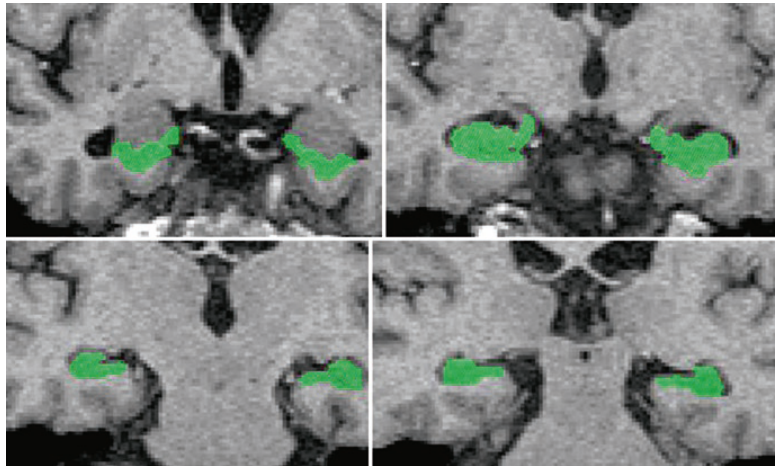


FIGURE 2.5: Tracing hippocampal volume. The region of interest (ROI, green) includes the hippocampal proper, subiculum, dentate gyrus and part of the alveus. Image source: Barkhof et al. (2011).

In longitudinal studies, serial scans are acquired at baseline and follow-up time points. The rate of atrophy indicating the change in volume can be computed if the measurements on the scans over time are available. Since the atrophy rate compares the follow-up measurements with baseline of the same subject, the inter-subject difference in the head size is less important. Images are usually registered to the first scan (e.g. Jack et al., 2004), or a common atlas space (e.g. Barnes et al., 2007). Greater rate of hippocampal atrophy in AD than the control group has consistently been reported in the literature, which have been reviewed in the meta-analysis by Barnes et al. (2009a).

Apart from the direct measurement of volume based on the defined ROI, morphometric methods such as tensor-based morphometry (TBM) and voxel-based morphometry (VBM, Ashburner and Friston, 2000, for review, see Ashburner and Friston, 2003) evaluate the local changes in brain structures without explicitly calculate the absolute volume. While the structural changes are identified in TBM from the Jacobian of the deformation between two images, VBM compares the concentration of gray matter (or white matter) in the local tissues voxel by voxel, which has been used in AD studies to detect the medial temporal lobe atrophy (e.g. Baron et al., 2001; Frisoni et al., 2002), and to measure the hippocampal atrophy (Testa et al., 2004). Findings from morphometric MRI studies in AD and MCI using VBM have been reviewed by Busatto et al. (2008).

Boundary shift integral (BSI, Barnes et al., 2004, 2007) is another method that compares the baseline and the follow-up images and measures the shift in the hippocampal boundary.

2.3.2 Shape analysis

Volume alone provides significant discrimination ability, but is inadequate to fully describe the effect of the disease on the morphology of hippocampus. In addition to volumetry, hippocampal shape analysis also contributed to the understanding of the development of the disease. Regional differences between hippocampal subfields have been found in the neurodegenerative process of AD, with more pronounced neuron loss reported in CA1 and subiculum subfields (West et al., 1994; Bobinski et al., 1998; Rössler et al., 2002; Mueller and Weiner, 2009; for review see Scher et al., 2007). With the development of brain mapping techniques such as radial atrophy mapping (Thompson et al., 2004; Frisoni et al., 2008), and high-dimensional brain mapping (Csernansky et al., 2000; Wang et al., 2003, 2006), findings from neuroimaging studies into AD and MCI have also corroborated the locality of shape changes in CA1 and subiculum subfields along with global tissue reduction (Csernansky et al., 2005; Apostolova et al., 2006; Scher et al., 2007; Chételat et al., 2008; Qiu et al., 2009). Both shape and volume of hippocampus

have been exploited in the detection of AD and to predict the onset of the dementia Csernansky et al. (2005).

Shape surface represented by SPHARM has been employed to model the hippocampus (Gerig et al., 2001) and to detect the shape changes caused by AD (Li et al., 2007; Gutman et al., 2009; Gerardin et al., 2009; Zhou et al., 2009; Cuingnet et al., 2010). SPHARM description of shape boundary has been combined with medial representation (Styner and Gerig, 2001; Bouix et al., 2005) to obtain more localized shape features (Styner et al., 2004). In order to exploit the localized pattern of hippocampal atrophy, feature selection methodology has been employed to select patches on hippocampal surface thus improving the performance of shape features in diagnosing schizophrenia (Yushkevich et al., 2003a) and AD (Zhou et al., 2010). Features characterizing local hippocampal surface deformation with respect to the mean shape have also been used to classify AD (Li et al., 2007).

SSMs have been applied in modeling the variability in the hippocampal shapes among the population Davies (2002); Davies et al. (2003). However, the principal components spanning the subspace for valid shape samples are not necessarily discriminative between the subpopulations of interest. As global shape descriptor, each component models the variation of the whole hippocampal shape which may not be sensitive to local differences. Constraints upon isotropic lesser principal components restricting to the region of interest has been presented to give more meaningful reconstruction (Vermaak and Perez, 2003). In localized components analysis (LoCA, Alcantara et al. (2007)), spatial locality in the shape variation is explicitly optimized, which has been applied to hippocampus shape analysis and shown to produce local shape components strongly correlated with cognitive measurement Xie et al. (2009).

2.4 Approach adopted in this thesis

In this thesis, we will use the multiple atlas-based methods to segment the hippocampal volume, which has been demonstrated to have good performance in this

specific task. We will develop methodologies in various aspects of this approach including the atlas construction and atlas selection. Based on the segmented hippocampal volumes, the groupwise optimization of MDL is used to establish the correspondence across the data set of hippocampal shapes, which is used to build the hippocampal SSMs. We propose an EM-ICP based method to extrapolate the SSM to unseen data and estimate the shape parameters. Then we use the built SSM to analyze hippocampal shape changes in AD. We propose to restrict the shape analysis to the hippocampal subregions where significant difference between the healthy controls and AD patients, which is shown to improve the discrimination ability of the PCA-based hippocampal SSM, and better correlated with the episodic memory decline in AD.

Hippocampal segmentation using multiple atlases

הַפֶּר מִחֻשְׁבוֹת בְּאֵין סוֹד וּבְרַב יוֹעֲצִים תִּקּוּם:

Proverbs, 15:22.

The segmentation of hippocampus poses a challenge to the accurate and precise assessment of hippocampal atrophy in AD. Multi-atlas based segmentation is one successful approach to the automatic segmentation of hippocampus in structural MR images. In this chapter, we first introduce the basic framework of multi-atlas segmentation approach. Then, we develop a supervised method to construct a population specific atlas set for the atlas-based segmentation. The problem of atlas selection problem will also be discussed, to which we proposed two alternative atlas selection strategy in addition to the commonly used selection by image similarity ranking.

The results of population specific atlas construction have been published in “Supervised method to build an atlas database for multi-atlas segmentation-propagation,” in *SPIE Medical Imaging 2010: Computer-Aided Diagnosis*. The results of the alternative atlas selection strategies have been partially published in “Atlas selection strategy in multi-atlas segmentation propagation with locally weighted voting using diversity-based MMR re-ranking,” in *SPIE Medical Imaging 2011: Image*

Processing, and “Atlas selection strategy using least angle regression in multi-atlas segmentation propagation,” in *2011 IEEE International Symposium on Biomedical Imaging*.

3.1 Basic version of multi-atlas based segmentation propagation

In image analysis, the 3D image I acquired by structural MR scans is modeled by a real function defined on a rectangular region $\Omega \subset \mathbb{R}^3$

$$I : \Omega \mapsto \mathbb{R}, \quad (3.1)$$

such that the intensity of each voxel $x \in \Omega$ is given by $I(x)$. The aim of image segmentation is to create a label map

$$L : \Omega \mapsto \mathcal{L}, \quad (3.2)$$

for image I such that each voxel x is identified with a label $L(x)$ in the label set \mathcal{L} .

In multi-atlas based segmentation, we use an atlas set

$$\{(I_k, L_k) : k = 1, 2, \dots, n\} \quad (3.3)$$

in which each atlas image $I_k : \Omega_k \subset \mathbb{R}^3 \mapsto \mathbb{R}$ is labeled with known segmentation $L_k : \Omega_k \mapsto \mathcal{L}$, to segment the query I . Each atlas image is first registered to I , producing the transformation

$$T_k : \Omega \mapsto \Omega_k \quad (3.4)$$

mapping the atlas I_k to the transformed image $I_k \circ T_k : \Omega \mapsto \mathbb{R}$ in the same space of the target I . The same transformation can be applied to L_k such that the transformed label map $L_k \circ T_k$ gives one labeling for the image I . Using multiple

atlases, the result segmentation \hat{L} for the image I can be obtained by combining the transformed label maps

$$\{L_k \circ T_k : k = 1, 2, \dots, n\}. \quad (3.5)$$

The mis-alignment in the transformed atlases due to the registration error is propagated to the segmentation result, which can be reduced by selecting the atlases according to the registration accuracy measured by image similarity. In the similarity based atlas selection, the atlases are ranked by the image similarity between the target image I and the registration result $I_k \circ T_k$. The subset $\mathcal{A} \subset \{1, 2, \dots, n\}$ of total n atlases best registered to the target is selected and combined in the fusion step. Given the selected atlases, the labeling of the query image is determined by the consensus of transformed segmentations. Vote rule is a simple but robust method to produce the consensus segmentation, in which the label for each voxel $\hat{L}(x)$ is estimated as the label that accounts for the majority in $\{L_k(x) : k \in \mathcal{A}\}$. This process of segmentation propagation using multiple atlases is illustrated in Figure 3.1.

3.1.1 Atlas registration

The transformation T between the source I_S and the target I_T are estimated in two steps. Firstly, the transform T is restricted to the space of affine transformations, and the two images are matched by rigid and/or affine registration algorithms. Then, after solving the affine component T^A of the transform T , NRR algorithms are used to register the image $I_S \circ T^A$ to I_T . The final transform T between I_S and I_T is the composition

$$T = T^A \circ T^N, \quad (3.6)$$

in which T^N is the non-rigid deformation found by the NRR algorithm.

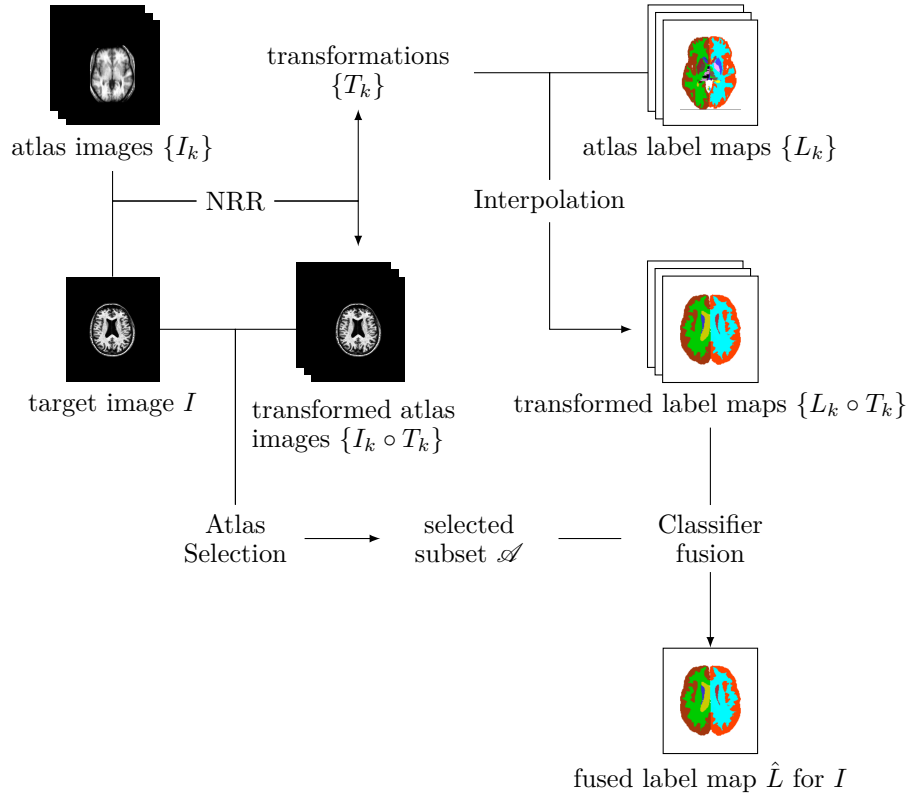


FIGURE 3.1: Diagram demonstrating the process segmentation using multiple atlases.

3.1.1.1 Affine registration

The affine registration is performed using a robust block matching approach (Ourselin et al., 2001). In the block matching step, the image blocks in the source are matched to the target maximizing the image similarity metric. The optimal transformation is then estimated by a least square regression matching the displacement between the blocks in the source and the target. A multi-resolution implementation varying the sampling rate from coarse to fine is used. In practice, the registration is initially performed with a rigid transformation of 6 degrees of freedom ($\text{SO}(3) \times \mathbb{R}^3$): 3D translation and 3D rotation. Based on the rigid initialization, an affine registration is used to estimate the affine transformation T^A of 12 degrees of freedom ($\text{GL}(3, \mathbb{R}) \times \mathbb{R}^3$): 3D translation, 3D rotation, 3D anisotropic scaling, and 3D skew.

3.1.1.2 Non-rigid registration

In the comparison by Yassa and Stark (2009), pairwise cross-participant registrations were performed over 20 MR images of healthy subjects using the state-of-the-art registration algorithms. The manual delineations of subcortical structures including hippocampus, entorhinal cortex, perirhinal cortex, temporopolar cortex and parahippocampal cortex of each subject were warped to the rest 19 images. Methods such as Talairach alignment and 3dWarpDrive in AFNI (Cox, 1996), normalization in SPM (Ashburner and Friston, 1999, 2005), LDDMM (Beg et al., 2005; Miller et al., 2005), DARTEL (Ashburner, 2007), and Demons (Thirion, 1998; Vercauteren et al., 2009) were used for registration, and evaluated by the overlap between the warped and the manual segmentation. The results showed that the Demons algorithm aligns the hippocampus and other subcortical structures with the highest overlap.

The Demons algorithm (Thirion, 1996, 1998) is based on the notion of Maxwell's demons, which are fictitious agents on a semi-permeable membrane directing the diffusion process toward the decrease of the total entropy, thus contradicting the second law of thermodynamics.¹ In Demons algorithm, the transformation between the source and the target images is modeled by diffusion processes with the control of demons driven by the force of optical flow (Horn and Schunck, 1981; Barron et al., 1994). The diffeomorphic Demons is developed by Vercauteren et al. (2007, 2009) in which the unconstrained update of displacement is projected back to the Lie group of diffeomorphisms through the exponential map (Mahony and Manton, 2002; Malis, 2004).

3.1.2 Similarity based atlas selection

In multi-atlas based segmentation, the warped atlases are selected according to their registration accuracy such that the errors in the less well aligned atlases

¹Relevant literature on Maxwell's demons is summarized by Leff and Rex (1990), and more recent review of the paradox and the solutions by Maruyama et al. (2009).

are not propagated to the segmentation result. The atlases to be fused into the segmentation result are selected by their similarity to the query. Three similarity criteria were discussed by Aljabar et al. (2007, 2009), namely

segmentation similarity between the warped label map $L_k \circ T_k$ and the manual segmentation of the query, which is not realistic in the application since it prejudices the outcome of the segmentation, and assumes the availability of the ground truth,

image similarity between the warped atlas $I_k \circ T_k$ and the query image I , which is usually used to evaluate the quality and accuracy of the registration,

demographic information between the atlas subject k and the query subject, which is independent of the image, and registration results.

Among the three similarity criteria, the selection by image similarity is the most popular in applications. The warped atlases $\{I_k \circ T_k\}$ are compared with the target image I , and ranked according to the similarity. The atlases most similar to the target image I are selected. Due to the longer computation time of NRR than the rigid-affine registration, sometimes the atlases are selected based on the rigid-affine results $\{I_k \circ T_k^A\}$, and only selected atlases in \mathcal{A} are registered non-rigidly to I , and combined to produce the segmentation result subsequently. Commonly used image similarity metrics include sum of squared differences (SSD), correlation coefficient, mutual information (Collignon et al., 1995; Viola and Wells, 1995), normalized mutual information (NMI, Studholme et al., 1996), etc. The NMI and correlation coefficient are found to provide better estimates for the accuracy of the warped atlases (Aljabar et al., 2007, 2009).

3.1.2.1 Image mutual information

Image mutual information is a widely used similarity metric in image registration (for review, see Pluim et al., 2003). It is able to measure the alignment between

two images acquired from different modalities, or in MRI, images of different characteristics depending on the acquisition protocols. It is based on the information theoretic definition of the entropy

$$H(I) = - \int_{\mathbb{R}} p_I(s) \log p_I(s) ds \quad (3.7)$$

where $p_I(\cdot)$ is the probability density of the image intensity estimated from the histogram of image I . The joint entropy of two images I and J

$$H(I, J) = - \int_{\mathbb{R}^2} p_{I,J}(s, t) \log p_{I,J}(s, t) ds dt \quad (3.8)$$

is defined by the joint density $p_{I,J}(\cdot, \cdot)$ of the two images. The mutual information is defined as

$$\text{MI}(I, J) = H(I) + H(J) - H(I, J) \quad (3.9)$$

measuring the dependency between two images, and the NMI (Studholme et al., 1996)

$$\text{NMI}(I, J) = 1 + \frac{\text{MI}(I, J)}{H(I, J)} = \frac{H(I) + H(J)}{H(I, J)}. \quad (3.10)$$

When image I and J are independent, the mutual information $\text{MI}(I, J) = 0$ and $\text{NMI}(I, J) = 1$. When the two images are identical, the mutual information is maximized and $\text{NMI}(I, J) = 2$.

3.1.2.2 Correlation coefficient

Correlation coefficient is another image similarity metric, which is defined as

$$C(I, J) = \frac{1}{|\Omega| \cdot \sigma_I \sigma_J} \sum_{x \in \Omega} (I(x) - \bar{I}) (J(x) - \bar{J}), \quad (3.11)$$

where \bar{I} and σ_I , \bar{J} and σ_J are the mean and the standard deviation of the gray level in image I and J respectively.

3.1.3 Label fusion

The most simple method of label fusion in multi-atlas based segmentation is majority vote rule, in which the labeling of each voxel is determined by the consensus

$$\hat{L}(x) = \arg \max_{l \in \mathcal{L}} |\{k \in \mathcal{A} : L_k \circ T_k(x) = l\}|. \quad (3.12)$$

More sophisticated approach is to use weighted votes

$$\hat{L}(x) = \arg \max_{l \in \mathcal{L}} \sum_{k \in \mathcal{A} \text{ and } L_k \circ T_k(x) = l} w_k(x). \quad (3.13)$$

In the local weighted voting (LWV, Artaechevarria et al., 2009), the weights are calculated by a similarity metric on the neighbourhood N_x of the voxel x . Using the mean squared difference (MSD)

$$w_k(x) = \text{MSD}(I_k \circ T_k(N_x), I(N_x))^p \quad (3.14)$$

provides the best performance on the subcortical structures, where p is a negative integer.

The formulation of MSD permits an efficient implementation to calculate the weight $w_k(\cdot)$. We define the MSD $M_{I,J}(\cdot)$ image between image I and J as

$$M_{I,J}(x) \equiv \text{MSD}(I(N_x), J(N_x)) = \frac{1}{|N_x|} \sum_{y \in N_x} (I(y) - J(y))^2, \quad (3.15)$$

which is equivalent of applying a mean filter (over the same neighborhood definition as $N_{(\cdot)}$) to the squared difference image $(I - J)^2$. The algorithm for the computation of the local weight $w_k(\cdot)$ is listed in Algorithm 1.

Algorithm 1 Computation of the weight $w_k(\cdot)$

- 1: Compute the squared difference image $\text{SD}_k \leftarrow (I_k \circ T_k - I)^2$
 - 2: Compute the MSD image $M_k \leftarrow \text{SD}_k \star K_{\text{mean}}$, where K_{mean} is the kernel of mean filter
 - 3: Compute the weight $w_k \leftarrow (M_k)^p$ by applying power function to M_k
-

3.2 Supervised construction of population-specific atlas

To achieve a good performance over a large population with significant inter-subject variability, a large atlas database is required in which the anatomical structures of interest are reliably labeled. For instance, two recent studies (Aljabar et al., 2007, 2009) involved a repository of atlases consisting of more than 270 brain MR images with manual delineation of various structures. Often due to extremely demanding time and cost of expert's labeling, multi-atlas based method, as a successful approach, becomes less practical when the manual segmentation over a dataset of such size is unavailable.

To overcome this limitation, we developed a method of building a set of atlases using the labeled images publicly available from the Internet the Internet Brain Segmentation Repository (IBSR, see §2.1.1). Starting with the 18 atlases available in IBSR, the aim of this method is to construct population specific atlases, for the purpose of multi-atlas based segmentation. Instead of labeling manually defined by experts, the database of atlas can be built up in a supervised manner iteratively. We apply this method to an elderly population of healthy control (NC) and Alzheimer's disease (AD) patients, producing an elderly specific atlas set.

3.2.1 Construction of atlas set

The atlas database is a set of images well segmented, which can be used in multi-atlas based approach to segment unseen query images. Though a large database of manual segmentations may not be readily available, the set of atlases can be constructed by a supervised method. For a MR image dataset from a given population, the process to construct a population specific atlas database is listed below:

The diagram of iterative process is illustrated in Figure 3.2.

The simple majority voting is used to determine the label from the propagated atlas labels. It has been shown Aljabar et al. (2007, 2009) that the Dice similarity

Algorithm 2 Supervised construction of atlas set

- 1: Initialize the atlas database with 18 segmented images in IBSR
 - 2: **while** size of atlas database below a predetermined threshold **do**
 - 3: Using multi-atlas segmentation propagation method, segment the image dataset with the current atlas database
 - 4: Visually inspect the segmentation results
 - 5: Well segmented images with high consistency between the image and labeling over structures of interest are qualified and added to the atlas database
 - 6: **end while**
-

coefficient (DSC) score between the segmentation and the ground truth reaches the highest value when approximately 10 image similarity ranked atlases are fused. Considering the fact that there 8 subjects in the IBSR set are under 18 years old, and to avoid tie votes, 9 atlases were selected in experiment for classifier fusion. The selection was based on image similarity measured by NMI between the unlabeled target image and the registered atlases. The segmentation results were visually inspected, with attention paid especially to the lateral ventricle and deep gray matter structures, such as hippocampus, thalamus, caudate, and putamen. Segmentations qualified in terms of their visual consistency between the image and the corresponding segmentation were added to the atlas database. As the size of atlas database grows, this step can be repeated so that more segmented MR images may be added to the atlas database, enhancing its capability in the multi-atlas based approach.

In this study, the atlas set was initialized with the IBSR data, in which anatomical structures are manually delineated by experts (Makris et al., 2004). The age of subjects in IBSR dataset ranges from juvenile to 71, including 4 juvenile subjects and another 4 under 18 years old. In the age-based atlas selection (Aljabar et al., 2007), selecting atlases of subjects with similar age to the query provides a good estimation. The demographic information of atlases fused is relevant to the performance of multi-atlas based segmentation. Atlases of younger subjects in IBSR are likely to fail when being propagated to the brain images of a subject in elderly population. By adding to the atlas set well segmented brain images of subjects from elderly population, it may improve the performance in segmenting the images of elderly subjects.

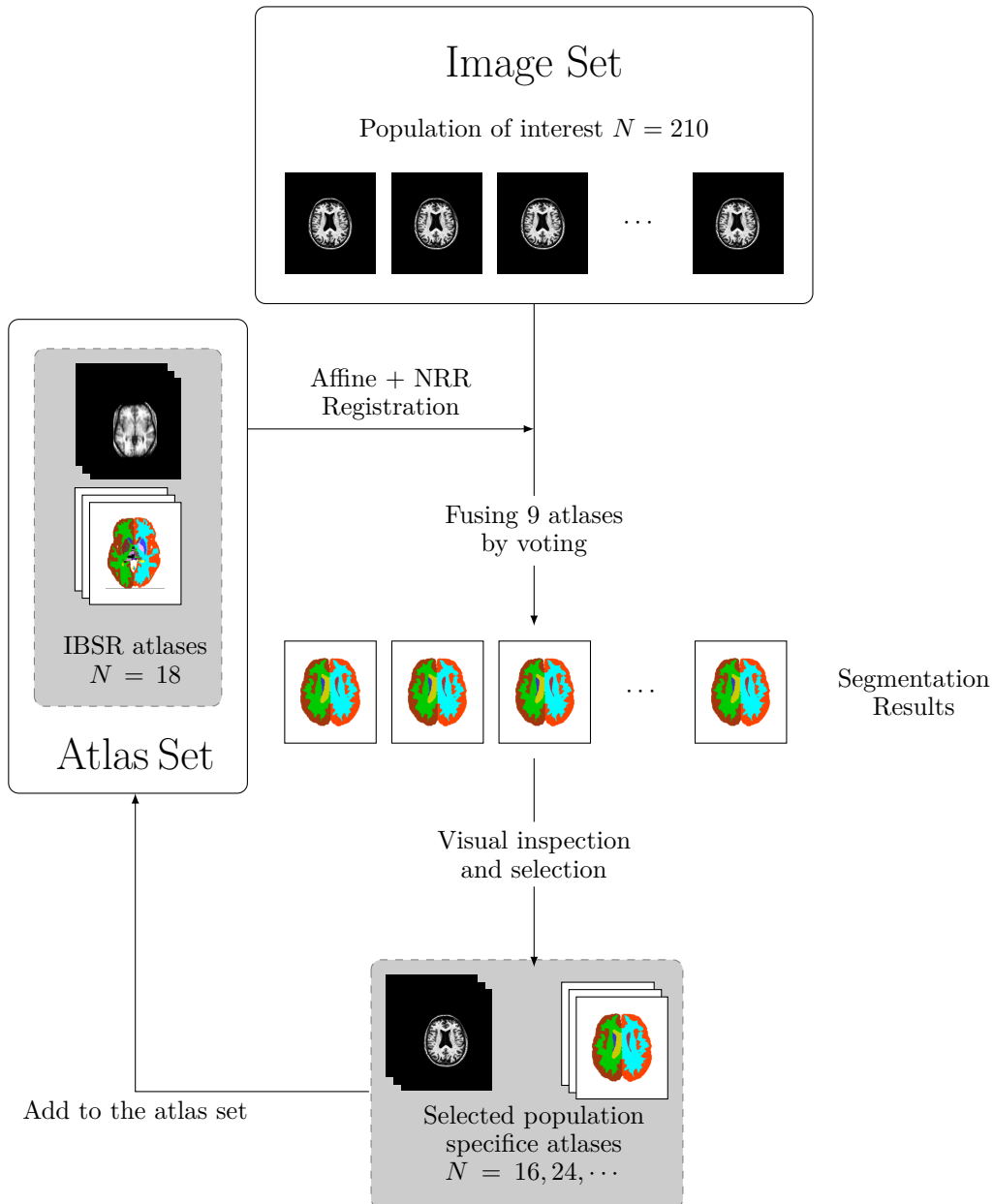


FIGURE 3.2: Diagram demonstrating the process building a set of population specific atlases.

3.2.2 Evaluation of atlas set

In the multi-atlas based segmentation method, the errors in the labeling of atlases may be propagated to the segmentation results. It is therefore necessary to evaluate the quality of atlas produced by the proposed method. Due to the lack of delineation of anatomical structures by experts, it is impossible to assess the accuracy of segmentation of these atlases quantitatively against the manual segmentation as ground truth. Measurements of segmentation's overlap with ground

truth such as DSC score, and the boundary difference such as Hausdorff distance are thus not applicable.

In order to evaluate the atlases produced and selected as described in the previous section, the agreement among their propagated labels is taken into account. The underlying assumption is that the performance of classifier fusion may be affected by the disagreement among propagated segmentations. The agreement among the fused atlases more likely result from the reduction of random error, even though the accuracy of the propagated labels is intrinsically limited by the registration algorithm. It is preferable to deal with individual segmentations agreeing with each other in the fusion of labels. A higher agreement among the atlases means more overlap between the segmentation results, i.e. the consensus region with majority votes, and each individual segmentation propagation. It becomes a measurement of accuracy when the segmentation result is back-propagated to the atlas, and overlap is transformed into the atlas space.

A probability image can be created for each structure when fusing the label maps propagated from n atlases. For a given label $l \in \mathcal{L}$, each pixel in the probability image counts the number of votes it receives, and is normalized by the total number of atlases

$$P_l(x) = \frac{|\{k : L_k \circ T_k(x) = l\}|}{n} \quad (3.16)$$

The entropy of this probability image, and the partial moment of its histogram are used to measure the performance of the atlases.

3.2.2.1 Entropy of probability image

The entropy of image is a statistical measure of its randomness. As far as the probability image is concerned, it can be defined as

$$H_P(P_l) = \sum_{i=1}^n -p_i \log p_i, \quad (3.17)$$

where

$$p_i = \frac{1}{|\Omega|} \left| \left\{ x \in \Omega : P_l(x) = \frac{1}{n} \right\} \right| \quad (3.18)$$

is the probability mass function (pmf) of voxels which have i votes on the given label l . The difference between the definition of H_P and H in (3.7) is that in H_P we only use the positive part of the histogram, thus excluding the background with zero vote ($i = 0$). In the ideal case when all the atlases agree unanimously, the entropy $H_P = 0$.

3.2.2.2 Partial moment of histogram

In addition to the entropy, the second order partial moments of histogram with respect to the reference point 1 is used. It measures the overall deviation of the distribution of the votes from unanimous agreement. It can be defined as follows,

$$\mu_2 = \sum_{i=1}^n p_i \cdot \left(1 - \frac{i}{n} \right)^2. \quad (3.19)$$

In the ideal case of unanimous agreement, $\mu_2 = 0$.

3.3 Atlas selection by re-ranking

When using the locally based methods, the segmentation accuracy on the ranked atlases does not converge as quickly as the simple majority voting on the ranked atlases, and keeps increasing as long as new atlases are added (see, e.g. Sdika, 2010). Since locally based methods requires both the image and the label map of the atlases in the fusion step, it is computationally expensive in terms of both the computation time and the memory footprint, if we increase the number of atlases until the segmentation accuracy converges. In the context of locally based label fusion, we propose the atlas selection strategies other than the similarity ranking. Using the LWV for the label fusion, we re-rank the atlases by maximal marginal relevance (MMR), and use least angle regression (LAR, Efron et al., 2004) to

search for a solution path to an efficient combination of the registration results in addition to the similarity criteria.

3.3.1 MMR re-ranking

MMR criterion was introduced in the field of information retrieval to reduce the redundancy in document summarization by taking diversity into consideration, while still maintaining the relevance to the query (Carbonell and Goldstein, 1998). Since MMR uses only the similarity measurement in re-ranking, it can be easily translated into the context of atlas ranking and selection in multi-atlas based segmentation. In MMR re-ranking, not only the image similarity between the query and the transformed atlas is measured, the similarity between the atlas set is also taken into account. We first define the atlas similarity, which is a symmetric modification of the basic image similarity introduced in 3.1.2, and then describe the MMR algorithm as it is applied to the atlas selection problem.

3.3.1.1 Atlas similarity and image similarity

The similarity between an atlas and the target image can be defined with transformed atlas image after the registration, using NMI (3.10) as the similarity metric

$$\text{Sim}_{\text{NMI}}^A(A_k, I) = \text{NMI}(I_k \circ T_k, I). \quad (3.20)$$

Respectively, when correlation coefficients (3.11) are used as the similarity metric, we can define the measurement as

$$\text{Sim}_C^A(A_k, I) = C(I_k \circ T_k, I). \quad (3.21)$$

This definition of $\text{Sim}_{(\cdot)}^A$ is asymmetric (hence the superscript), since only the atlas image is registered to the target. By performing mutual registration between the atlases in the cross-validation of the atlas set, we obtain the transformation T_{ij} and T_{ji} between every pair of two atlases, A_i and A_j . This enables us to symmetrize

the similarity measurement between two atlases

$$\text{Sim}_{\text{NMI}}(A_i, A_j) = \frac{1}{2} \left(\text{Sim}_{\text{NMI}}^A(A_i, I_j) + \text{Sim}_{\text{NMI}}^A(A_j, I_i) \right) \quad (3.22)$$

$$\text{Sim}_C(A_i, A_j) = \frac{1}{2} \left(\text{Sim}_C^A(A_i, I_j) + \text{Sim}_C^A(A_j, I_i) \right). \quad (3.23)$$

3.3.1.2 Atlas selection by MMR algorithm

We initialize the set of selected atlases \mathcal{A} to be empty and select one atlas each iteration. At each iteration, the atlas \hat{k} is selected according to MMR, such that

$$\hat{k} = \arg \max_{k \notin \mathcal{A}} \left(\lambda \text{Sim}_{(\cdot)}^A(A_k, I) - (1 - \lambda) \max_{j \in \mathcal{A}} \text{Sim}_{(\cdot)}(A_j, A_k) \right), \quad (3.24)$$

until the selected atlas set \mathcal{A} reaches a preset threshold. The similarity $\text{Sim}_{(\cdot)}^A$ and $\text{Sim}_{(\cdot)}$ are to be substituted in practice by the metrics described previously. The parameter $\lambda \in (0, 1]$ controls the similarity measurement $\text{Sim}_{(\cdot)}^A(\cdot, \cdot)$. In addition to similarity, diversity is introduced by penalizing the redundancy

$$\max_{j \in \mathcal{A}} \text{Sim}_{(\cdot)}(A_j, A_k) \quad (3.25)$$

within the selected set \mathcal{A} . When $\lambda = 1$, MMR is equivalent to the similarity ranking using $\text{Sim}_{(\cdot)}^A(\cdot, \cdot)$.

The algorithm of atlas selection using MMR is listed in Algorithm 3. The matrix of atlas similarity $\left(\text{Sim}_{(\cdot)}(A_i, A_j) \right)_{i,j=1,\dots,n}$ can be pre-computed and stored.

Algorithm 3 Atlas re-ranking by MMR

- 1: $\hat{k} \leftarrow \arg \max_k \text{Sim}_{(\cdot)}^A(A_k, I)$
 - 2: $\mathcal{A} \leftarrow \{\hat{k}\}$
 - 3: **while** $|\mathcal{A}| \leq$ the number of atlases to be selected **do**
 - 4: $\hat{k} \leftarrow \arg \max_{k \notin \mathcal{A}} \left(\lambda \text{Sim}_{(\cdot)}^A(A_k, I) - (1 - \lambda) \max_{j \in \mathcal{A}} \text{Sim}_{(\cdot)}(A_j, A_k) \right)$
 - 5: $\mathcal{A} \leftarrow \mathcal{A} \cup \{\hat{k}\}$
 - 6: **end while**
-

3.3.2 Least angle regression

LAR is a variable selection method in regression, which is closely related to other model selection methods such as Lasso (Tibshirani, 1996) and stagewise forward selection. The conceptual connections between them have been exploited, and made it possible to implement all these methods within the same algorithm framework.

We re-formulate the atlas selection in the atlas-based segmentation approach as a variable selection problem in which we estimate the image I from the transformed atlases $\{I_k \circ T_k\}$ as covariates. Assuming the linear independence of the atlas set, for the coefficients $\{\hat{\beta}_k\}$ of each atlas, the estimated image \hat{I} is calculated from the linear model

$$\hat{I} = \hat{I}_b + \sum_{k=1}^n \hat{\beta}_k \cdot I_k \circ T_k, \quad (3.26)$$

where \hat{I}_b is the intercept.

Let $\mathcal{A} \subset \{1, 2, \dots, n\}$ denote the active subset of atlases that is selected by the LAR procedure, and

$$\hat{I}_{\mathcal{A}} = \hat{I}_b + \sum_{k \in \mathcal{A}} \hat{\beta}_k \cdot I_k \circ T_k, \quad (3.27)$$

is the estimate from the current selection \mathcal{A} . We can compute the correlation \hat{c}_k between the current residual $I - \hat{I}_{\mathcal{A}}$ and the transformed atlas $I_k \circ T_k$

$$\hat{c}_k = C(I_k \circ T_k, I - \hat{I}_{\mathcal{A}}) \quad (3.28)$$

and the sign s_k of \hat{c}_k

$$s_k = \begin{cases} 1 & \text{if } \hat{c}_k > 0, \\ 0 & \text{if } \hat{c}_k = 0, \\ -1 & \text{if } \hat{c}_k < 0. \end{cases} \quad (3.29)$$

LAR based atlas selection starts with $\mathcal{A} = \{k_1\}$ such that the atlas $I_{k_1} \circ T_{k_1}$ is most correlated with the image I

$$k_1 = \arg \max_k C(I_k \circ T_k, I) \quad (3.30)$$

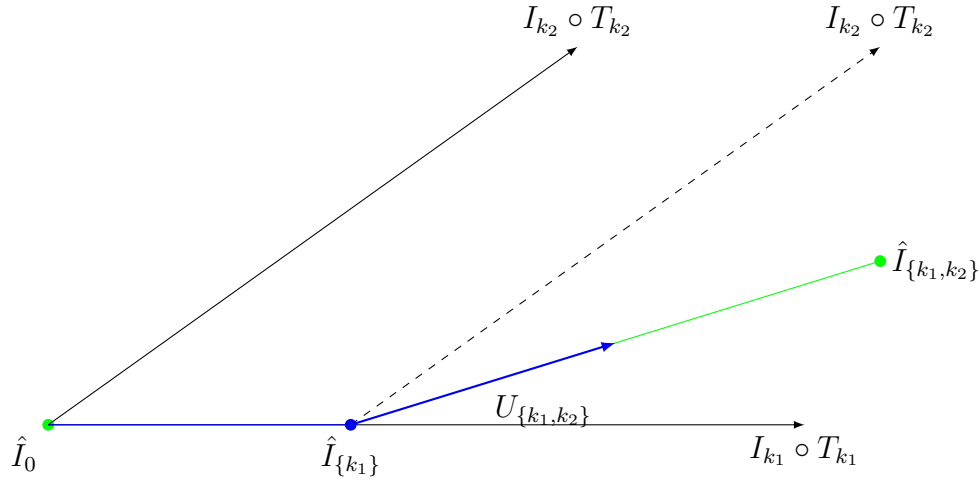


FIGURE 3.3: Least angle regression (LAR) with the first 2 covariates/atlas. $\hat{I}_{\{k_1, k_2\}}$ is the projection of I into $\text{span}(I_{k_1}, I_{k_2})$. The initial residual $\hat{I}_{\{k_1, k_2\}} - \hat{I}_0$ has greater correlation with $I_{k_1} \circ T_{k_1}$ than $I_{k_2} \circ T_{k_2}$; the next LAR estimate is $\hat{I}_{\{k_1\}} = \hat{I}_0 + \hat{\gamma}_1 I_{k_1} \circ T_{k_1}$, where $\hat{\gamma}_1$ is chosen such that $\hat{I}_{\{k_1, k_2\}} - \hat{I}_{\{k_1\}}$ bisects the angle between $I_{k_1} \circ T_{k_1}$ and $I_{k_2} \circ T_{k_2}$. Then $\hat{I}_{\{k_1, k_2\}} = \hat{I}_{\{k_1\}} + \hat{\gamma}_2 U_2$, where U_2 is the unit bisector. Adapted from Efron et al. (2004).

The coefficient $\hat{\beta}_{k_1}$ is increased until a second atlas image I_{k_2} has the same correlation \hat{c}_{k_2} with the current residual as \hat{c}_{k_1} . We use $\hat{\gamma}_1$ to denote the value of coefficient $\hat{\beta}_{k_1}$ at this point. Thus

$$\hat{I}_{\{k_1\}} = I_b + \hat{\gamma}_1 I_{k_1} \circ T_{k_1} \quad (3.31)$$

and k_2 is selected and added to \mathcal{A} . The LAR then proceeds in along the direction U_2 equiangular to both $I_{k_1} \circ T_{k_1}$ and $I_{k_2} \circ T_{k_2}$

$$\hat{I}_{\mathcal{A}} = \hat{I}_{\{k_1\}} + \gamma_2 U_2. \quad (3.32)$$

A third covariate/atlas is added when it has the strongest correlation with the residual equaling the correlation with the two selected variables. The algorithm continues in the direction of the least angle to all the selected variables, and so on.

When more than two atlases are selected, the data matrix of the selected atlases $\mathbf{X}_{\mathcal{A}}$ can be defined as

$$\mathbf{X}_{\mathcal{A}} = (\cdots, s_j \cdot I_j \circ T_j(\Omega), \cdots), \quad j \in \mathcal{A} \quad (3.33)$$

such that each of its column $s_j \cdot I_j \circ T_j(\Omega)$ is a $|\Omega|$ dimensional vector representing the signed atlas image $s_k \cdot I_k \circ T_k$ of $|\Omega|$ voxels. With $|\mathcal{A}| \geq 2$, the LAR algorithm for atlas selection is listed in Algorithm 4.

Algorithm 4 Atlas selection by LAR (Efron et al., 2004)

- 1: **while** $|\mathcal{A}| \leq$ the number of atlases to be selected **do**
 - 2: for all k , update the correlation $\hat{c}_k \leftarrow C(I_k \circ T_k, I - \hat{I}_{\mathcal{A}})$
 - 3: $\hat{C} \leftarrow \max_k \{\hat{c}_k\}$
 - 4: **for all** k **do**
 - 5: $s_k \leftarrow \text{sign}(\hat{c}_k)$
 - 6: **end for**
 - 7: $\mathbf{X}_{\mathcal{A}} \leftarrow (s_k \cdot I_k \circ T_k), k \in \mathcal{A}$
 - 8: $\mathcal{G}_{\mathcal{A}} \leftarrow \mathbf{X}_{\mathcal{A}}^T \mathbf{X}_{\mathcal{A}}$
 - 9: $A_{\mathcal{A}} \leftarrow (\mathbf{1}_{\mathcal{A}}^T \mathcal{G}_{\mathcal{A}}^{-1} \mathbf{1}_{\mathcal{A}})^{-\frac{1}{2}}$, where $\mathbf{1}_{\mathcal{A}}$ is a one-vector of length $|\mathcal{A}|$
 - 10: compute the least-angle image $U_{\mathcal{A}}$ such that $C(I_k \circ T_k, U_{\mathcal{A}}) = C(I_{k'} \circ T_{k'}, U_{\mathcal{A}}), \forall k, k' \in \mathcal{A}$
 - 11: **for all** k **do**
 - 12: $a_k \leftarrow C(I_k \circ T_k, U_{\mathcal{A}})$
 - 13: **end for**
 - 14: $\hat{\gamma} \leftarrow \min_{k \notin \mathcal{A}}^+ \left\{ \frac{\hat{C} - \hat{c}_k}{A_{\mathcal{A}} - a_k}, \frac{\hat{C} + \hat{c}_k}{A_{\mathcal{A}} + a_k} \right\}$, where \min^+ indicates the minimum takes only positive components
 - 15: select the atlas $\hat{k} \leftarrow \arg \min_{k \notin \mathcal{A}}^+ \left\{ \frac{\hat{C} - \hat{c}_k}{A_{\mathcal{A}} - a_k}, \frac{\hat{C} + \hat{c}_k}{A_{\mathcal{A}} + a_k} \right\}$
 - 16: $\mathcal{A} \leftarrow \mathcal{A} \cup \{\hat{k}\}$
 - 17: update $\hat{I}_{\mathcal{A}} \leftarrow \hat{I}_{\mathcal{A}} + \hat{\gamma} U_{\mathcal{A}}$
 - 18: **end while**
-

Analysis of computational complexity shows that LAR is efficient. When $n < |\Omega|$, the computational complexity of entire LAR sequence will be $O(n^3 + |\Omega| \cdot n^2)$ which is linear to the number of voxels $|\Omega|$ (Efron et al., 2004).

3.4 Results and discussion

In the experiments, we constructed an population specific set of atlases from the elderly population enrolled in the Australian Imaging, Biomarker & Lifestyle Flagship Study of Ageing (AIBL) study, using our proposed supervised method, initialized with the generic IBSR atlases. In total 40 atlases of elderly subjects are produced and evaluated in terms of their agreement propagated on the larger elderly population.

For the test of atlas selection strategies, we used a larger atlas set provided by Alzheimer’s Disease Neuroimaging Initiative (ADNI). A leave-one-out cross-validation is performed on two set of atlases. One consists of NC subjects ($n = 138$), and the other consists of AD patients ($n = 99$). The performance of different atlas selection criteria on large atlas sets ($n \sim 100$) is tested.

3.4.1 Supervised atlas construction

3.4.1.1 Materials

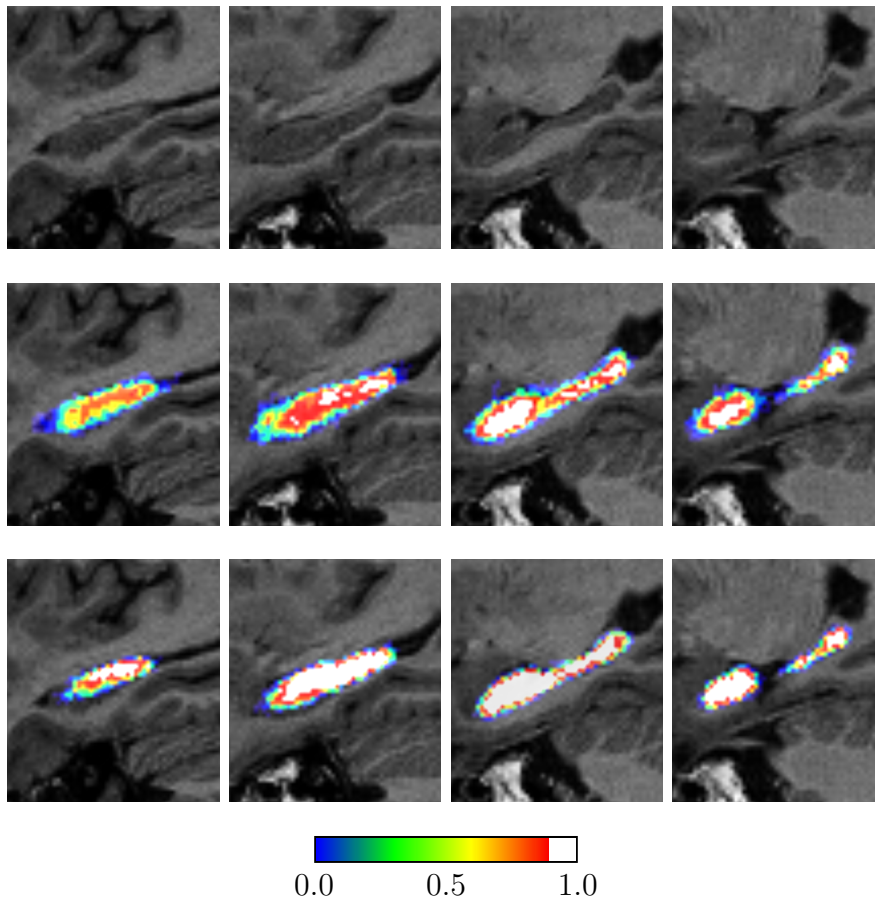


FIGURE 3.4: Probability images P_l of hippocampus of an NC subject in AIBL data, with the white colour indicating unanimous agreement. Top: T1-weighted MR images of hippocampus; middle: the probability images fusing 9 propagated atlases from IBSR, selected according to image similarity; bottom: the probability images fusing 9 atlases propagated from population specific atlases, selected according to image similarity.

The data used in the experiment of supervised atlas construction are from the Australian Imaging, Biomarker & Lifestyle Flagship Study of Ageing (AIBL, Ellis et al., 2010). Launched in November 2006, the AIBL study is a prospective longitudinal study of ageing comprised of patients with AD, MCI and healthy volunteers. The primary goal of AIBL is to develop and confirm a set of diagnostic markers biomarkers and psychometrics that can be used to objectively monitor disease progression and to develop hypotheses about diet and lifestyle factors that might delay the onset of this disease. Successful completion of this work will enable the design and conduct of extensive cohort studies that may lead to clinically proven preventative strategies for AD. Recruitment commenced in 2007 and has been on a volunteer basis. A total of 1112 participants from Western Australia (40%) and Victoria (60%) have been enrolled in the AIBL study. Basic inclusion criteria for the AIBL study required that each participant be aged 60 years of age or older at the time of recruitment, English speaking and, if applicable, have stable medications (e.g. controlled hypertension). Additionally, Alzheimer’s participants were required to have a CDR of 0.5, 1 or 2, to meet the NINDCDS-ADRDA, ICD-10 & DSM-IV criteria for probable or possible AD and to have a reliable informant with contact of at least ten hours per week. About a quarter of the AIBL cohort received imaging using MRI and PiB-PET.

The MR imaging was performed at 2 sites using a Siemens 3T Trio (~60%) and a Siemens 1.5T Magnetom Avanto (~40%). The imaging protocol was defined to follow guideline of Alzheimer’s Disease Neuroimaging Initiative (ADNI), with the exception that a single T1W MPRage was acquired for each subject at each timepoint (compared to 2 T1W MPRage scans in the standard ADNI protocol) and no phantoms were acquired. From the population enrolled in the AIBL study, 210 brain MR images of 170 NC and 40 AD subjects, were segmented using the multi-atlas based segmentation method with the IBSR images used as the initial set of atlases. Among the segmentation results using IBSR atlases, 16 segmentations were qualified and added to the database of atlases after the first iteration. Another 24 were added after the second iteration. Thus an atlas database of 40 segmented

images was built on a population of elderly subjects. The demographics of the selected atlases are shown in Table 3.1, all of which are NC subjects.

TABLE 3.1: Demographics of selected atlases

	IBSR	Iter. 1	Iter. 2
No. of atlases	18	16	24
Male/Female	14/4	6/10	10/14
		mean: 74.54	mean: 75.73
Age	min: Juv.	min: 63.68	min: 62.35
	max: 71	max: 86.10	max: 88.26
MMSE	N/A	27.81	28.88

3.4.1.2 Results

The labels in the 18 IBSR atlases and 40 population specific atlases were propagated to the 210 AIBL images. The atlases were selected based on NMI similarity. For each query, 9 atlases were selected from IBSR atlases and atlases of elderly subjects respectively. The labels from the selected atlases were fused by majority voting. Two examples of probability image of hippocampus produced from IBSR atlases and atlases selected from elderly population are shown in Figure 3.4. The probability images fused by IBSR atlases and atlases of elderly population are evaluated quantitatively in terms of their entropy H_P and the second order partial moment μ_2 of their histograms. For the IBSR and the population specific atlases, the results fusing 9 atlases selected according to image similarity are presented in Tables 3.2 and 3.3.

3.4.1.3 Discussion

The results show that, the agreement among the elderly population specific atlases is in general higher than that from IBSR, when being propagated to query images in the dataset of elderly subjects. For both NC and AD cases, the entropy is higher when probability images are fused with atlases of the IBSR than that of atlases selected from elderly population, indicating a higher randomness in the probability images produced using IBSR atlases. In terms of the second order

TABLE 3.2: Entropy H_P of probability images, the bold indicates the best case in NC and AD respectively, for each structure.

	H_P Entropy of probability image					
	NC			AD		
	IBSR	Iter. 1	Iter. 1+2	IBSR	Iter. 1	+ Iter. 1+2
Hippocampus	3.01	2.82	2.79	3.00	2.82	2.81
Thalamus	2.71	2.61	2.53	2.73	2.56	2.54
Caudate	2.97	2.87	2.89	2.92	2.84	2.89
Putamen	2.99	2.90	2.92	3.02	2.94	2.97
Lateral Ventricle	2.96	2.73	2.55	2.92	2.73	2.49

TABLE 3.3: Partial moment μ_2 of probability image histogram, the bold indicates the best case in NC and AD respectively, for each structure.

	μ_2 Histogram moment of probability image					
	NC			AD		
	IBSR	Iter. 1	Iter. 1+2	IBSR	Iter. 1	+ Iter. 1+2
Hippocampus	0.61	0.60	0.54	0.63	0.61	0.55
Thalamus	0.52	0.56	0.49	0.53	0.61	0.50
Caudate	0.60	0.60	0.56	0.63	0.63	0.58
Putamen	0.55	0.54	0.52	0.57	0.56	0.54
Lateral Ventricle	0.51	0.52	0.54	0.48	0.52	0.43

partial moment of histograms, segmentation propagation with IBSR atlases results in more dissidence than using the atlases selected.

The partial moment μ_2 of the histogram of probability images produced using similarity selected atlases are lower than those randomly selected, indicating more voxels are labeled with fewer votes when fusing a random set of atlases. A similar trend is observed in the results of probability image entropy using population specific atlases. Another observation made on the effect of atlas selection is that this effect is more significant when dealing with AD cases (Table. 3.3).

Considering the size of the population specific atlas set, selecting based on image similarity from a larger pool of atlases produces the label map with a higher degree of agreement. In terms of probability image entropy H_P , the label maps of hippocampus, thalamus and lateral ventricle are produced with less randomness when selecting atlases from 40 atlases, with the exception of caudate and putamen.

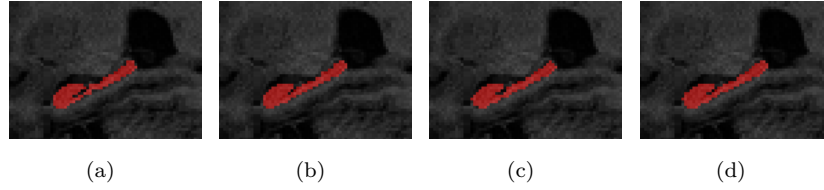


FIGURE 3.5: Comparison of result hippocampal segmentation of one example NC case by fusing 31 atlases selected according to different criteria. (a) SNT segmentation; (b) correlation (DSC=0.861); (c) NMI (DSC=0.865); (d) LAR (DSC=0.871).

While in terms of the partial moment μ_2 , the distributions of the votes using 40 atlases are consistently closer to the unanimous agreement.

All the 40 atlases visually inspected and selected are from NC subjects. Since IBSR atlases are from NC subjects, the well segmented images using IBSR set are more likely to come from NC population. This effect is reflected in the measurement of agreement. The NC atlases are more easily to agree upon NC cases compared to AD ones. The trend is consistently present as measure by the partial moment μ_2 , while it is not very clearly shown in terms of entropy H_P .

3.4.2 Atlas selection strategies

3.4.2.1 Materials

Data used in the experiments were obtained from the Alzheimer’s Disease Neuroimaging Initiative (ADNI) database. The ADNI was launched in 2003 by the National Institute on Aging (NIA), the National Institute of Biomedical Imaging and Bioengineering (NIBIB), the Food and Drug Administration (FDA), private pharmaceutical companies and non-profit organizations, as a \$60 million, 5-year public-private partnership. The primary goal of ADNI has been to test whether serial MRI, positron emission tomography (PET), other biological markers, and clinical and neuropsychological assessment can be combined to measure the progression of MCI and early AD. Determination of sensitive and specific markers of very early AD progression is intended to aid researchers and clinicians to develop new treatments and monitor their effectiveness, as well as lessen the time and cost

of clinical trials. The initial goal of ADNI was to recruit 800 adults, ages 55 to 90, to participate in the research – approximately 200 cognitively normal older individuals to be followed for 3 years, 400 people with MCI to be followed for 3 years, and 200 people with early AD to be followed for 2 years.

In the experiments, two separate atlas sets were used. One consisted of 138 normal control (NC) subjects, and the other with 99 patients diagnosed of Alzheimer’s disease (AD). The hippocampal volumes are semi-automated segmentations provided by ADNI, using high-dimensional brain mapping tool SNT, commercially available from Medtronic Surgical Navigation Technologies (Louisville, CO). SNT hippocampal volumetry has been previously validated on the normal aging, MCI and AD subjects (Hsu et al., 2002). It first uses 22 control points manually placed on the individual brain MRI as local landmarks. Fluid image transformation is then used to match the individual brains to a template brain (Christensen et al., 1997). The segmentations were manually edited by qualified reviewers if the boundaries delineated by SNT were not accurate.

3.4.2.2 Experimental results

We perform a leave-one-out cross-validation on each atlas set. Each NC atlas was registered to all other cases in NC set, and each AD atlas was registered to all the others in the AD set. The registrations were performed by affine transformation using a robust block matching approach (Ourselin et al., 2001) with 12 degrees of freedom, which is followed by non-rigid registration using non-parametric diffeomorphic Demons algorithm (Vercauteren et al., 2007), transforming the atlases by diffeomorphic displacement fields. In total $138 \times 137 + 99 \times 98 = 28\,608$ NRRs were performed, in which 235 failed.

For a given atlas, the labels from other atlases were selected and combined using LWV. NMI and correlation coefficients were used as similarity metrics in the atlas selection. The similarity metrics were evaluated on a region of interest (ROI) containing the hippocampus to be segmented. The ROI is defined by the labeling of the atlas closest to the target with padding of 15-voxel width.

We varied the power p of the MSD in the atlas weight (eq. 3.14) in order to choose the optimal value of p to be used in the LWV. The results of LWV on the NC atlas set with varying values of the power in the atlas weight is plotted in Figure 3.6, which shows that $p = -3$ gave the best performance.

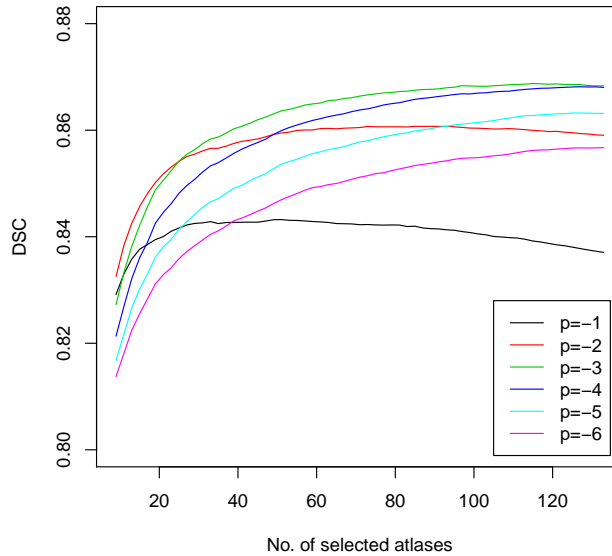


FIGURE 3.6: The average Dice similarity coefficient (DSC) of left and right hippocampi using locally weighted voting (LWV) on the normal control (NC) atlas set with varying power p of the MSD function in the atlas weight. The atlases are selected by normalized mutual information (NMI) ranking.

In the atlas selection by MMR re-ranking, the parameter λ (eq. 3.24) was adjusted. The effects of varying values of λ were plotted in Figure 3.7. The best performance is produced with parameter $\lambda = 0.7$.

The leave-one-out cross validation was performed on the NC atlas set and the AD atlas set. We compared the performance of the image similarity based atlas selection, MMR re-ranking and LAR atlas selection. The results of average DSC of left and right hippocampi with increasing number of atlases selected according to different criteria are shown in Figure 3.8.

3.4.2.3 Discussion

The results show that the MMR re-ranked atlases with $\lambda = 0.7$ outperforms other methods on the NC atlas set. One example of fusing 31 atlases is shown in Figure 3.5. It selects more informative atlases as compared to the same number of

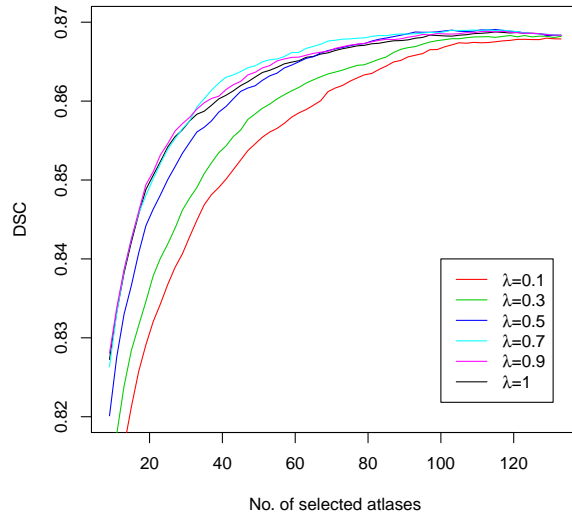
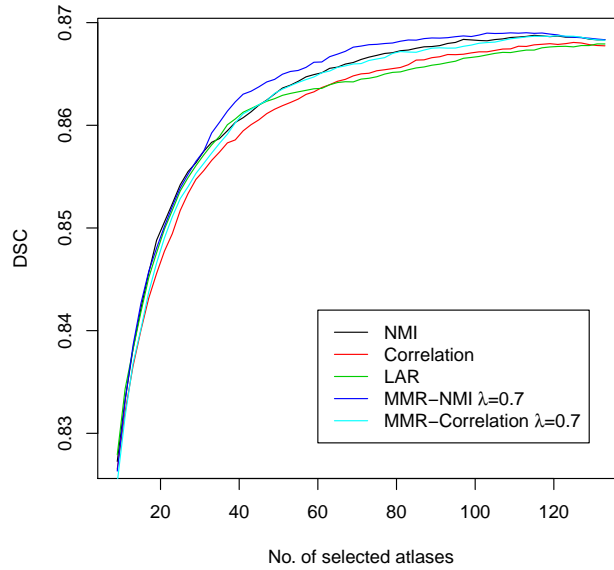


FIGURE 3.7: The average Dice similarity coefficient (DSC) of left and right hippocampi using locally weighted voting (LWV) on the normal control (NC) atlas set. The atlases selected by maximal marginal relevance (MMR) re-ranking. The parameter λ varies from 0.1 to 0.9. The case of $\lambda = 1$ is equivalent to the selection by NMI ranking.

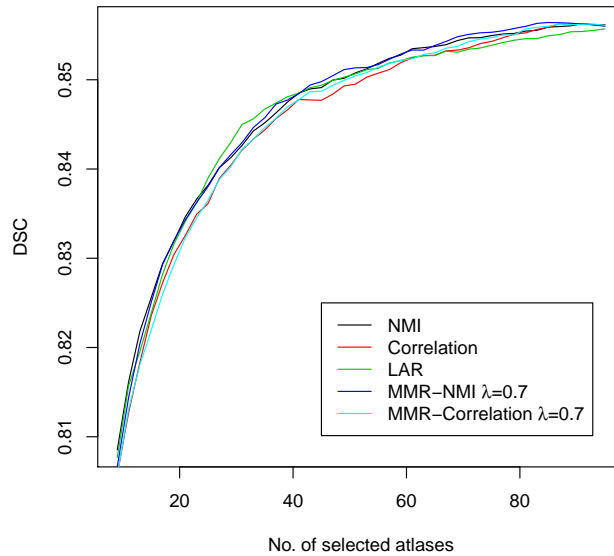
atlases selected according to the image similarity ranking. Combining the atlases selected by MMR reaches accuracy that required more atlases based on similarity selection. MMR is therefore a more efficient strategy when the number of atlases is restricted by the limitations of computation time, memory usage or the availability of atlases.

The effect of using MMR is less significant on the AD atlas set. It may be due to more variability within the AD atlases introducing more noise into the penalty term of MMR. The LAR criterion achieved better performance when there were 20–40 atlases were selected and fused on the AD atlases.

As a parametric method, MMR is dependent upon the parameter weighting the inter-atlas similarity. In terms of computation complexity, the LAR algorithm is more efficient since it does not require the step to pre-compute the inter-atlas similarity matrix as in MMR based method.



(a) Performance of atlas selection strategies on NC atlases.



(b) Performance of atlas selection strategies on AD atlases.

FIGURE 3.8: The average Dice similarity coefficient (DSC) of left and right hippocampi using locally weighted voting (LWV) on the normal control (NC) atlas set. The atlases are selected according to image similarity ranking, maximal marginal relevance (MMR) re-ranking and least angle regression sequence.

3.5 Summary

We used a supervised approach to produce a set of population specific atlases from elderly subjects using multi-atlas based segmentation-propagation. Starting with 18 IBSR atlases, 16 images from elderly population well segmented were added to the atlas set. More images were added in the second iteration. The result

40 population specific atlases were evaluated in terms of their agreement when propagated and fused to target images. Comparing to the 18 images in the IBSR atlases, the population specific atlas set built from the elderly population reaches a higher level of consensus generic IBSR atlases. The result segmentations are produced by a majority vote rule with higher certainty. Although as a supervised approach our method requires visual inspection, it is still less time consuming and costs less than manually segment images.

LWV label fusion gives better accuracy by utilizing the local image similarity information, which makes it possible to improve the segmentation quality by increasing the number of atlases. It is necessary to select the registration results when the number of atlas to be fused is limited. As a combination optimization problem, selection by exhaustive search is not tractable. Conventional heuristics such as similarity ranking selects the atlases most close to the query image while does not consider the inter-atlas redundancy. Selecting atlases re-ranked according to MMR and LAR re-ranking is more efficient compared to image similarity selection when labels are fused by LWV. They provide more accurate results when the same number of atlases are selected and fused. These methods are advantageous when the number the atlases to be fused is limited by the computation time, memory constraint and/or the size of atlas set. In the future work, it will be of interest to search for the selection of atlases based on the combination of current methods in order to optimize the performance of the label fusion over varying sizes of the atlas set.

Statistical shape model of Hippocampus

In nova fert animus mutatas dicere formas corpora

Ovid, *Metamorphoses*, 1.1.

The study of hippocampal shape using statistical shape model (SSM) models the distribution of its shape among the population. It provides not only a characterization of the hippocampal shape variance, which is of interest in the investigations into the morphological changes induced upon the hippocampus by neurodegenerative diseases, but also the prior information which can be used to direct the automatic segmentation of hippocampus in medical images. SSMs are built from corresponding shape surface representations, to model the variability in the distribution of each landmark. Manually locating the anatomical landmarks used in earlier studies (e.g. gorilla skulls by O'Higgins and Dryden, 1993, midsagittal brain MR scans of normal and schizophrenic subjects by Bookstein, 1996) becomes tedious and cumbersome when the shape analysis is carried out on large data set of 3D image volumes, with more densely populated landmarks on the surface of the objects of interest. Automated methods have been developed to reduce spurious correspondences and identify the corresponding landmarks.

In this chapter, the construction of SSMs from hippocampal surfaces by the optimization of minimum description length (MDL) and the evaluation of the constructed SSMs are described. We also presented a symmetric consistent method to extrapolate the SSM to the unseen data and estimate the shape parameters.

The results of the SSM building have been used in “Increasing power to predict mild cognitive impairment conversion to Alzheimer’s disease using hippocampal atrophy rate and statistical shape models,” in *Medical Imaging Computation and Computer-Aided Intervention – MICCAI 2010*, LNCS, vol. 6362. The work of consistent estimation of shape parameters in SSM has been submitted to *SPIE Medical Imaging 2012*.

4.1 Building the shape model

The SSM is built on a training set of hippocampal surfaces $\{X_i : i = 1, \dots, n\}$ in which each surface X_i is represented as a triangulated mesh. The triangulated meshes are usually produced from binary images of segmented label maps by marching cube algorithm (Lorenson and Cline, 1987), and smoothed to remove aliasing and terracing artifacts.

For each surface X_i , the first step is to find a parameterization

$$f_i : U \times V \mapsto X_i \subset \mathbb{R}^3, \quad i = 1, \dots, n \quad (4.1)$$

which gives the position of the point on the 2D surface of the shape given the parameter (u, v) in the parameter space $U \times V$. In order to build the shape model, we expect that the point $f_i(u_0, v_0)$ on the shape surface i , and the point $f_j(u_0, v_0)$ on the shape surface j with the same parameter (u_0, v_0) , would correspond to the same landmark.

For instance, we have two parameterized surfaces of hippocampi f_i and f_j . For a landmark on hippocampus, say the head of hippocampus, $f_i(u_{h_i}, v_{h_i})$ and $f_j(u_{h_j}, v_{h_j})$ their parameters $(u_{h_i}, v_{h_i}) = (u_{h_j}, v_{h_j}) = (u_h, v_h)$ should be the same. This can be

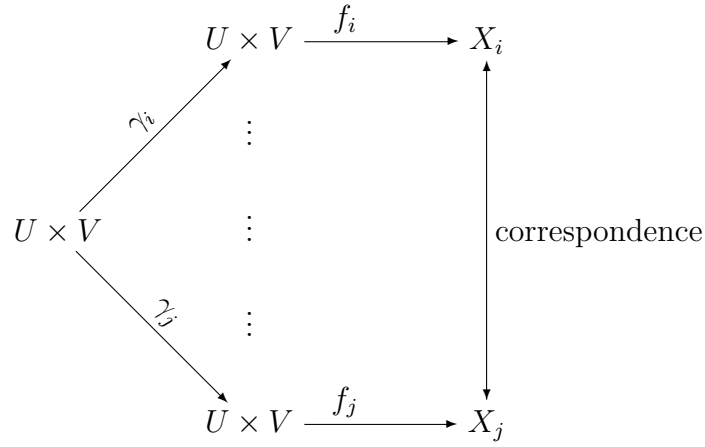


FIGURE 4.1: Parameterizations $\{f_i\}$ and reparameterizations $\{\gamma_i\}$ of the shape surfaces $\{X_i\}$ and correspondences.

achieved by reparameterization of $\{f_i\}$

$$\gamma_i : U \times V \mapsto U \times V, \quad i = 1, \dots, n \quad (4.2)$$

on the parameter space, such that

$$\gamma_i(u_{h_i}, v_{h_i}) = \gamma_j(u_{h_j}, v_{h_j}) = (u_h, v_h), \quad (4.3)$$

and the result collection of parameterizations $\{f_i \circ \gamma_i\}$ establish the correspondence across the training data $\{X_i\}$.

Since the hippocampal segmentation are simply connected regions on MR images, the closed surfaces extracted from the segmentations are homeomorphic to the S^2 sphere. The reparameterizations are thus homeomorphisms on S^2

$$\gamma_i : S^2 \mapsto S^2, \quad i = 1, \dots, n, \quad (4.4)$$

in which a rotation component Γ can be separated

$$\gamma_i = \Gamma_i \circ \tilde{\gamma}_i \quad (4.5)$$

We introduce the calculation of the parameterization f in §4.1.1. To establish

correspondence by reparameterization, we first consider the rotation degree of freedom of the reparameterization (§4.1.2), and then solve the reparameterizations $\{\tilde{\gamma}_i\}$ by an optimization approach minimizing the Minimum Description Length (MDL) of the shape model (§4.1.3).

4.1.1 Parameterization of the shape surfaces

A natural choice of coordinate system on S^2 is to use spherical polar coordinates $(\theta, \phi) \in [0, \pi] \times [-\pi, \pi)$ for the parameterization. A numerical solution to the spherical parameterization of genus 0 surfaces is developed by Brechbühler et al. (1995) which is used to map the hippocampal surfaces to the unit sphere. Since the topology of the surface is used in the parameterization algorithm, the mesh representation of the input surface X is used to preserve both geometrical and topological information. For a given mesh representation for the input X , the parameterization algorithm computes the latitude $\theta(v)$ and the longitude $\phi(v)$ for each vertex v by solving the Laplacian equations

$$\nabla^2 \theta = 0, \quad (4.6)$$

$$\nabla^2 \phi = 0 \quad (4.7)$$

diffusing the coordinates (θ, ϕ) over the mesh X . The diffusion boundary condition is set by initializing a north pole and a south pole on the mesh to be parameterized. The assignment of latitude and longitude is then optimized by minimizing the distortion in the parameterization. Thus the parameterization $f(\theta, \phi)$ of the surface X is defined such that

$$f(\theta(v), \phi(v)) = \mathbf{p}_v \in X \quad (4.8)$$

gives the spatial position \mathbf{p}_v for all the vertex v .

In order to calculate the position $f(\theta, \phi)$ for an arbitrary pair parameters (θ, ϕ) , we first locate the parameters on the unit sphere, where

$$\mathbf{r}(\theta, \phi) = (\sin \theta \cos \phi, \sin \theta \sin \phi, \cos \theta)^T, \quad (4.9)$$

is contained inside the triangle with vertices

$$\begin{aligned} \mathbf{r}_1 &= (\sin \theta(v_{i_1}) \cos \phi(v_{i_1}), \sin \theta(v_{i_1}) \sin \phi(v_{i_1}), \cos \theta(v_{i_1}))^T, \\ \mathbf{r}_2 &= (\sin \theta(v_{i_2}) \cos \phi(v_{i_2}), \sin \theta(v_{i_2}) \sin \phi(v_{i_2}), \cos \theta(v_{i_2}))^T, \\ \mathbf{r}_3 &= (\sin \theta(v_{i_3}) \cos \phi(v_{i_3}), \sin \theta(v_{i_3}) \sin \phi(v_{i_3}), \cos \theta(v_{i_3}))^T. \end{aligned} \quad (4.10)$$

The barycentric coordinate

$$(w_1, w_2, w_3), \quad \forall i = 1, 2, 3 : 0 \leq w_i \leq 1 \quad (4.11)$$

for \mathbf{r} can be calculated, such that

$$w_1 \mathbf{r}_1 + w_2 \mathbf{r}_2 + w_3 \mathbf{r}_3 = \mathbf{r}. \quad (4.12)$$

The corresponding position for (θ, ϕ) can be obtained by a linear interpolation

$$f(\theta, \phi) = w_1 \mathbf{P}_{v_{i_1}} + w_2 \mathbf{P}_{v_{i_2}} + w_3 \mathbf{P}_{v_{i_3}} \quad (4.13)$$

4.1.1.1 Initial parameterization by diffusion

Given the mesh representation for the input X of k vertices, two of the vertices $v_{\text{north}}, v_{\text{south}}$ are selected as the north pole and the south pole

$$\theta(v_{\text{north}}) = 0, \quad (4.14)$$

$$\theta(v_{\text{south}}) = \pi \quad (4.15)$$

which is used as Dirichlet condition of the Lapacian equation $\nabla^2 \theta = 0$. The PDE is approximated on the mesh X by a linear system $\mathbf{A}\boldsymbol{\theta} = \mathbf{b}$, where \mathbf{A} is

the Laplacian matrix for the mesh X , and the vector \mathbf{b} is set by the boundary conditions, and $\boldsymbol{\theta} = (\theta(v_1), \theta(v_2), \dots, \theta(v_k))^T$ is the vector of the values for all the vertex $\theta(v)$. The algorithm setting up the matrix \mathbf{A} , and the vector \mathbf{b} is listed in Algorithm 5.

Algorithm 5 Linear system for the initial diffusion of θ , adapted from Brechbühler et al. (1995)

```

1: {Setting up the matrix  $\mathbf{A}$ }
2: for all vertex  $v_i, i = 1, \dots, k$  do
3:    $A_{ii} \leftarrow$  number of direct neighbors of  $v_i$ 
4:   for all  $v_j$  which is direct neighbor of  $v_i$  do
5:      $A_{ij} \leftarrow -1$ 
6:   end for
7: end for
8: {Setting up the vector  $\mathbf{b}$ }
9: for all  $i = 1, \dots, k$  do
10:   $b_i \leftarrow 0$ 
11:  if  $v_i$  is direct neighbor of  $v_{\text{south}}$  then
12:     $b_i \leftarrow \pi$ 
13:  end if
14: end for

```

To compute the diffusion of the longitude, a date line connecting the north and south pole is chosen as the path with steepest latitude ascent. Analogous to the International Date Line on the globe, there is a 2π -discontinuity in ϕ across the date line, which is used as the boundary condition for ϕ . Since the longitude is undefined for the poles, the neighbors of both poles are disconnected to the pole in the computation of the longitudes. The Laplacian matrix \mathbf{A} for solving the $\boldsymbol{\phi} = (\phi(v_1), \phi(v_2), \dots, \phi(v_k))^T$ is thus modified. The algorithm modifying \mathbf{A} and setting \mathbf{b} is listed in Algorithm 6.

4.1.1.2 Distortion minimization

The initial assignment of parameters $(\theta(v), \phi(v))$ is optimized to reduce the distortion. The optimization is carried out under the constraint of area preserving, i.e. the area of each facet on X must map to a region of proportional area in parameter space S^2 . The optimization process aims to minimize the distortion

Algorithm 6 Linear system for the initial diffusion of ϕ , adapted from Brechbühler et al. (1995)

```

1: {Modification of the matrix  $\mathbf{A}$ }
2: for all direct neighbors  $v_i$  of the north or the south pole do
3:    $A_{ii} \leftarrow A_{ii} - 1$ 
4: end for
5:  $A_{11} \leftarrow A_{11} + 2$  (arbitrary)
6: {Setting up the vector  $\mathbf{b}$ }
7: for all  $i = 1, \dots, k$  do
8:    $b_i \leftarrow 0$ 
9: end for
10: previous  $\leftarrow i_{\text{north}}$ 
11:  $i \leftarrow 1$ 
12: maximum  $\leftarrow 0.0$ 
13: while  $i \neq i_{\text{south}}$  do
14:   for all  $v_j$  which is direct neighbor of  $v_i$  do
15:     if  $\theta(v_j) > \text{maximum}$  then
16:       maximum  $\leftarrow \theta(v_j)$ 
17:       next  $\leftarrow j$ 
18:     end if
19:     if  $j = \text{previous}$  then
20:        $\mathbf{p}_{\text{previous}} \leftarrow \mathbf{p}_{v_j}$ 
21:     end if
22:   end for
23:   for all  $v_j$  which is direct neighbor of  $v_i$ , clockwise between  $\mathbf{p}_{\text{previous}}$  and  $\mathbf{p}_{\text{next}}$  do
24:      $b_j \leftarrow b_j + 2\pi$ 
25:      $b_i \leftarrow b_i - 2\pi$ 
26:   end for
27:   previous  $\leftarrow i$ 
28:    $i \leftarrow \text{next}$ 
29: end while

```

of the mapping. Each square facet on X should map to a spherical quadrilateral close to a spherical square on S^2 , by maximizing the objective function $\sum_{i=1}^4 \cos e_i$, where $e_i, i = 1, 2, 3, 4$ are the 4 arcs of the mapped spherical quadrilateral (see Figure 4.2). The cosine of the arc can be computed as the dot product of two vectors from the centre of the sphere (origin) to the two vertices. The constrained optimization algorithm is solved by a Newton-Lagrange algorithm. An alternative implementation is proposed by Weistrand (2005) which computes the distortion on triangles instead of on quadrilaterals.

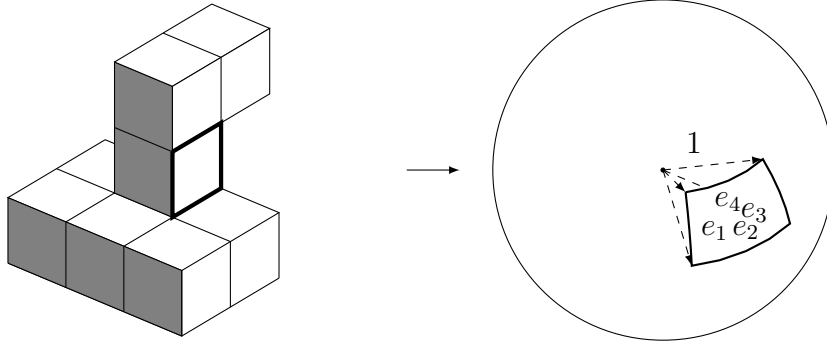


FIGURE 4.2: Parameterization of quadrilateral. The square face (bold) on the physical surface (left) is mapped to the parameter space of unit sphere (right). The length of each edge e_i in the quadrilateral equals to the corresponding center angle. Image adapted from Brechbühler et al. (1995).

4.1.2 Reparameterization by rotation

Since the parameterization is performed on each surface X_i individually, the correspondence across the training set $\{X_i : i = 1, \dots, n\}$ is not guaranteed. In the implementation by Styner et al. (2006), the first degree of SPHARM coefficients for each shape is computed, and the first order ellipsoid is oriented to fit the shape surface. The parameterizations are rotated to coincide both poles of the parameterization to that of the first order ellipsoid. In our implementation, the parameterizations are rotated to minimize the shape difference between surfaces up to similarity transformations based on the parameterization correspondence.

The L_2 distance between parameterizations can be defined based on the standard Lebesgue measure on S^2

$$\|f_i - f_j\|^2 = \int_{S^2} \|f_i(\theta, \phi) - f_j(\theta, \phi)\|^2 d\Omega \quad (4.16)$$

where $d\Omega = \sin\theta d\theta d\phi$ is the surface element on S^2 . The condition of isometry is satisfied for rotation Γ

$$\begin{aligned}
\|f_i \circ \Gamma - f_j \circ \Gamma\|^2 &= \int_{S^2} \|f_i(\Gamma(\theta, \phi)) - f_j(\Gamma(\theta, \phi))\|^2 d\Omega \\
&= \int_{S^2} \|f_i(\Gamma(\theta, \phi)) - f_j(\Gamma(\theta, \phi))\|^2 J^{-1}(\Gamma(\theta, \phi)) d\Omega(\Gamma(\theta, \phi)) \\
&= \int_{S^2} \|f_i(\Gamma(\theta, \phi)) - f_j(\Gamma(\theta, \phi))\|^2 d\Omega(\Gamma(\theta, \phi)) \\
&= \|f_i - f_j\|^2
\end{aligned} \tag{4.17}$$

since the Jacobian J for rotation is 1 on S^2 . Assuming the shape surfaces $\{X_i\}$ are aligned (e.g. by ICP algorithm) via similarity transforms to a common template, the rotation Γ_i can be found by minimizing the pairwise distance

$$\Gamma_i = \arg \min_{\Gamma \in \text{SO}(3)} \|f_i \circ \Gamma - f_1\|^2, \tag{4.18}$$

where f_1 is an arbitrarily selected parameterization as the template. Multiple runs with different choices of template may be performed in order to avoid bias towards the choice of template.

In implementation, the L_2 distance may be evaluated by sampling on S^2

$$\|f_i - f_j\|^2 \simeq \frac{4\pi}{k} \sum_{s=1}^k \|f_i(\theta_s, \phi_s) - f_j(\theta_s, \phi_s)\|^2, \tag{4.19}$$

where (θ_s, ϕ_s) , $s = 1, \dots, k$ are uniformly sampled on S^2 by Platonic solids such as octahedron, dodecahedron or icosahedron. By parameterizing the rotation Γ using Rodrigues parameters or quaternions, the optimization problem in (4.18) thus becomes a least-square problem with closed form solution, which can be solved by Nelder-Mead simplex or other standard optimizers.

A multi-resolution scheme can be easily implemented by subdividing the initial sampling (Figure 4.3). The multi-resolution algorithm for rotational reparameterization is listed in Algorithm 7.

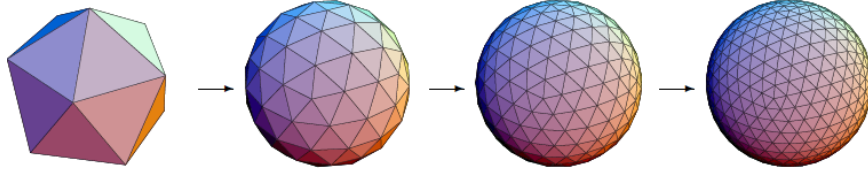


FIGURE 4.3: Multi-resolution subsampling by icosahedron subdivision. Left to right: icosahedron, subdivisions by factor 2, 4 and 6. Image credit: Styner et al. (2006).

Algorithm 7 Multi-resolution reparameterization by rotation.

```

1: for  $i = 1, \dots, n$  do
2:    $\Gamma_i \leftarrow \text{Id}$ 
3: end for
4: for each trial do
5:   select an arbitrary parameterization  $f_j$  as the template
6:    $\{(\theta_s, \phi_s)\} \leftarrow$  coordinates of icosahedron vertices
7:   for each level of resolution do
8:     for all  $f_i \neq f_j$  do
9:       initialize the optimizer with current  $\Gamma_i$ 
10:      update  $\Gamma_i \leftarrow \arg \min_{\Gamma \in \text{SO}(3)} \sum_{s=1}^k \|f_i(\Gamma(\theta_s, \phi_s)) - f_j(\Gamma_j(\theta_s, \phi_s))\|^2$ 
11:     end for
12:   end for
13: end for

```

4.1.3 Groupwise optimization on shape images

Given the rotationally reparameterized surfaces $\{f_i \circ \Gamma_i, i = 1, \dots, n\}$, the remaining component of the homeomorphisms $\{\tilde{\gamma}_i\}$ are to be computed by the optimization of the MDL of the collection $\{f_i \circ \Gamma_i \circ \tilde{\gamma}_i, i = 1, \dots, n\}$. Instead of reparameterizing on S^2 , which involves intersection and interpolation on the sphere, Davies et al. (2008b) re-map the parameterization to an image in \mathbb{R}^2 to facilitate the manipulation of the shape representation. The reparameterization on the image representation of shapes is turned to a problem similar to the non-rigid registration. Groupwise optimization is used to reparameterize each individual shape, and fluid regularization is applied.

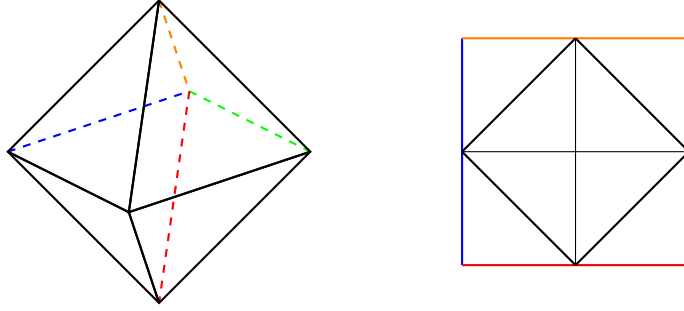


FIGURE 4.4: Cutting the octahedron and unfold to a plane. The edges cut are color coded. Left: octahedron, right: unfolded octahedron. Adapted from Praun and Hoppe (2003).

4.1.3.1 Image representation and manipulation of shapes

In previous steps, the shape surfaces are parameterized by spherical coordinates on S^2 . By sampling on S^2 by a subdivided octahedron, shape surface X_i is sampled as

$$f_i \circ \Gamma_i(\theta_s, \phi_s), \quad s = 1, \dots, k \quad (4.20)$$

where $(\theta_s, \phi_s), s = 1, \dots, k$ are sampled parameters on S^2 by the octahedron. The octahedron can be mapped to a 2D grid bijectively by cutting the edges of the octahedron, and unfolding it to the plane (see Figure 4.4, Praun and Hoppe, 2003). Due to cutting of the surface, some nodes in the octahedron are duplicated when unfolded on the plane. Subdivided octahedron of $k = 4N^2 + 2$ nodes is unfolded to a $(2N + 1) \times (2N + 1)$ grid. Each node $(i, j) \in \mathbb{N}^2$ on the grid is associated with a node $s(i, j)$ on the subdivided octahedron. The mapping

$$g : D = [0, 1] \times [0, 1] \subset \mathbb{R}^2 \mapsto S^2 \quad (4.21)$$

from a image domain D to the parameter space S^2 , which can be interpolated from the values of the grid nodes

$$g(\mathbf{x}_{i,j}) = (\theta_{s(i,j)}, \phi_{s(i,j)}) \quad (4.22)$$

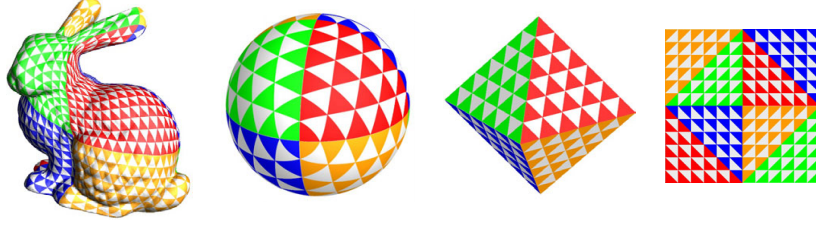


FIGURE 4.5: The construction of a shape image, from shape to sphere to embedded octahedron to final shape image. The colour code denotes corresponding regions. From left to right: physical surface (bunny), spherical parameterization, octahedron embedding, shape image. Image credit: Praun and Hoppe (2003); see also Davies et al. (2008b).

where each node (i, j) is identified with a pixel $\mathbf{x}_{i,j} \in [0, 1] \times [0, 1]$. A vector image S can be defined on D

$$S = f \circ \Gamma \circ g : D \mapsto \mathbb{R}^3 \quad (4.23)$$

such that the homeomorphic reparameterization $\tilde{\gamma}$ on S^2 is equivalent to a deformation ψ of the image domain

$$S \circ \psi = f \circ \Gamma \circ \tilde{\gamma} \circ g \quad (4.24)$$

where

$$\psi = g^{-1} \circ \tilde{\gamma} \circ g : D \mapsto D \quad (4.25)$$

is a 2D deformation field.

In the discussions of kinetics of continuous media and the modeling of deformation in image registration, physical quantities such as the displacement and the velocity field are more efficiently studied under Eulerian reference frame, in which the frame of reference is fixed with respect to the laboratory system, in contrast to the Lagrangian frame which follows the motion of the particles. Under Eulerian reference frame, the deformation ψ is described by the displacement $\mathbf{u}(\mathbf{x}, t)$ of the particles passing through \mathbf{x} at time t , originated from $\mathbf{x} - \mathbf{u}(\mathbf{x}, t)$ at $t = 0$. Given the displacement field \mathbf{u} , the shape image can be reparameterized

$$S'(\mathbf{x}) = S(\mathbf{x} - \mathbf{u}(x)) \quad (4.26)$$

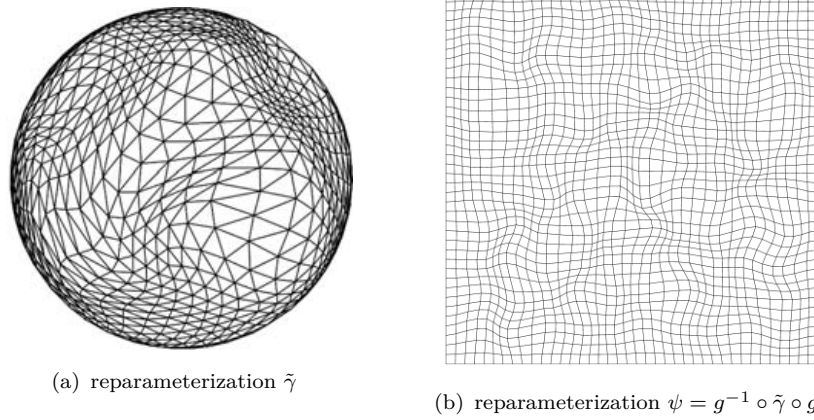


FIGURE 4.6: Reparameterization on the spherical parameterization and on the shape image. Left: the reparameterization $\tilde{\gamma}$ on the sphere; right: the reparameterization $\psi = g^{-1} \circ \tilde{\gamma} \circ g$ on the shape image, which is equivalent to a deformation on a 2D image. Image credit: Davies et al. (2008a).

with the deformation

$$\psi(\mathbf{x}) = \mathbf{x} - \mathbf{u}(\mathbf{x}). \quad (4.27)$$

4.1.3.2 MDL cost function and its gradient

The original MDL cost function for optimizing correspondences was proposed by Davies et al. (2002, 2003), which was simplified by Thodberg (2003). With each shape surface in the collection $\{X_i, i = 1, \dots, n\}$ sampled by octahedron and mapped to 2D images, the mean \bar{S} and the covariance matrix Σ for the shape sample can be computed

$$\bar{S}(\mathbf{x}) = \frac{1}{n} \sum_{i=1}^n S_i(\mathbf{x}), \quad (4.28)$$

$$\Sigma_{ij} = \frac{1}{(2N+1)^2} \sum_{i=1}^{2N+1} \sum_{j=1}^{2N+1} (S_i(\mathbf{x}_{i,j}) - \bar{S}(\mathbf{x}_{i,j})) \cdot (S_j(\mathbf{x}_{i,j}) - \bar{S}(\mathbf{x}_{i,j})). \quad (4.29)$$

The MDL cost function is defined as

$$\mathcal{L}_{\text{MDL}} = \sum_{\lambda_m \geq \lambda_c} \left(1 + \log \frac{\lambda_m}{\lambda_c} \right) + \sum_{\lambda_m < \lambda_c} \frac{\lambda_m}{\lambda_c}, \quad (4.30)$$

where λ_m are the eigenvalues of the covariance matrix Σ , and λ_c is the cut-off value. The variation of the MDL cost function \mathcal{L}_{MDL} with respect to the the

position in the landmark $S_i(\mathbf{x})$ has been derived by Ericsson and Åström (2003) based on the SVD decomposition of the data matrix, and by Hladůvka and Bühler (2005) on the eigen-decomposition of the covariance matrix Σ .

The variation based on eigen-decomposition is used in the implementation. The variation of the cost function with respect to the displacement \mathbf{u}_i at pixel (i, j) in i -th shape image can be calculated by applying the chain rule

$$\frac{\delta \mathcal{L}_{\text{MDL}}}{\delta \mathbf{u}_i(\mathbf{x}_{ij})} = \frac{\partial \mathcal{L}_{\text{MDL}}}{\partial \lambda^m} \cdot \frac{\partial \lambda^m}{\partial \Sigma_{jl}} \cdot \frac{\delta \Sigma_{jl}}{\delta \mathbf{S}_i(\mathbf{x}_{ij})} \cdot \frac{\delta \mathbf{S}_i(\mathbf{x}_{ij})}{\delta \mathbf{u}_i(\mathbf{x}_{ij})}, \quad (4.31)$$

where Einstein summation convention applies to the repeated subscripts m, j, l .

The partial derivative of the cost function with respect to the eigenvalues is

$$\frac{\partial \mathcal{L}_{\text{MDL}}}{\partial \lambda^m} = \begin{cases} \frac{1}{\lambda_m} & \text{if } \lambda_m \geq \lambda_c, \\ \frac{1}{\lambda_c} & \text{if } \lambda_m < \lambda_c. \end{cases} \quad (4.32)$$

The partial derivative of the eigenvalue with respect to the element of covariance matrix Σ_{jl} is calculated from the eigen-decomposition

$$\Sigma = \mathbf{W} \Lambda \mathbf{W}^T, \quad (4.33)$$

where Λ is the diagonal matrix of eigenvalues, and \mathbf{W} is the matrix of eigenvectors, which gives the derivative

$$\frac{\partial \lambda^m}{\partial \Sigma_{jl}} = W_{jm} W_{lm}, \quad (4.34)$$

where W_{lm}, W_{jm} are elements of \mathbf{W} . The variation of the covariance matrix with respect to the position of the point $S_i(\mathbf{x}_{ij})$ is derived from (4.29)

$$\frac{\delta \Sigma_{jl}}{\delta S_i(\mathbf{x}_{ij})} = \frac{1}{(2N+1)^2} \left[\left(\delta_{ij} - \frac{1}{n} \right) S_l(\mathbf{x}_{ij}) + \left(\delta_{il} - \frac{1}{n} \right) S_j(\mathbf{x}_{ij}) \right] \in \mathbb{R}^{1 \times 3}. \quad (4.35)$$

The variation of the point $S_i(\mathbf{x}_{ij})$ with respect to the displacement \mathbf{u}

$$\begin{bmatrix} \delta S_i(\mathbf{x}_{ij}) \\ \delta \mathbf{u}_i(\mathbf{x}_{ij}) \end{bmatrix} \in \mathbb{R}^{3 \times 2} \quad (4.36)$$

can be calculated on the image S_i by interpolation.

4.1.3.3 Fluid regularization

Since the groupwise optimization of \mathcal{L}_{MDL} is generally ill-posed, regularization of the solution is required. Modeling the deformation as viscous fluid, fluid registration method (Christensen et al., 1996) has been used by Davies et al. (2008b) in solving the deformation \mathbf{u} . The external force is calculated from the variation of the object function

$$\mathbf{F}_i(\mathbf{x}_{ij}) = -\frac{\delta \mathcal{L}_{\text{MDL}}}{\delta \mathbf{u}_i(x_{ij})}. \quad (4.37)$$

which drives the velocity field \mathbf{v} described by the Navier-Lamé equation for the steady state defined by the Navier-Lamé operator L

$$L[\mathbf{v}] \equiv -\mu \nabla^2 \mathbf{v} - (\mu + \lambda) \nabla(\nabla \cdot \mathbf{v}) = \mathbf{F}. \quad (4.38)$$

where μ and λ are the Lamé coefficients, which are set to be equal in our application. The Navier-Lamé equation (4.38) is solved using an LU decomposition by Davies et al. (2008b). The solvability of the boundary value problems for the system has been discussed by Dahlberg et al. (1988). A fast solution to the viscous fluid PDE using discrete Fourier transform has been proposed by Bro-Nielsen and Gramkow (1996) to solve the equation under the sliding boundary condition, i.e. the normal components of \mathbf{v} on the boundary ∂D vanishes, while the tangential components are undetermined.

Since the boundaries of the shape image are cut from the original parameterization (sphere or octahedron), we expect the boundary to be fixed in the reparameterization. To solve the reparameterization on the shape image, the Navier-Lamé system (4.38) is to be considered in conjunction with zero Dirichlet boundary condition, also known as the ‘no-slip’ condition

$$\mathbf{v}|_{\partial D} = \mathbf{0}. \quad (4.39)$$

A fast solver to the boundary value problem of Navier-Lamé system under Dirichlet boundary condition based on discrete sine transform (Martucci, 1994) has developed by Cahill et al. (2007). The adjoint of the operator in matrix form

$$\mathbf{L}^\dagger = -\mu \nabla^2 - (\mu + \lambda) \begin{pmatrix} \frac{\partial^2}{\partial y^2} & -\frac{\partial^2}{\partial x \partial y} \\ -\frac{\partial^2}{\partial x \partial y} & \frac{\partial^2}{\partial x^2} \end{pmatrix} \quad (4.40)$$

is multiplied to both side of the equation (4.38)

$$\mathbf{L}^\dagger \mathbf{L}[\mathbf{v}] = \det(\mathbf{L})[\mathbf{v}] = \mathbf{L}^\dagger[\mathbf{F}] \quad (4.41)$$

where the matrix determinant of \mathbf{L} has the form

$$\det(\mathbf{L}) = \mu(2\mu + \lambda) \nabla^2 \nabla^2. \quad (4.42)$$

The sinusoidal waves on D

$$\omega_{a,b}(\mathbf{x}) = \sin a\pi x \sin b\pi y, \quad \mathbf{x} = (x, y) \in D, \text{ and } a, b \in \mathbb{N}, \quad (4.43)$$

are the eigen-functions of $\det(\mathbf{L})$ under the ‘no-slip’ condition (4.39), which motivates the fast solution of the boundary value problem via discrete sine transform listed in Algorithm 8.

Algorithm 8 Solving the velocity field with fluid regularization on shape image. Adapted from Cahill et al. (2007).

- 1: Compute $\mathbf{L}^\dagger[\mathbf{F}](\mathbf{x}_{i,j}), \forall i, j = 1, 2, \dots, 2N + 1$ by direct convolution of \mathbf{F} with linear differential filter
- 2: Compute the discrete sine transform $\tilde{\mathbf{F}}(a, b)$ of $\mathbf{L}^\dagger[\mathbf{F}]$
- 3: Compute the coefficients

$$\tilde{\mathbf{v}}(a, b) \leftarrow \frac{\tilde{\mathbf{F}}(a, b)}{4\mu(2\mu + \lambda) \left(\cos\left(\frac{a\pi}{2N}\right) + \cos\left(\frac{b\pi}{2N}\right) - 2 \right)^2}$$

- 4: Compute the velocity $\mathbf{v}(\mathbf{x}_{i,j})$ from the inverse discrete sine transform of $\tilde{\mathbf{v}}(a, b)$.
-

4.1.3.4 Optimization process

Once the velocity \mathbf{v} is solved, the update of \mathbf{u} follows the Eulerian derivative

$$\dot{\mathbf{u}}(\mathbf{x}, \tau) = \mathbf{v}(\mathbf{x}, \tau) - (\mathbf{v} \cdot \nabla)\mathbf{u}(\mathbf{x}, \tau), \quad (4.44)$$

which gives the increment of \mathbf{u} in each time step τ

$$\tau(\mathbf{v}_i - (\mathbf{v}_i \cdot \nabla)\mathbf{u}_i). \quad (4.45)$$

In the process of optimization, re-gridding is performed to avoid folding (Christensen et al., 1996). The Jacobian in folded deformation is negative, thus the condition of performing re-gridding is determined by checking the Jacobian of the deformation. If the deformation of any shape image leads to the local Jacobian below a positive threshold, the regrid is performed by reparameterizing all the shape images based on the current \mathbf{u}

$$S'_i(\mathbf{x}) = S_i(\mathbf{x} - \mathbf{u}_i(\mathbf{x})) \quad (4.46)$$

and the displacement \mathbf{u} is reset. In order to avoid the bias due to the choice of the orientation of the octahedron in cutting and unfolding, the octahedron parameterization is periodically reoriented and unfolded to the plane. The 6 possible orientations (~ 6 vertices of the octahedron) and the unfolding are shown in Figure 4.7. The algorithm of groupwise optimization for shape images is listed in Algorithm 9.

4.1.4 Validation and evaluation of shape models

For reparameterized shape surfaces $\{f_i \circ \gamma_i, i = 1, \dots, n\}$ or image representation $\{S_i \circ \psi_i, i = 1, \dots, n\}$, each shape surface is sampled and represented in SSM by a vector concatenating the coordinates of sampled points

$$X_i = \left(x_i^1, y_i^1, z_i^1, x_i^2, y_i^2, z_i^2, \dots, x_i^k, y_i^k, z_i^k \right)^T \in \mathbb{R}^{3k}, \quad (4.47)$$

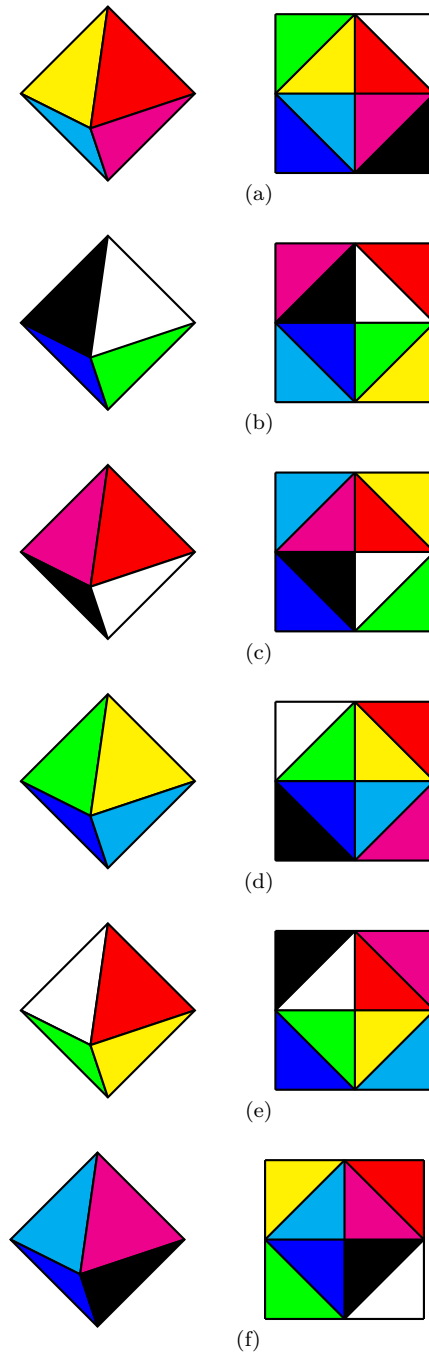


FIGURE 4.7: Six possible choices of reorientation and unfolding of the octahedron. The octahedron is cut in the manner of Figure 4.4. Left column: 6 re-orientations; right column: the unfolding. The faces unfolded are color coded.

Algorithm 9 Groupwise optimization with fluid regularization. Adapted and modified from Davies et al. (2008b).

```

1: Initialize with  $\mathbf{u}_i \leftarrow 0, \mathbf{v}_i \leftarrow 0, i = 1, \dots, n$ .
2: while  $\mathbf{u}$  not converging do
3:   for all shapes images  $S_i, i = 1, \dots, n$  do
4:     Compute  $\mathbf{F}_i$  given  $\mathbf{u}_i$  (eq. 4.37)
5:     Compute  $\mathbf{v}_i$  given  $\mathbf{F}_i$  (eq. 4.41, Cahill et al., 2007)
6:     Update  $\mathbf{u}_i$ :  $\leftarrow \mathbf{u}_i + \tau(\mathbf{v}_i - (\mathbf{v}_i \cdot \nabla)\mathbf{u}_i)$  (eq. 4.45)
7:   end for
8:   if the minimum Jacobian of any  $\mathbf{u}_i$  is below threshold then
9:     for all shapes images  $S_i, i = 1, \dots, n$  do
10:       $S_i(\mathbf{x}) \leftarrow S_i(\mathbf{x} - \mathbf{u}_i)$  (eq. 4.46)
11:       $\mathbf{u}_i \leftarrow 0, \mathbf{v}_i \leftarrow 0$ 
12:    end for
13:   end if
14:   if reorientation required then
15:     for all shapes images  $S_i, i = 1, \dots, n$  do
16:       $S_i(\mathbf{x}) \leftarrow S_i(\mathbf{x} - \mathbf{u}_i)$  (eq. 4.46)
17:      reorient the octahedron unfolding  $g_i$ 
18:      update  $S_i$ 
19:       $\mathbf{u}_i \leftarrow 0, \mathbf{v}_i \leftarrow 0$ 
20:    end for
21:   end if
22: end while

```

where

$$(x_i^s, y_i^s, z_i^s)^T = f_i \circ \gamma_i(\theta_s, \phi_s) = S_i \circ \psi_i(\iota_s, j_s), \quad s = 1, 2, \dots, k \quad (4.48)$$

are the sampled points. For sampling on subdivided octahedron $k = 4N^2 + 2$. The mean

$$\bar{X} = \frac{1}{n} \sum_{i=1}^n X_i, \quad (4.49)$$

gives the data matrix

$$\mathbf{X} = (X_1 - \bar{X}, X_2 - \bar{X}, \dots, X_n - \bar{X}). \quad (4.50)$$

A PCA is performed such that each shape can be approximated by a subspace spanned by the eigenvectors of the larger covariance matrix

$$X = \bar{X} + \mathbf{W}\mathbf{b}, \quad (4.51)$$

where \mathbf{W} is the matrix which consists of all eigenvectors of $\mathbf{X}\mathbf{X}^T$, and \mathbf{b} is the vector describing the shape of X .

The SSM built upon the optimized correspondence is evaluated in terms of its compactness, generalization ability and specificity (Davies et al., 2003).

4.1.4.1 Compactness

The compactness of the SSM is measured by the cumulative variance of the first M variation modes of model

$$\text{Compactness}(M) = \frac{\sum_{m=1}^M \lambda_m}{\sum_{m=1}^{n-1} \lambda_m}, \quad (4.52)$$

where $\lambda_m, m = 1, \dots, n-1$ are the descendingly sorted eigenvalues of the covariance matrix Σ , with λ_1 the largest eigenvalue.

4.1.4.2 Generalization ability

The generalization ability of the SSM measures the ability of the model to represent an unseen shape. It is measured by a leave-one-out scheme

$$\text{Generalisability}(M) = \frac{1}{n} \sum_{i=1}^n \|X'_i(M) - X_i\|^2, \quad (4.53)$$

where $X'_i(M)$ is the reconstruction of the shape X_i by the model based on the training set excluding X_i with the first M modes, $\|\cdot\|$ is the L_2 -norm defined on the vector space.

4.1.4.3 Specificity

The specificity is the expected distance between the shapes generated by model and the shapes in the training set. It is evaluated by the generation shapes by the

SSM according to the variance in the shape space

$$\text{Specificity}(M) = \frac{1}{N} \sum_{j=1}^N \min_i \|X_j^*(M) - X_i\|^2, \quad (4.54)$$

where $X_j^*(M), j = 1, \dots, N$ are the samples generated by the model using the first M modes.

4.2 Extrapolation of testing cases

The estimation of parameters of an unseen shape requires a dense correspondence between the shape surface and the SSM in order to register the model, and map the shape to the legitimate subspace modeled by the SSM. The estimation result and the quality of the model reconstruction thus depend upon the accuracy of the correspondence between shape surfaces. In point set registration problems, the popular ICP algorithm estimates the transformation by minimizing the distance between two point sets based on the nearest neighbor correspondence. This method is sensitive to incorrect correspondences, and outliers need to be rejected in order to avoid local minima.

Instead of deterministic matching between two point sets, a Gaussian mixture model (GMM, Chui and Rangarajan, 2000; Jian and Vemuri, 2010) can be used to interpret the correspondence probabilistically as hidden random variables, and the maximum likelihood (ML) estimation of the transformation can be solved by Expectation-Maximization (EM) algorithm (Granger and Pennec, 2002). A symmetric formulation of the energy function has been proposed to achieve inverse consistency of the transformation (Combès and Prima, 2010). Previous work (Hufnagel et al., 2009) using EM-ICP has been developed for SSMs to estimate the model parameters with latent correspondences probabilities, and to build the shape model.

The EM-ICP framework is extended here to the estimation the shape parameters in PCA-based SSMs, and to improve the estimation by imposing symmetric

consistency and regularization on the estimator. Since PCA provides a linear parameterization of the variation and non-rigid deformation in the shape space, the formulation of symmetric data terms for consistent estimation has a closed form least square solution. The deformation of the shape model under the guidance of shape components also reduces significantly the dimension of the linear system. The shape parameters are associated with *a priori* distribution due to the statistical nature of SSM, which facilitates the extension of ML estimator to maximum *a posteriori* (MAP) by adding a Tikhonov regularization term.

4.2.1 Gaussian mixture model and EM algorithm

The point set registration problem is to transform the point set $\{\bar{\mathbf{p}}_X^s, s = 1, \dots, k\}$ of the model \bar{X} (the mean of the SSM in this case) to a target scene Y consisting of k_Y landmarks $\{\mathbf{p}_Y^t, t = 1, \dots, k_Y\}$. The Gaussian mixture model for point set registration models the transformed points $\mathcal{T}(\bar{X})$ as samples from a mixture of Gaussian distribution with mean at target points $\{\mathbf{p}_Y^t\}$

$$p(\mathcal{T}(\bar{X}), \mathbf{A}|Y) = \prod_{s,t} \left(\pi_{st} \cdot p(\mathcal{T}(\bar{\mathbf{p}}^s) | \mathbf{p}_Y^t) \right)^{A_{st}}, \quad (4.55)$$

where $p(\cdot | \mathbf{p}_Y^t)$ is the density of the Gaussian distribution in 3D, and $\mathbf{A} = (A_{st})$ is the binary matching matrix of which each entry $A_{st} = 1$ if point \mathbf{p}_Y^t corresponds to $\bar{\mathbf{p}}^s$ on the model with *a priori* probability

$$P(A_{st} = 1) = \pi_{st}, \quad \sum_t \pi_{st} = 1, s = 1, \dots, k. \quad (4.56)$$

By applying Bayes' rule, the distribution density of the matching matrix \mathbf{A} given the transformation \mathcal{T}

$$p(\mathbf{A} | \mathcal{T}(\bar{X}), Y) = \prod_{s,t} \left(\frac{\pi_{st} \cdot p(\mathcal{T}(\bar{\mathbf{p}}_X^s) | \mathbf{p}_Y^k)}{\sum_l \pi_{sl} \cdot p(\mathcal{T}(\bar{\mathbf{p}}_X^s) | \mathbf{p}_Y^l)} \right)^{A_{st}} \quad (4.57)$$

gives the conditional expectation

$$E(A_{st}|\mathcal{T}) = \frac{\pi_{st} \cdot p(\mathcal{T}(\bar{\mathbf{p}}_X^s)|\mathbf{p}_Y^k)}{\sum_l \pi_{sl} \cdot p(\mathcal{T}(\bar{\mathbf{p}}_X^s)|\mathbf{p}_Y^l)} \quad (4.58)$$

Viewing the correspondence matching matrix \mathbf{A} as hidden variable, EM algorithm can be used to minimize the free energy

$$F(\mathbf{A}, \mathcal{T}) = -E_{\mathbf{A}}(\log p(\mathcal{T}(\bar{\mathbf{x}}), \mathbf{A}|\mathbf{y})) + E_{\mathbf{A}}(\log p(\mathbf{A})). \quad (4.59)$$

In implementation, isotropic Gaussian noise with covariance $\sigma^2\mathbf{I}$ is assumed

$$p(\mathbf{p}'|\mathbf{p}) = \frac{1}{(2\pi)^{\frac{3}{2}}\sigma^3} \exp\left(-\frac{1}{2\sigma^2} \|\mathbf{p} - \mathbf{p}'\|^2\right) \quad (4.60)$$

where $\|\mathbf{p} - \mathbf{p}'\|$ is the Euclidean distance between the point \mathbf{p} and \mathbf{p}' . The prior distribution is set to be uniform

$$\pi_{st} = \frac{1}{k_Y}, \quad \forall s, t. \quad (4.61)$$

The EM algorithm estimates the latent match \mathbf{A} and the transformation \mathcal{T} alternatively. In the Expectation-step (E-step), the algorithm estimates the expectation of the match matrix \mathbf{A} based on the current estimate of \mathcal{T}

$$A_{st}^* = E(A_{st}|\mathcal{T}) = \frac{e^{-\|\mathcal{T}(\bar{\mathbf{p}}_X^s) - \mathbf{p}_Y^t\|^2/2\sigma^2}}{\sum_l e^{-\|\mathcal{T}(\bar{\mathbf{p}}_X^s) - \mathbf{p}_Y^l\|^2/2\sigma^2}}, \quad (4.62)$$

In the Maximization-step (M-step), the transformation \mathcal{T} is estimated by minimizing the energy

$$\mathcal{T}^* = \arg \min_{\mathcal{T}} \frac{1}{k\sigma^2} \sum_{s,t} A_{st}^* \left\| \mathcal{T}(\bar{\mathbf{p}}_X^s) - \mathbf{p}_Y^t \right\|^2, \quad (4.63)$$

where the transformation $\mathcal{T} = (T_A, \mathbf{b})$ is composed of an affine transformation T_A , and the deformation of the SSM along the vector \mathbf{b} (eq. 4.51)

$$\mathcal{T}(\bar{X}) = T_A(\bar{X} + \mathbf{W}\mathbf{b}) \quad \text{and} \quad \mathcal{T}(\bar{\mathbf{p}}_X^s) = T_A(\bar{\mathbf{p}}_X^s + (\mathbf{W}\mathbf{b})^s), \quad (4.64)$$

with $(\mathbf{W}\mathbf{b})^s \in \mathbb{R}^3$ indicating the displacement of the s -th model point given the vector \mathbf{b} .

Noting that \mathbf{A} is row-stochastic, i.e. $\sum_t A_{st}^* = 1$, it can be transformed into a least square estimation

$$\mathcal{T}^* = \arg \min_{\mathcal{T}} \sum_s \frac{1}{k\sigma^2} \|\mathcal{T}(\bar{\mathbf{x}}^s) - \mathbf{p}_{Y_c}^s\|^2 \quad (4.65)$$

where

$$Y_c = E(\mathbf{A}|\mathcal{T})Y \quad \text{and} \quad \mathbf{p}_{Y_c}^s = \sum_t A_{st}^* \mathbf{p}_Y^t \quad (4.66)$$

are the correspondence of model points \bar{X} in the scene Y weighted by the conditional expectation of \mathbf{A} . The optimization of \mathcal{T} in the M-step can be divided further into:

M.1 The least square estimation of deformation \mathbf{b}

$$\mathbf{b}^* = \arg \min_{\mathbf{b}} \sum_s \frac{1}{k\sigma^2} \|T_A(\bar{\mathbf{p}}_X^s + (\mathbf{W}\mathbf{b})^s) - \mathbf{p}_{Y_c}^s\|^2, \quad (4.67)$$

which has the least square solution $\mathbf{b}^* = \mathbf{W}^T(T_A^{-1}(Y_c) - \bar{X})$, where T_A^{-1} is the inverse of the affine component in the current estimation;

M.2 The least square estimation of the pose T_A

$$T_A^* = \arg \min_{T_A} \sum_s \|T_A(\bar{\mathbf{p}}_X^s + (\mathbf{W}\mathbf{b}^*)^s) - \mathbf{p}_{Y_c}^s\|^2. \quad (4.68)$$

The algorithm for deforming the SSM to fit the scene Y is listed in Algorithm 10.

4.2.2 Estimation with symmetrical consistency and shape priors

The energy function (4.63) to be minimized in **M.1** is asymmetric since it is the mean square distance from each point in $\mathcal{T}(\bar{X})$ to Y_c . Symmetrically, a mean square data term

$$\frac{1}{k_Y\sigma^2} \sum_{s,t} B_{ts}^* \|\mathcal{T}(\bar{\mathbf{p}}_X^s) - \mathbf{p}_Y^t\|^2 \quad (4.69)$$

Algorithm 10 EM-ICP estimation of the deformation and the pose of the SSM.

- 1: Estimate the pose T_A by ICP
 - 2: $\mathbf{b} \leftarrow \mathbf{0}$
 - 3: Initialization $\mathcal{T}^0 \leftarrow (T_A^0, \mathbf{b})$
 - 4: **while** \mathcal{T} not converged **do**
 - 5: {E-step}
 - 6: $\mathbf{A}^* \leftarrow E(\mathbf{A}|\mathcal{T})$ (eq. 4.62)
 - 7: {M-step}
 - 8: **for all** s **do**
 - 9: $Y_c \leftarrow \mathbf{A}^* Y$ (eq. 4.66)
 - 10: **M.1** $\mathbf{b} \leftarrow \mathbf{W}^T (T_A^{-1}(Y_c) - \bar{X})$
 - 11: **M.2** $T_A \leftarrow \arg \min_{T_A} \|T_A(\bar{X} + \mathbf{W}\mathbf{b}) - Y_c\|^2$ (eq. 4.68)
 - 12: **end for**
 - 13: **end while**
-

from each point in Y to $\mathcal{T}(\bar{X})$ can be added to the energy, where $\mathbf{B} = (B_{ts})$ is the row-stochastic match matrix, which is updated in the E-step

$$\mathbf{B}^* = E(\mathbf{B}|\mathcal{T}) \quad \text{and} \quad B_{ts}^* = E(B_{ts}|\mathcal{T}) = \frac{e^{-\|\mathcal{T}(\bar{\mathbf{p}}_X^s) - \mathbf{p}_Y^t\|^2/2\sigma^2}}{\sum_l e^{-\|\mathcal{T}(\bar{\mathbf{p}}_X^l) - \mathbf{p}_Y^t\|^2/2\sigma^2}}. \quad (4.70)$$

The formulation of SSM allows the shape priors based on the distribution of \mathbf{b} parameters $b_m \sim \mathcal{N}(0, \lambda_m)$, where λ_m is the m th eigenvalue of the covariance matrix. To include *a priori* information of parameters, a Tikhonov regularization term is added to the energy function, which penalizes the coefficients of the lesser components. Hence the cost function for symmetric consistent estimation with regularization

$$\begin{aligned} \mathcal{E} &= \frac{1}{2\sigma^2} \frac{1}{k} \sum_{s,t} A_{st}^* \left\| \mathcal{T}(\bar{\mathbf{p}}_X^s) - \mathbf{p}_Y^t \right\|^2 \\ &+ \frac{1}{2\sigma^2} \frac{\alpha}{k_Y} \sum_{s,t} B_{ts}^* \left\| \mathcal{T}(\bar{\mathbf{p}}_X^s) - \mathbf{p}_Y^t \right\|^2 \\ &+ \frac{\beta}{2} \sum_m \frac{b_m^2}{\lambda_m}, \end{aligned} \quad (4.71)$$

where α and β control the amount of symmetric consistency and regularization. Fixing the affine part T_A in \mathcal{T} , and noting that all rows in \mathbf{A} and \mathbf{B} sum to 1, the

cost function can be rewritten as

$$\begin{aligned}\mathcal{E} &= \frac{\|T_A\|}{2k\sigma^2} \|\bar{X} + \mathbf{W}\mathbf{b} - T_A^{-1}(Y_c)\|^2 \\ &+ \frac{\alpha\|T_A\|}{2k_Y\sigma^2} \|X_c - T_A^{-1}(Y) + \tilde{\mathbf{B}}\mathbf{W}\mathbf{b}\|^2 \\ &+ \frac{\beta}{2} \mathbf{b}^T \mathbf{\Lambda}^{-1} \mathbf{b},\end{aligned}\quad (4.72)$$

where $\|T_A\|$ is norm of the linear part of the affine transformation T_A , which is the scaling factor of T_A ,

$$X_c = \mathbf{B}^* X, \quad (4.73)$$

and $\mathbf{\Lambda}$ is the diagonal matrix of eigenvalues $\{\lambda_m\}$ of SSM. As opposed to $\mathbf{B} \in \mathbb{R}^{k_y \times k}$, $\tilde{\mathbf{B}} \in \mathbb{R}^{3k_Y \times 3k}$ is left multiplied to $\mathbf{W}\mathbf{b} \in \mathbb{R}^{3k}$, which is modified from \mathbf{B}^*

$$\tilde{\mathbf{B}} = \begin{pmatrix} B_{11}^* \mathbf{I}_{3 \times 3} & B_{12}^* \mathbf{I}_{3 \times 3} & \cdots & B_{1k}^* \mathbf{I}_{3 \times 3} \\ B_{21}^* \mathbf{I}_{3 \times 3} & B_{22}^* \mathbf{I}_{3 \times 3} & \cdots & B_{2k}^* \mathbf{I}_{3 \times 3} \\ \vdots & \vdots & \ddots & \vdots \\ B_{k_Y 1}^* \mathbf{I}_{3 \times 3} & B_{k_Y 2}^* \mathbf{I}_{3 \times 3} & \cdots & B_{k_Y k}^* \mathbf{I}_{3 \times 3} \end{pmatrix} \quad (4.74)$$

The minimum of the energy function is reached with the derivative

$$\frac{\partial \mathcal{E}}{\partial \mathbf{b}} = \mathbf{0}, \quad (4.75)$$

which is the solution to the linear system

$$\begin{aligned} \left(\frac{1}{k} \mathbf{I} + \frac{\alpha}{k_Y} \mathbf{W}^T \tilde{\mathbf{B}}^T \tilde{\mathbf{B}} \mathbf{W} + \frac{\sigma^2 \beta}{\|T_A\|} \mathbf{\Lambda}^{-1} \right) \mathbf{b} &= \frac{1}{k} \mathbf{W}^T (T_A^{-1}(Y_c) - \bar{X}) \\ &+ \frac{\alpha}{k_Y} \mathbf{W}^T \tilde{\mathbf{B}}^T (T_A^{-1}(Y) - X_c). \end{aligned} \quad (4.76)$$

To facilitate the computation of the term $\mathbf{W}^T \tilde{\mathbf{B}}^T \tilde{\mathbf{B}} \mathbf{W}$, sparsity on $\tilde{\mathbf{B}}$ can be imposed by restricting the search of correspondence in (4.70) within a neighborhood of radius ρ .

4.3 Experimental results

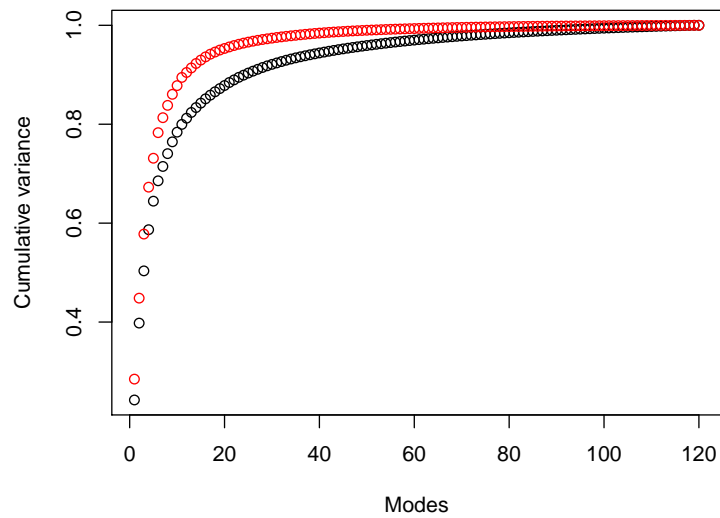
In the experiments, we first built SSMs for hippocampus based on the semi-automated segmentations from the ADNI database. The compactness, specificity and generalization ability of the result shape models were evaluated. Then we tested the performance of the EM-ICP based model extrapolation method we proposed. We compared the performance of the symmetric and asymmetric estimation both with and without regularization. The reconstruction error and the accuracy of the parameter estimation are evaluated.

4.3.1 SSM Building

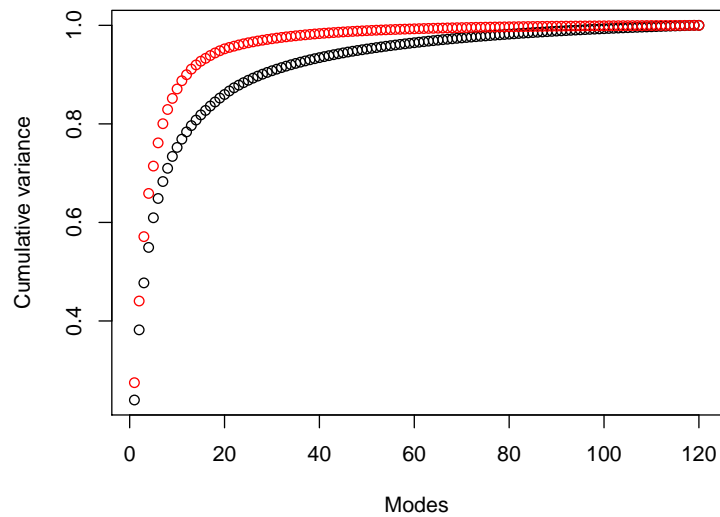
The hippocampal volumes used to build the SSMs were segmented semi-automatically by SNT provided by ADNI (see §3.4.2.1). The SSMs for right and left hippocampi were built on a training subset consisting of 60 AD subjects with average age 75.2(6.7) years old and 60 NC subjects with average age 77.0(4.8) years old. The correspondences of 4098 sampled landmarks in the SSMs were established by groupwise optimization described in the §4.1.

Examples of first 3 principal components of shape variation in left hippocampus is shown in Figure 4.11. The results of optimized SSMs are evaluated in terms of their compactness, specificity, and generalization ability. The compactness of the optimized SSM and the initial model is compared in Figure 4.8. For the left hippocampus, the 90% of the total variance is explained by the first 12 modes, 95% by the first 20 modes, and 98% by the first 36 modes in the optimized model. For the right hippocampus, the 90% of the total variance is explained by the first 13 modes, 95% by the first 20 modes, and 98% by the first 37 modes in the optimized model.

In the process of optimization, the information theoretic MDL is the object function to be minimized. As the MDL of the model decreases, the specificity and the generalization ability of the model improves as shown in Figures 4.9 and 4.10.

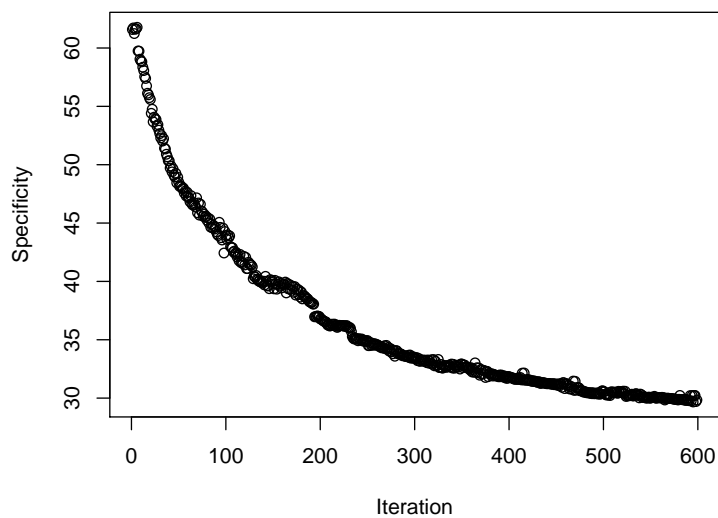


(a) Left hippocampus

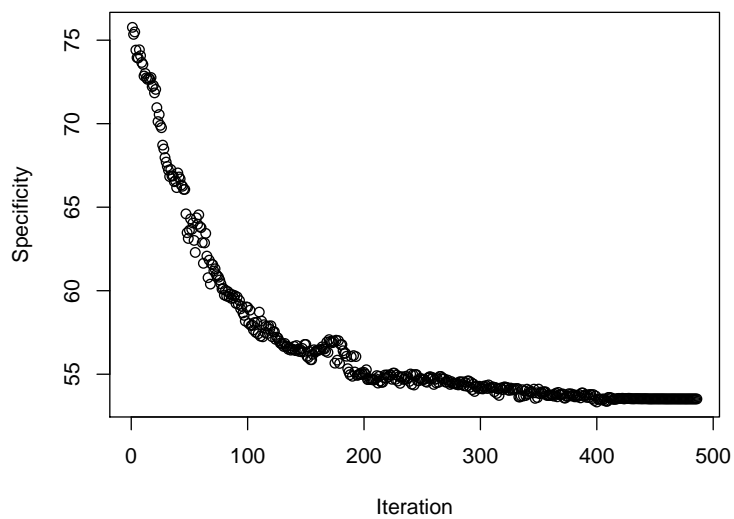


(b) Right hippocampus

FIGURE 4.8: The compactness of the Statistical Shape Model (SSM). The proportion of the total variance explained by the first principal components of the shape model. Red: optimized SSM, black: initial SSM.

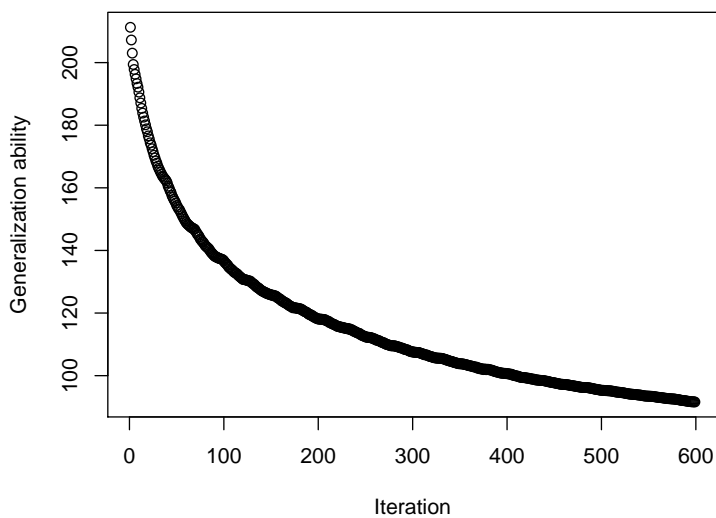


(a) Left hippocampus

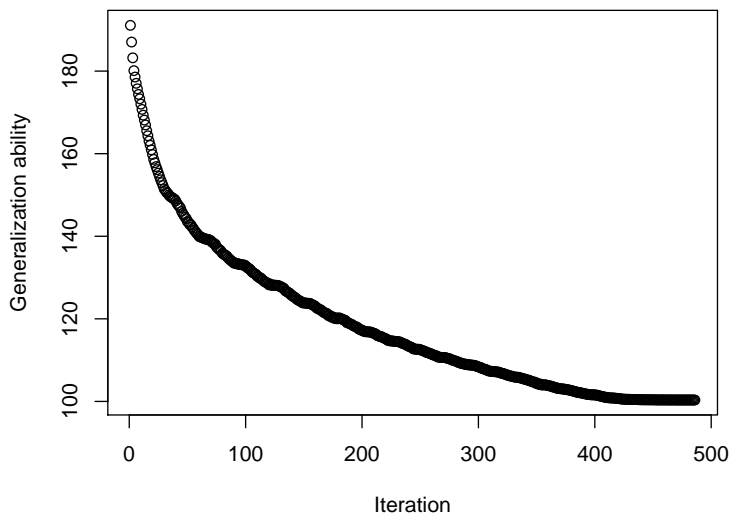


(b) Right hippocampus

FIGURE 4.9: The behavior of the $\text{Specificity}(M)$ in the groupwise optimization of the Statistical Shape Model (SSM), using the first $M = 15$ principal components, the number of trials in the simulation $N = 1000$.



(a) Left hippocampus



(b) Right hippocampus

FIGURE 4.10: The descendance of $\text{Generalisability}(M)$ in the groupwise optimization of the Statistical Shape Model (SSM), using the first $M = 15$ principal components.

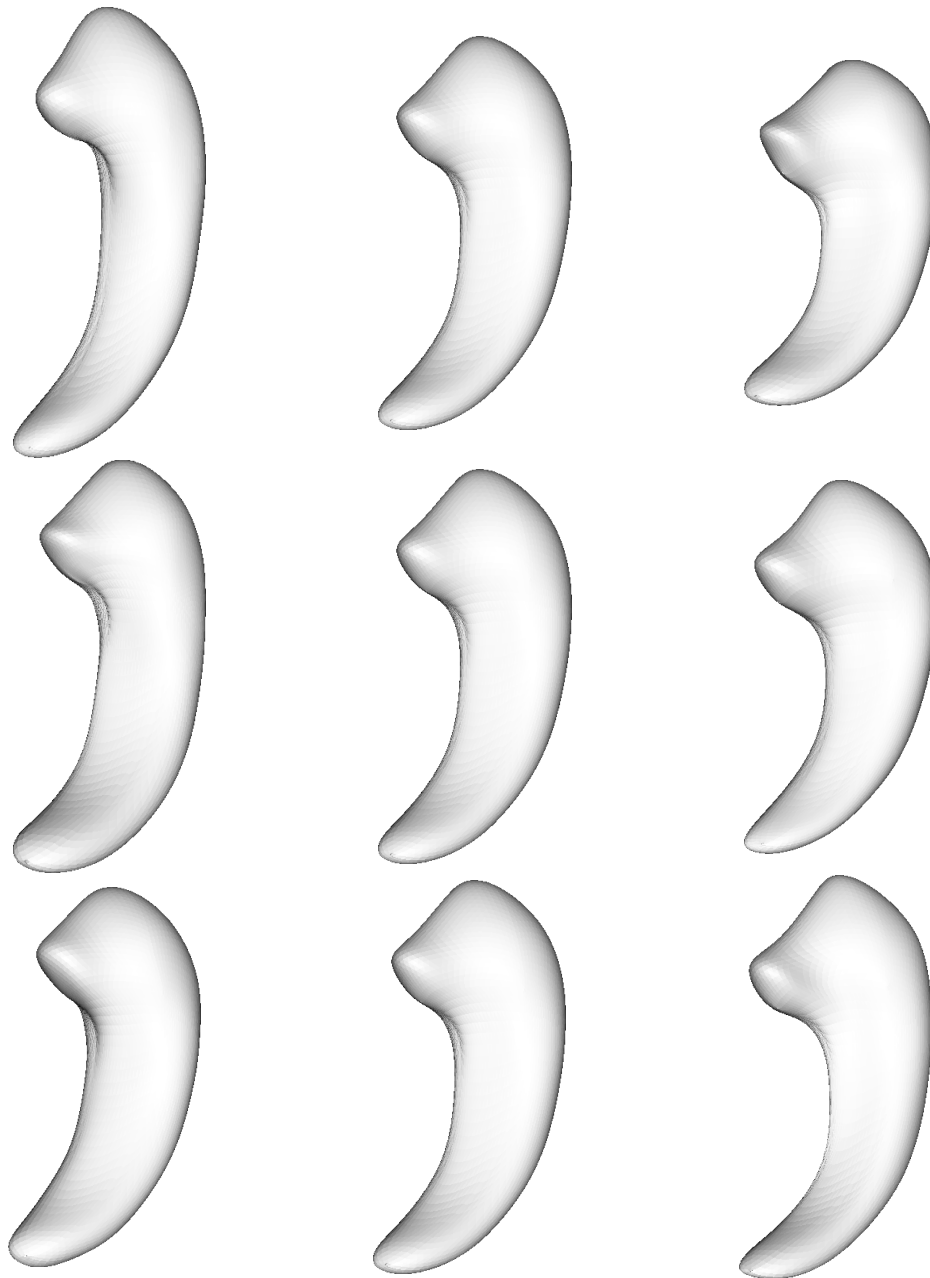


FIGURE 4.11: The shape variation in the first 3 modes of the left hippocampal shape model ($\pm 2\sqrt{\lambda_m}$, i.e. ± 2 standard deviations). Top row: the first mode; middle: the second mode; bottom row: the third mode. From left to right: variation mode with coefficient $-2\sqrt{\lambda_m}$, mean, variation mode with $2\sqrt{\lambda_m}$

4.3.2 SSM parameter estimation

We used the SSM of left hippocampus built previously in the experiments of model extrapolation and parameter estimation. We evaluate the effect of the symmetric consistency and regularization on the performance of the estimation by measuring the accuracy of the estimated shape parameters \mathbf{b} compared to the phantom ground truth, and the precision of the estimated shape surfaces. Two experiments were carried out, and in each of the experiments, we performed both the symmetric and asymmetric shape parameter estimation, with and without regularization.

In the first experiment, we aim to evaluate the accuracy of the estimated parameters by generating phantom samples from the SSM. The phantom shapes were generated by a random vector \mathbf{b} in which each component $b_m \sim \mathcal{N}(0, \lambda_m)$. Gaussian random noises ($0.05\|\mathbf{b}\|$) were added to the coordinates of surface points, and regularized by smoothing with a windowed sinc function (Taubin et al., 1996). These surfaces were further decimated (Garland and Heckbert, 1997), reducing 60% to 80% of triangles, to create missing correspondences between the phantom and the SSM, and match the density of marching cube meshes produced from hippocampal segmentations. The error of the estimation $\hat{\mathbf{b}}$ were measured by normalized mean squared error (MSE)

$$E(\|\hat{\mathbf{b}} - \mathbf{b}\|^2 / \|\mathbf{b}\|^2) = E\left(\frac{\sum_m (b_m - \hat{b}_m)^2}{\sum_i b_m^2}\right), \quad (4.77)$$

with respect to \mathbf{b} as the ground truth.

In the second experiment, we evaluated the precision of the estimated shapes by testing our method to represent smoothed marching cube surfaces obtained from an unseen testing set of hippocampal volumes (20 NC and 20 AD from ADNI). We deformed the SSM to fit the surfaces and measure the root mean square (RMS) error and the Hausdorff distance between SSM-reconstructed surface and the testing surface.

TABLE 4.1: Accuracy of shape parameter estimation. Normalized MSE of $\hat{\mathbf{b}}$, average of 40 randomly generated phantoms.

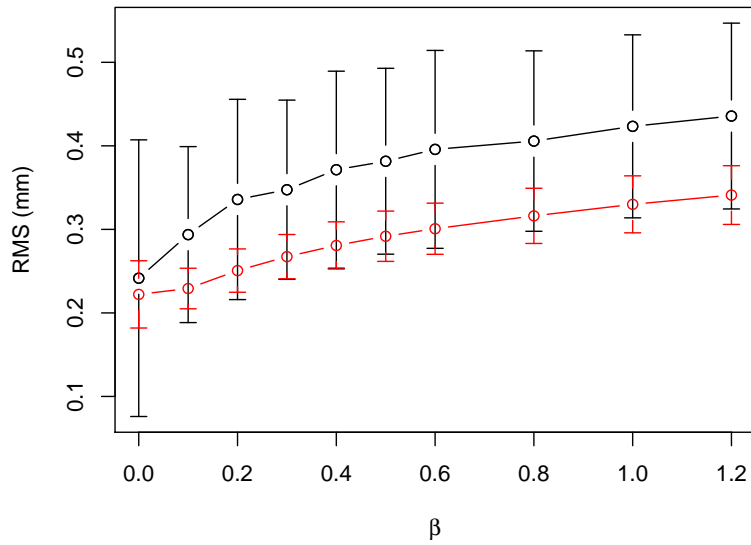
	60% decimation		80% decimation	
	Asymmetric	Symmetric	Asymmetric	Symmetric
w/o regularization	1.30	0.115	1.14	0.498
$\beta = 0.2$	0.117	0.078	0.117	0.103

4.3.3 Results and discussion

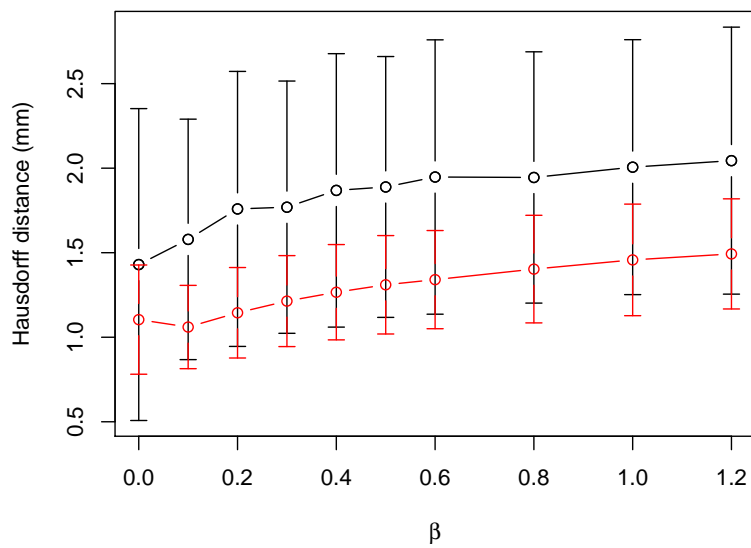
The results parameter estimation accuracy of first experiment are listed in Table. 4.1. The results of reconstruction precision in the second experiment are plotted in Figure 4.12. One example of reconstruction is shown in Figure 4.13 with the effect of regularization shown in Figure 4.14.

The formulation of shape parameter estimation as a least square problem results in the explicit optimization for the RMS error. Thus the lowest RMS error from the reconstruction based on asymmetric estimation without regularization is unsurprising. A closer look at one example (Figure 4.13(b)) reveals mismatch and inconsistent geometry in the regions with high-frequency of change and high-curvature details. The mismatch was corrected by the symmetric estimation, which ensures a mutually consistent match, and thus the Hausdorff distance between the reconstruction and the target was significantly reduced.

The closeness of reconstruction to the data based on un-regularized estimation may also be due to the effect of overfitting. It results in the foldings on the reconstructed surface, which can be seen for instance in Figure 4.14(a). This effect of folding and overfitting is eliminated by regularization, which takes the shape priors modeled by the SSM into account. With the presence of noise and occlusion of correspondence, the MAP (regularized) estimator provides more accurate estimates of shape parameters, while ML is more sensitive to the noise.



(a) RMS error



(b) Hausdorff distance

FIGURE 4.12: The precision of the model reconstruction with the estimated shape parameter. The errors were measured on the average of 40 unseen cases in the testing set. Black: Asymmetric estimator; red: symmetric estimator.

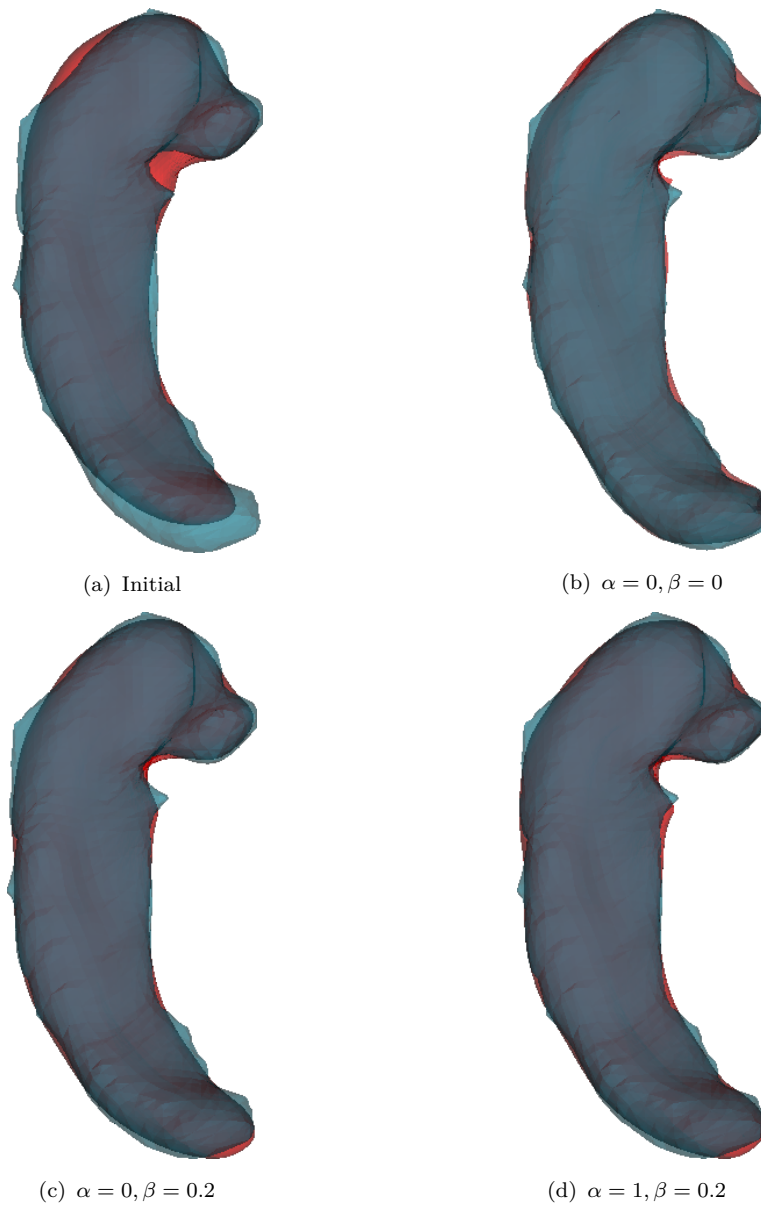


FIGURE 4.13: An example of reconstruction from estimated shape parameters. Blue: target shape surface; red: SSM generated reconstruction. (a) Mean shape with only similarity pose estimation. (b) RMS 0.173mm, Hausdorff distance 1.48mm. (c) RMS 0.211mm, Hausdorff distance 1.56mm. (d) RMS 0.188mm, Hausdorff distance 0.970mm.

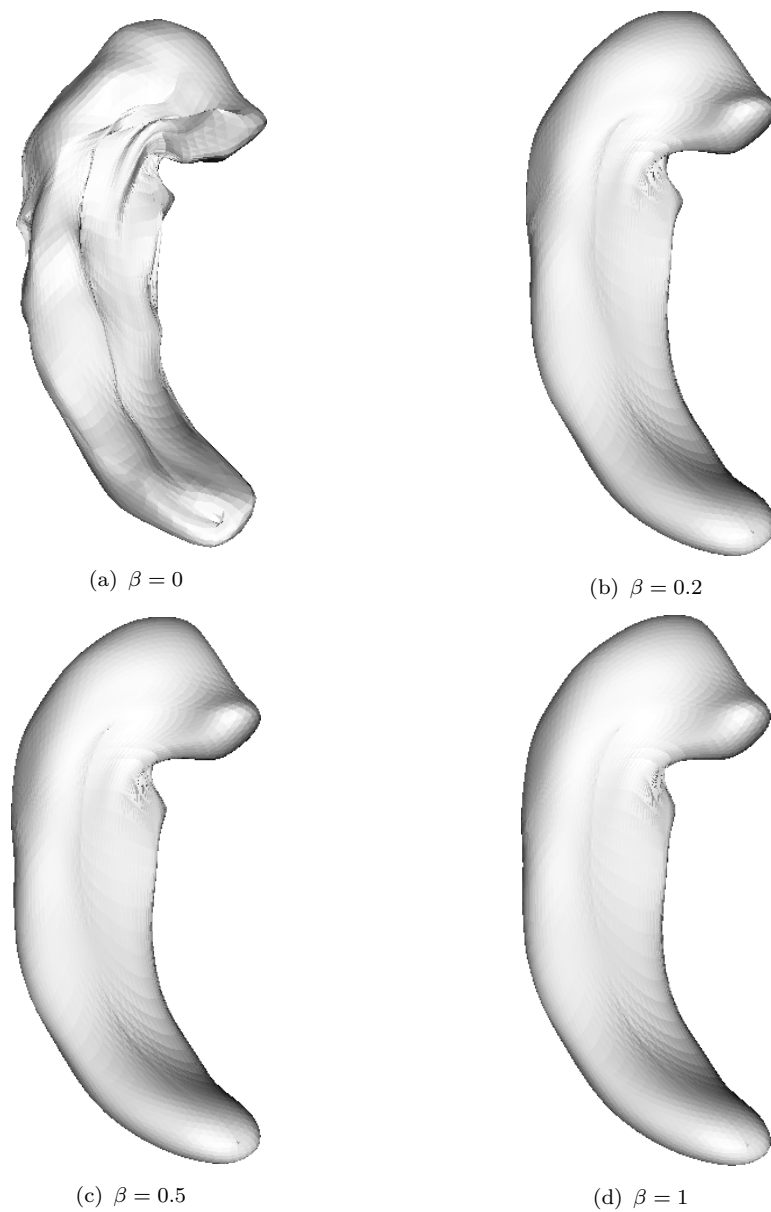


FIGURE 4.14: An example of regularization on symmetric shape parameter estimation. (a) RMS 0.188mm, Hausdorff distance 0.970mm (b) $\beta = 0.2$, RMS 0.186mm, Hausdorff distance 0.963mm. (c) RMS 0.220mm, Hausdorff distance 1.16mm. (d) RMS 0.253mm, Hausdorff distance 1.30mm.

4.4 Summary

In this chapter, we described the building of SSMs from the training shape data. The shape surfaces are first parameterized on a unit sphere by area-preserving mapping. The spherical parameterization of surfaces are then flattened to the shape image representation, which are re-parameterized to eliminate the spurious correspondences by groupwise optimization. The re-parameterization on the shape image is analogous to the non-rigid deformation in image registration, which is computed with fluid regularization. A fast algorithm solving fluid velocity using discrete sine transform is applied to regularize the shape reparameterization. The result SSM based on the correspondence in the parameter space is evaluated in terms of its compactness, generalization ability and specificity.

Once the SSM is built, it is used to estimate the shape parameters of unseen surfaces or point sets. An EM algorithm is used to estimate the transformation and the deformation of the model to fit the data with correspondence as the hidden variable. The data term to be optimized is symmetric between the model and the surface data in order to impose the consistency of the estimation. The SSM also provide the shape prior for the MAP estimator which includes a regularization term. The consistent symmetric estimation is shown to improve the details and the precision of the reconstruction of the shape surface from the model, and the shape prior regularization is necessary to avoid the problem of overfitting. With the presence of noises, mismatches, and disappearance of the correspondence, the regularized MAP gives more accurate estimation of shape parameters.

Quantitative shape analysis of hippocampus in AD

वर्णाकारप्रतिध्वानैर्नेत्रवक्त्रविकारतः ।

अप्यूहति मनो धीरास्[...]

Nārāyaṇa, *Hitopadeśa*, 3.34.

The hippocampus is affected at an early stage in the development of Alzheimer’s disease (AD). With the use of structural Magnetic Resonance (MR) imaging, we can investigate the effect of AD on the morphology of the hippocampus. The hippocampal shape variations among a population can be usually described using statistical shape models (SSMs). Conventional SSMs model the modes of variations among the population via principal component analysis (PCA). Although these modes are representative of variations within the training data, they are not necessarily discriminative on labeled data or relevant to the differences between the subpopulations. We use the shape descriptors from SSM as features to classify AD from normal control (NC) cases. A Hotelling’s T^2 test is performed to select a subset of landmarks which are used in PCA. The resulting variation modes are used as predictors of AD from NC. The discrimination ability of these predictors is evaluated in terms of their classification performances with bagged support vector machines (SVMs). Restricting the model to landmarks with better

separation between AD and NC increases the discrimination power of SSM. The predictors extracted on the subregions also showed stronger correlation with the memory-related measurements such as Logical Memory, Auditory Verbal Learning Test (AVLT) and the memory subscores of Alzheimer Disease Assessment Scale (ADAS).

The results of the localization of the SSM improving the discrimination of shape analysis have been previously partially published in “Increasing the discrimination power of shape analysis in Alzheimer’s disease detection by localized statistical shape model,” in *Alzheimer’s Association International Conference on Alzheimer’s Disease (ICAD)*, 2011, and “Detecting hippocampal shape changes in Alzheimer’s disease using statistical shape models,” in *Medical Imaging 2011: Image Processing*. Full results have been submitted to the journal *NeuroImage* for publication.

5.1 Overview of the method

We aim to extract hippocampal shape descriptors capturing both global and local shape changes linked to the AD pathology by SSM, so as to improve the performance of disease classification using additional shape information. We try to model the localized disease-related shape changes by performing the shape analysis upon the regions that are found to be affected by AD. We first identify the hippocampal surface subregions that are significantly different between the AD group and the controls via Hotelling’s T^2 test. Then we model the variations on these subregions using SSMs. Compared to the shape analysis of hippocampi via LoCA (Xie et al., 2009) which localizes the shape components while not specifically targeting the area related to the disease, we focus our shape analysis only on the regions that we marked as different, extracting the principal shape components on these regions. With the use of machine learning techniques, classifiers are able to learn the difference between AD and NC from the shape information as quantified by shape models. Extra information concerning AD pathology can be obtained by adding hippocampal shape descriptors in addition to the volumetry. We use the

morphological variation on these regions as variables to describe the AD pathology as they improve the discrimination between the classes and are correlated with the measures of memory decline associated with the disease.

We model the morphology of hippocampus by SSMs, and use the shape descriptors derived from the SSM to detect the effect of AD on the hippocampal size and its shape. Descriptors produced by different models serve as features for machine learning algorithms and are evaluated in terms of their prediction performance in distinguishing AD from NC.

The method used to extract relevant shape information from SSMs can be divided into two steps: 1) the localization step, and 2) the shape modeling step. The processing pipeline is shown in Figure 5.1. In the localization step, we build up the correspondence on hippocampal surface over a training set of both NC and AD subjects. Once the correspondence problem is solved, all the landmarks on the hippocampal surfaces are aligned by Procrustes analysis (Gower, 1975). A statistical test can be performed on each landmark to evaluate the significance of the difference between the distributions of aligned points of the NC group and the AD group.

The resulting significance map produced by the statistical tests in the localization step can be thresholded to obtain a surface mask of landmarks. In the shape modeling step, we apply these masks to the hippocampal surface to select a subset of hippocampal landmarks separating the subpopulations at a given statistical significance. The selected subregional landmarks are again aligned by Procrustes analysis and a PCA is performed on the aligned subregional landmarks. The coefficient of principal components describing local shape of hippocampus can thus be calculated.

In both the localization step and the shape modeling step, the shapes or selected shape patches are aligned by Procrustes analysis, which can be performed either through rigid-body transformations or through similarity transformations. In our experiments, both alignments are performed at each step and their performances are evaluated and compared. We evaluate the subregional shape models based

on their discrimination ability against the control group and the correlation with measures of cognition. The coefficients of modes describing the shape variations are used as features for disease classification, and the evaluation of the subregional models are based on the performance of the classifiers.

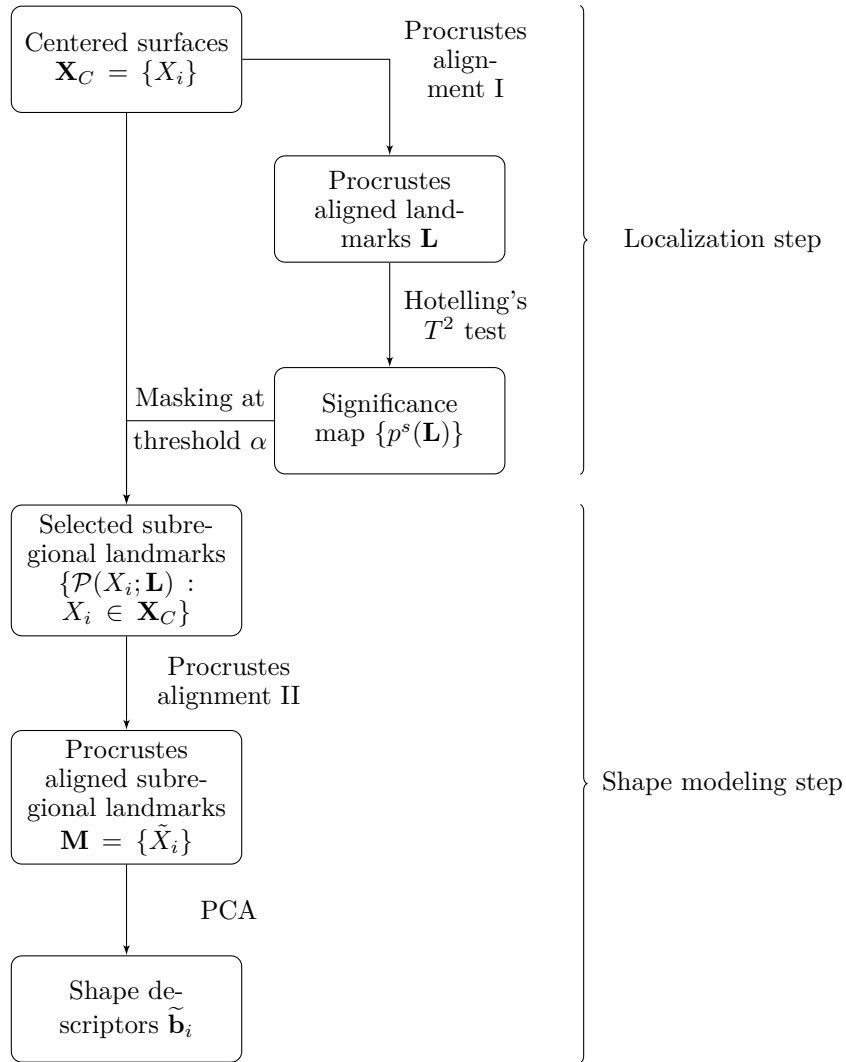


FIGURE 5.1: The pipeline of local shape descriptor extraction. The shape surfaces are first centered and aligned via Procrustes alignment I. A Hotelling's T^2 test is performed on each landmark of the aligned surfaces to obtain a significance mask, which is used to threshold the previously centered shape surfaces. The selected landmarks are aligned by Procrustes alignment II, and a Principal Component Analysis (PCA) is performed to extract the shape descriptors.

5.2 Shape analysis using SSM

The SSM for hippocampus is built upon a training set of hippocampal surfaces, in which the k landmarks on the surface of hippocampus are reparameterized to avoid the false variation induced by incorrect correspondences. This correspondence problem can be solved by a groupwise optimization and fluid regularization on the shape image (Davies et al., 2008b) as described in the §4.1.

Once the correspondence is established, the surfaces can be aligned by using Procrustes analysis, either through rigid-body or similarity transformations. The volume information is preserved after rigid body transformations. Procrustes analysis aligns the training data via rigid-body transformations to the size-and-shape space $S\Sigma_3^k$ in which the variation among the data would be driven by the change in both the size and the shape of hippocampus. If the training samples are aligned via isotropic similarity transformations, the surfaces will be rescaled to normalize the hippocampal volume. Thus we have the training set in the shape space Σ_3^k . As shape is defined as the remaining information ‘when the differences which can be attributed to translations, rotations, and dilations have been quotiented out’ (Kendall, 1984), the normalization of the volume by similarity transform enables the SSM to be more specific to the change in shape rather than incorporating variations in the sizes of hippocampi. The SSMs used are built on both rigid-body and similarity aligned surfaces.

For a set of hippocampal landmarks $\{X_1, X_2, \dots, X_n\}$ consisting of n samples with established correspondence, each sample is represented by the coordinates of its k landmarks concatenated as a $3k$ -vector

$$X_i = (x_i^1, y_i^1, z_i^1, x_i^2, y_i^2, z_i^2, \dots, x_i^k, y_i^k, z_i^k)^T \in \mathbb{R}^{3k}, \quad (5.1)$$

where $\mathbf{p}_i^s = (x_i^s, y_i^s, z_i^s)^T \in X_i$ is the position of the s -th sampled landmark point on the X_i . If the surfaces in $\{X_i, i = 1, \dots, n\}$ are aligned using Procrustes analysis, either rigidly or via isotropic similarity transformations, a PCA can be performed

on the data matrix (X_1, X_2, \dots, X_n) , and the shape data can be expressed as

$$X_i = \bar{X} + \mathbf{W}\mathbf{b}_i \quad (5.2)$$

where \bar{X} is the mean of $\{X_i\}$, \mathbf{W} is the matrix consisting of the eigenvectors of the covariance matrix of the training data, and the elements in vector \mathbf{b}_i are the parameters characterizing the i -th shape.

5.2.1 Localization step

In the localization step, we identify the regions affected by atrophy by analyzing the spatial distribution of each landmark across the training examples and the deformation between the two subpopulations. We begin with the set \mathbf{X}_C in which the correspondence over the training set is given and the landmarks are only Helmertized/centered without further alignment. We use Procrustes analysis to obtain an aligned ensemble \mathbf{L} of surfaces. For the k th landmark in \mathbf{L} , a Hotelling's T^2 test (Styner et al., 2007) can be used to assess the statistical significance of the landmark separating the NC from the AD group

$$p^s(\mathbf{L}) = P\left(T^2 > \frac{n_{\text{NC}} \cdot n_{\text{AD}}}{n_{\text{NC}} + n_{\text{AD}}} (\bar{\mathbf{p}}_{\text{NC}}^s - \bar{\mathbf{p}}_{\text{AD}}^s)^T s^{-1} (\bar{\mathbf{p}}_{\text{NC}}^s - \bar{\mathbf{p}}_{\text{AD}}^s)\right), \quad (5.3)$$

where $\bar{\mathbf{p}}_{\text{NC}}^s$ and $\bar{\mathbf{p}}_{\text{AD}}^s$ are the mean location of the s -th sampled landmark in each group, and

$$s = \frac{1}{n_{\text{NC}} + n_{\text{AD}} - 2} \left(\sum_{i \in \text{NC}} (\mathbf{p}_i^s - \bar{\mathbf{p}}_{\text{NC}}^s) (\mathbf{p}_i^s - \bar{\mathbf{p}}_{\text{NC}}^s)^T + \sum_{i \in \text{AD}} (\mathbf{p}_i^s - \bar{\mathbf{p}}_{\text{AD}}^s) (\mathbf{p}_i^s - \bar{\mathbf{p}}_{\text{AD}}^s)^T \right). \quad (5.4)$$

By thresholding the p -map $p^s(\mathbf{L})$, $s = 1, \dots, k$, we select only the subset of landmarks showing significant difference between NC and AD groups. This can be viewed as a projection \mathcal{P} of the shape surface to the regions more relevant to the

pathology

$$\begin{aligned} \mathcal{P}(\cdot; \mathbf{L}) : \mathbb{R}^{3k} &\mapsto \mathbb{R}^{3k'} \\ X &\mapsto (\tilde{x}^{s_1}, \tilde{y}^{s_1}, \tilde{z}^{s_1}, \tilde{x}^{s_2}, \tilde{y}^{s_2}, \tilde{z}^{s_2}, \dots, \tilde{x}^{s_{k'}}, \tilde{y}^{s_{k'}}, \tilde{z}^{s_{k'}})^T, \end{aligned} \quad (5.5)$$

which consists of $k' (< k)$ landmarks

$$(\tilde{x}^{s_i}, \tilde{y}^{s_i}, \tilde{z}^{s_i})^T \in \left\{ (x^s, y^s, z^s)^T \in X : p^s(\mathbf{L}) < \alpha \right\} \quad (5.6)$$

found to separate the NC from the disease group at significance level α .

Here the distribution of the surface landmarks depends on how the shapes in the SSM are aligned, and the variation between the subgroups will differ as rigid-body or similarity transformations can be chosen to align the shapes.

5.2.2 Shape modeling step

In the shape modeling step, instead of performing a PCA on the data consisting of all k landmarks of the surface, only the subset of landmarks identified as different between subpopulations in the localization step are used. We mask the Helmerized landmarks in \mathbf{X}_C and re-align the masked landmarks $\{\mathcal{P}(X_i; \mathbf{L}) : X_i \in \mathbf{X}_C\}$ by Procrustes analysis to form the training set

$$\mathbf{M} = \{\tilde{X}_i : \tilde{X}_i \text{ is Procrustes aligned } \mathcal{P}(X_i; \mathbf{L}), X_i \in \mathbf{X}_C\} \quad (5.7)$$

for the subregional SSM. A PCA is performed on \mathbf{M}

$$\tilde{X}_i = \bar{X}_M + \tilde{\mathbf{W}}\tilde{\mathbf{b}}_i \quad (5.8)$$

where \bar{X}_M is the mean of samples in \mathbf{M} , $\tilde{\mathbf{W}}$ is the matrix of eigenvectors describing the variation modes from significantly different landmarks, and $\tilde{\mathbf{b}}_i$ is the vector of coefficients of each mode.

5.3 Disease classification based on localized shape analysis

The shape descriptors from SSM are evaluated in terms of their performance when being used as features in classification algorithms. Support vector machines (SVMs, Vapnik, 1995) are widely used in solving general classification problems, and have been applied to AD diagnosis (e.g. Vemuri et al., 2008a; Kloppel et al., 2008, for review see Cuingnet et al., 2010). SVMs typically find the optimal hyperplane with the largest margin separating the classes. The computation of the optimal solution requires only the inner product of feature vectors which can be exploited by the substitution of a kernel for the inner product mapping the feature space to higher dimension (Schölkopf and Smola, 2002). We use the SVM classifier to test the discrimination ability of the features. We choose the radial basis function (RBF) as the kernel in SVM. The feature vector of each shape X for classification consists of the coefficient variation modes, as extracted from eq. (5.2) or (5.8).

In order to avoid modeling noise, less significant components produced by PCA are excluded from the feature set based on the assumption that these components tend to account more for noise than for meaningful shape information. Feature selection is usually required in classification tasks using SVM to reduce variance by eliminating the less relevant or noisier features, and to improve the classifier performance with fewer but more discriminative inputs. Commonly used wrapper methods for feature selection have the potential risk of overfitting the training data (Reunanen, 2003; Loughrey and Cunningham, 2005). The heuristic strategies searching for an optimal subset of features may select a combination not generalizing well on a separate test set. Since the aim of this study is to evaluate the prediction performance of different categories of shape descriptors, the performance of the classifier on a selected subset of features (not guaranteed to be optimal either on the training or the test set) does not represent the overall discriminant ability of the features derived from different shape models. It is therefore preferable to adopt a methodology that takes into account all features in order to assess the respective model that produces these features.

Bootstrap aggregation, or bagging (Breiman, 1996a), is another approach to reduce the variance in the learning algorithm. It is based on the repeating bootstraps of the training set, and trains the classifier using the resampled data. Multiple classifiers learned from the resampled data are often combined by a majority voting. When bagging is used, better performance is usually achieved with larger feature set without discarding weakly informative features (Munson and Caruana, 2009). We thus can train bagged classifier on the whole set of features to be evaluated and use the prediction performance of the bagged classifier as a measurement of the discriminant ability of the feature set.

In addition to the shape variations, the hippocampal volume normalized by the total intracranial volume (TIV) are used as independent feature. To compare the discrimination ability of the volume and the shape of the hippocampus, we evaluate the classification performance of shape descriptors both with and without the normalized volume feature. The TIV is calculated by summing the volume of white matter (WM), grey matter (GM) and cerebrospinal fluid (CSF). For each subject, the T1- and T2-weighted MR images were classified into WM, GM and CSF using an implementation of the expectation maximization segmentation algorithm (Acosta et al., 2009). In brief, this algorithm models the image intensity histogram using a mixture of Gaussian distribution. The parameters of the Gaussian mixture are iteratively updated using an expectation maximization approach. For this study, 6 Gaussian distributions were used: 1 for each of the main tissue types, namely WM, GM, and CSF, and 3 for non-brain tissues. To provide initialization and spatial consistency to the expectation maximization algorithm, a template and associated probability maps of GM, WM, and CSF were spatially normalized to each individual scan, first through an affine registration using a robust block matching approach (Ourselin et al., 2001) with 12 degrees of freedom, and then using a diffeomorphic demons nonrigid registration (Vercauteren et al., 2009). The expectation maximization algorithm computed probability maps for each tissue type, which were discretized by assigning each voxel to its most likely tissue type.

The data set used to train the classifier was resampled with replacement for 25 times, and the ensemble of classifiers consisted of SVMs with RBF kernel each of which were trained on the resampled data. The cost parameter C and the scale parameter of the kernel γ are not explicit parameters for the ensemble classifier, but parameters of individual SVMs in the ensemble. For each individual SVM, both C and γ are tuned by a grid search over the range $C = 2^{-7}, 2^{-6}, \dots, 2^2, 2^3$ and $\gamma = 2^{-2}, 2^{-1}, \dots, 2^7, 2^8$ using the resampled training set with 10-fold cross validation. The parameters giving the best performance on the resampled training data are chosen for the SVM. Each SVM in the ensemble may have different values of C and γ parameters. The predictions of 25 SVMs were combined by a voting rule to produce the final output. The validation on the training set with varying the threshold α , and experiments using separated training and testing sets were performed.

We use the out-of-bag estimation (OOB, Breiman, 1996b) to evaluate the performance of the bagging classifier on the training set. For each resample of the training data with replacement, there are approximately one-third of the training data left out of the bootstrap resampling. A classification of each left-out (i.e. ‘out-of-bag’) case can be obtained from the SVM trained using the selected (i.e. ‘in-bag’) sample. The classification of each case in the training set can be determined by a voting rule after multiple runs of resampling. The OOB estimation can be obtained from average accuracy on the left-out data. In our experiment, the OOB estimates are carried out by 70 resamplings, which result in each training case being left out and classified for approximately 25 times on average.

In order to compare with the disease classification result reported by Cuingnet et al. (2010) using hippocampal shape information (Gerardin et al., 2009), experiments using the linear C-SVM on SSM features were also carried out. The cost parameter C was chosen by searching over the range $10^{-5}, 10^{-4.5}, \dots, 10^{2.5}, 10^3$ and leave-one-out cross validation on the training set, in the same manner as in Cuingnet et al. (2010).

5.4 Correlating the shape variation with memory performance

Hippocampus plays a critical role in memory formation, and its atrophy is associated with memory decline in AD (Heun et al., 1997; Petersen et al., 2000). We assessed our global and local hippocampal SSMs in terms of their relevance to memory decline by the correlation analysis between the shape descriptors derived from these models and the scores from memory tests. The results from Logical Memory test (immediate and delayed recall), Auditory Verbal Learning Test (AVLT, 30-minute delay, Ivnik et al., 1992), and the memory subscores of Alzheimer Disease Assessment Scale (ADAS, including word recall, delayed word recall, orientation, word recognition and recall instructions) were chosen as the measurements of memory performance. Spearman's correlation coefficient ρ was used to compare the hippocampal shape variation with the memory scores, which were corrected for age in the experiments. For comparison, we also project the shape samples onto the direction of mean difference $\bar{X}_{NC} - \bar{X}_{AD}$, and perform the correlation analysis between the memory scores and the shape component along the mean difference direction.

5.5 Experimental Results

5.5.1 Materials

The hippocampal volumes used in the experiments are segmented semi-automatically by SNT provided by ADNI (see §3.4.2.1). The hippocampal volumes were divided into a training set and a testing set. The demographic information is listed in Table 5.1.

5.5.2 SSM

Based on the choice of the transformations aligning the surfaces in the localization step and in the shape modeling step, we can derive the variation modes of the

TABLE 5.1: Demographic information of subjects used in the study.

	Diagnosis	Number (M/F)	Age	Yeas of education
Training set	NC	34/26	77.0(4.8)	16.3(2.7)
	AD	31/29	75.2(6.7)	14.7(3.0)
Testing set	NC	35/43	76.3(5.2)	15.4(3.1)
	AD	20/19	77.8(7.3)	14.4(3.7)
Total	NC	69/69	76.6(5.0)	15.8(2.9)
	AD	51/48	76.2(7.0)	14.6(3.3)

hippocampal shapes in different ways. The combinations of alignment in the SSMs are listed in Table 5.2.

TABLE 5.2: Choices of alignment in SSMs

		Procrustes alignment II in shape modeling	
		\mathbf{M}_R	\mathbf{M}_S
Procrustes alignment I in localization	\mathbf{L}_R	1	2
	\mathbf{L}_S	3	4

1. In the localization step, the significance maps are produced from rigidly aligned size-and-shape set \mathbf{L}_R , and in the shape modeling step the subregional SSM is built on rigidly aligned the size-and-shape set \mathbf{M}_R ;
2. in the localization step, the significance maps are produced from rigidly aligned size-and-shape set \mathbf{L}_R , and in the shape modeling step the subregional SSM is built on similarity aligned the shape set \mathbf{M}_S ;
3. in the localization step, the significance maps are produced from similarity aligned shape set \mathbf{L}_S , and in the shape modeling step the subregional SSM is built on rigidly aligned the size-and-shape set \mathbf{M}_R ;
4. in the localization step, the significance maps are produced from similarity aligned shape set \mathbf{L}_S , and in the shape modeling step the subregional SSM is built on similarity aligned the shape set \mathbf{M}_S .

In the experiments, the hippocampi on both the right and the left hand sides of 60 NC and 60 AD subjects from ADNI data were used as a training set to build the SSM. Hotelling's T^2 test was performed on each SSM between the AD and NC groups, with the resulting significance maps shown in Figure 5.2. The results after the thresholding are shown in Figure 5.3.

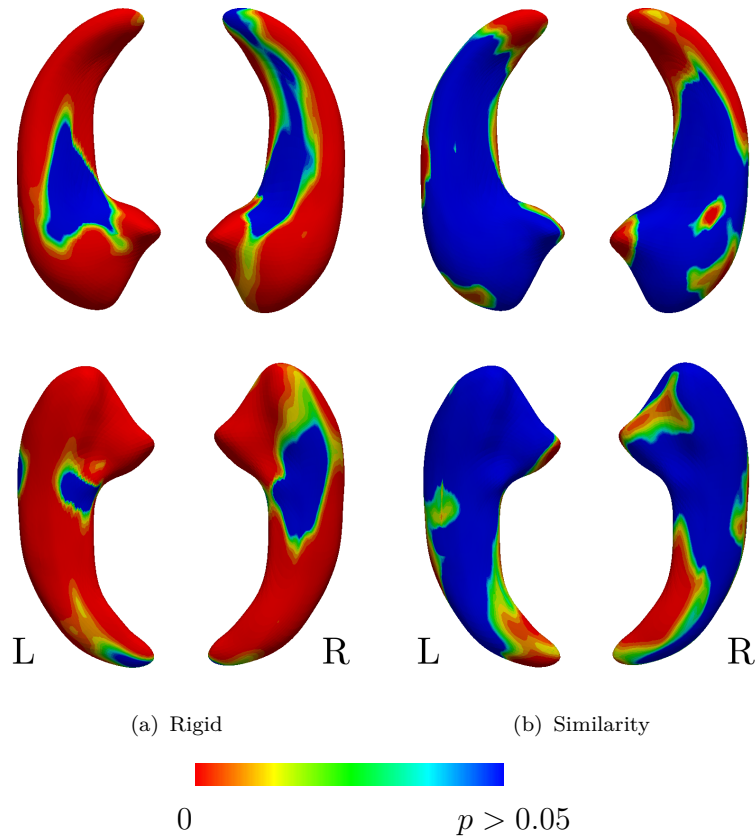


FIGURE 5.2: The significance map of local difference on hippocampal surface by Hotelling's T^2 test. For each landmark in the training set, a Hotelling's T^2 test is carried out between the normal control (NC) group, and the Alzheimer's disease (AD) group, resulting the map of p -values. Top: superior view; bottom: inferior view.

We vary the thresholds of the significance level when selecting the landmarks at $\alpha = 0.0001, 0.0002, \dots, 0.0009, 0.001, 0.002, \dots, 0.009, 0.01, 0.02, \dots, 0.09, 0.1, 0.2, \dots, 0.9$. The number of landmarks thresholded at each significance level is plotted in Figure 5.4. For the purpose of comparison, conventional PCA on all the landmarks was also performed, using models \mathbf{M}_R and \mathbf{M}_S .

5.5.3 Disease classification of AD using regional SSM

The first 15 principal components in each of the SSM were used as features for classification, which accounted for approximately 90% of the total variance in the training set (Heimann and Meinzer, 2009). The rest of the modes individually

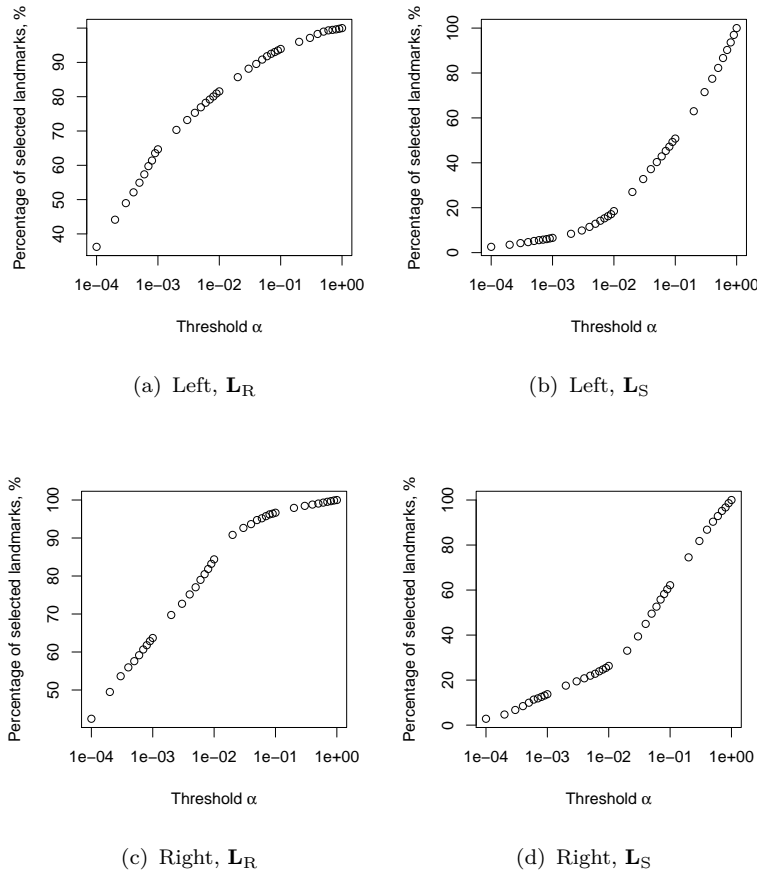


FIGURE 5.4: The percentage of landmarks selected, with varying thresholds in the landmark selection on the significance map of Hotelling's T^2 test.

plotted in 5.9 and 5.10.

As a baseline, using only the TIV normalized volume gave 77.6%(OOB), 83.5%(testing set) accuracy. The best OOB performance on the training set (81.2% accuracy) is achieved using rigid-body aligned SSM (\mathbf{M}_R) on the selected landmarks ($\mathbf{L}_S, \alpha = 0.01$) with additional volume feature. On the separate testing set the highest accuracy is 88.9% ($\mathbf{M}_R, \mathbf{L}_S, \alpha = 0.09$).

With the features produced by SSMs alone, the best OOB accuracy is 81.5%, using the localized SSM ($\mathbf{M}_R, \mathbf{L}_S, \alpha = 0.01$), and the accuracy on the testing set reaches 87.6% ($\mathbf{M}_R, \mathbf{L}_S, \alpha = 0.1$) The result of the linear C-SVM with this set of SSM features ($\mathbf{M}_R, \mathbf{L}_S, \alpha = 0.1$) gave 71.8% sensitivity and 94.9% specificity, which is comparable to the result of 69% sensitivity and 84% specificity reported by Cuingnet et al. (2010).

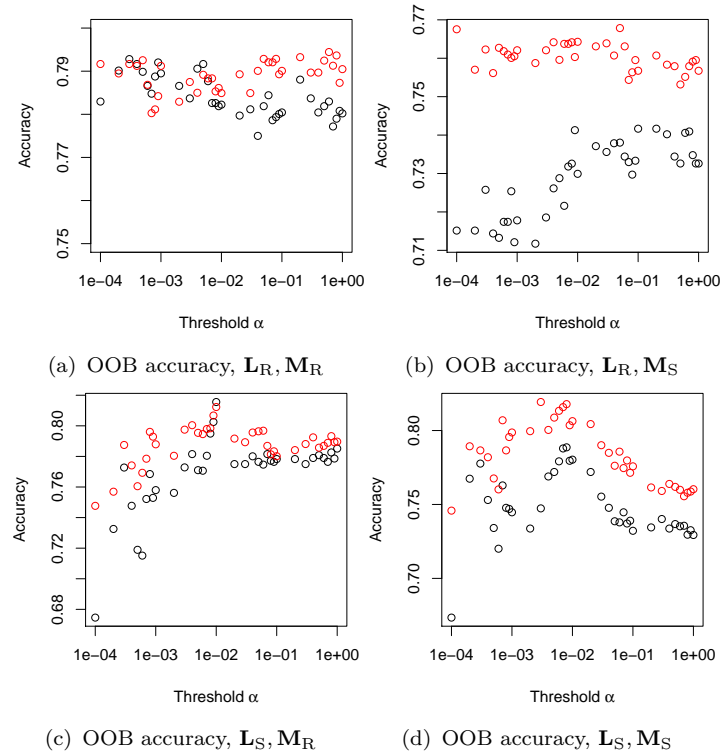


FIGURE 5.5: The training accuracy of the disease classification using bagged support vector machines (SVMs) with varying thresholds in the landmark selection. The out-of-bag (OOB) estimates is used for the measure of the training error. Black circles: shape features from the Statistical Shape Model (SSM) only; red circles: shape features with additional volume features.

5.5.4 Correlation of hippocampal SSM descriptors with memory scores

The results of the correlation between the memory scores and the hippocampal shape variation over all landmarks, landmarks selected with threshold $\alpha = 0.1$, and threshold $\alpha = 0.01$ are shown in Figure 5.11. The component in each SSM with the strongest correlation with the memory scores are plotted. The principal variations in the model on the selected subregions are shown to be better correlated with memory scores. Stronger correlations were found by the models built on \mathbf{L}_S identified regions. The highest correlation between the memory score and the hippocampal shape was captured by similarity aligned SSM (\mathbf{M}_S) on the hippocampal subregions masked using \mathbf{L}_S with threshold at $\alpha = 0.01$, in which the first principal component was the most correlated component with AVLT, Logical Memory scores (both immediate and delayed recall), and memory subscores of ADAS for

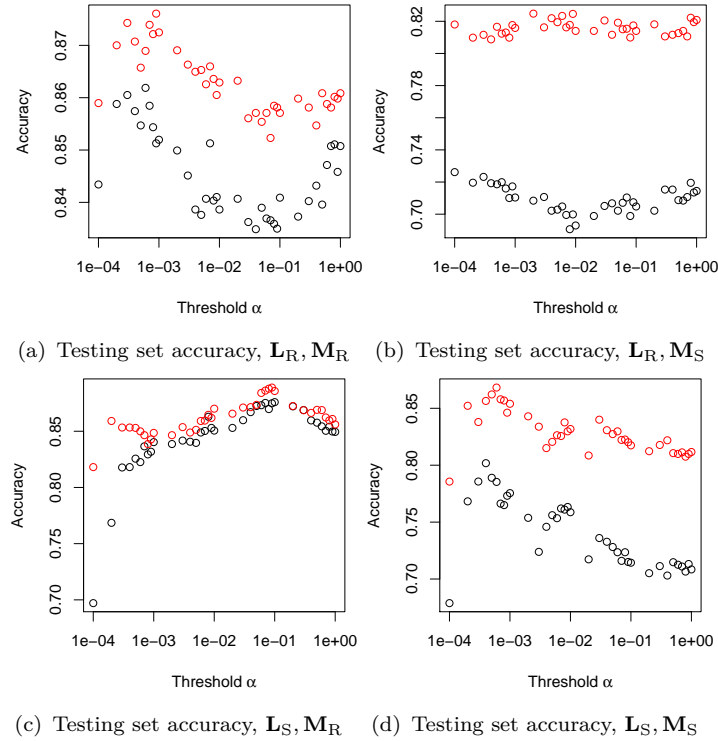


FIGURE 5.6: The accuracy of the disease classification using bagged support vector machines (SVMs) with varying thresholds in the landmark selection on a separated testing set. Black circles: shape features from the Statistical Shape Model (SSM) only; red circles: shape features with additional volume features.

both right and left hippocampus (visualization in Figure 5.12). The shape components extracted from subregions with significant shape differences indicate a better representation of the effect of the disease on the shape of the hippocampus. The mean difference between the NC and AD groups in the training set is shown in Figs. 5.14 and 5.15.

5.6 Discussion

5.6.1 Shape model and correspondences

In our current setting, the correspondence over the training set is MDL optimized, and propagated to the testing set via closest point. This is an economical solution while suboptimal to the optimization of MDL over the testing set. In practice, however, we found that the classification accuracy was not lowered when using the

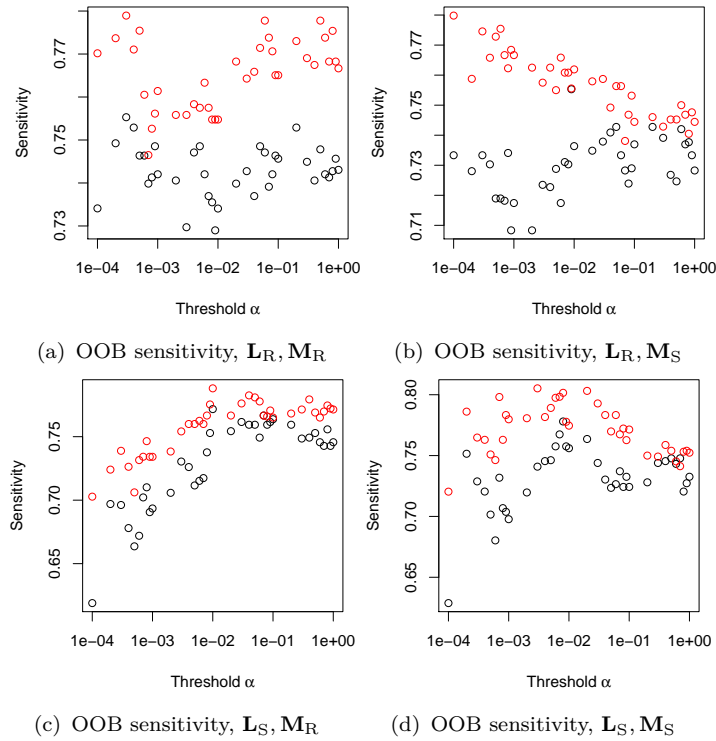


FIGURE 5.7: The out-of-bag (OOB) estimates of sensitivity of the disease classification using bagged support vector machines (SVMs) with varying thresholds in the landmark selection. Black circles: shape features from the Statistical Shape Model (SSM) only; red circles: shape features with additional volume features.

correspondences by closest point on the separate testing set as compared to the cross validation on training set equipped with MDL-optimized correspondence. Therefore we opted for the closest-point as a more practical method to process the correspondences on the testing set.

5.6.2 Identification of atrophy affected subregions

The results of the Hotelling's T^2 test superimposed on the hippocampal surface were compared to the maps showing the location of the different hippocampal subfields (La Joie et al., 2010, see Figure 5.13). Regions of significant differences between AD and NC were found mainly located in the CA1 and subiculum subfields (Figure 5.2(a)), which is consistent with previous studies (Ch etelat et al., 2008; Apostolova et al., 2010; Mueller et al., 2010). When the effect of volume change was removed in SSM by similarity alignment (Figure 5.2(b)), the regions

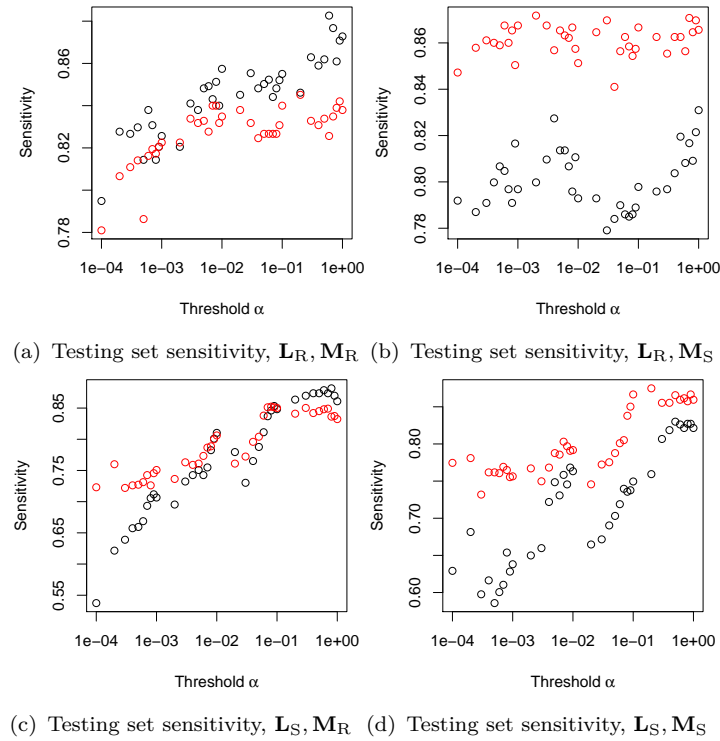


FIGURE 5.8: The sensitivity of the disease classification using bagged support vector machines (SVMs) with varying thresholds in the landmark selection on a separated testing set. Black circles: shape features from the Statistical Shape Model (SSM) only; red circles: shape features with additional volume features.

of significant shape difference between the two groups revealed a different profile with more localized effects mainly located in the posterior hippocampus. Because global changes were mainly driven by the predominant effects in the CA1 and subiculum subfields, it is not surprising that the changes independent from these main effects reveals a different pattern.

It should be pointed out that the hippocampal subregions affected by AD were identified by comparing the AD subpopulation with NC, which did not take into account the association of AD and its cognitive outcome with other factors such as age and level of education. Hippocampal atrophy has been shown to develop during the course of normal aging (Jack et al., 1998; Malykhin et al., 2008; Chételet et al., 2008; La Joie et al., 2010). The shape changes and variations reflect the combined effect of aging and AD, which may limit the discrimination ability of the shape analysis. In the future work it will be of interest to explicitly control the effects of normal aging on the hippocampus and other variables such as years

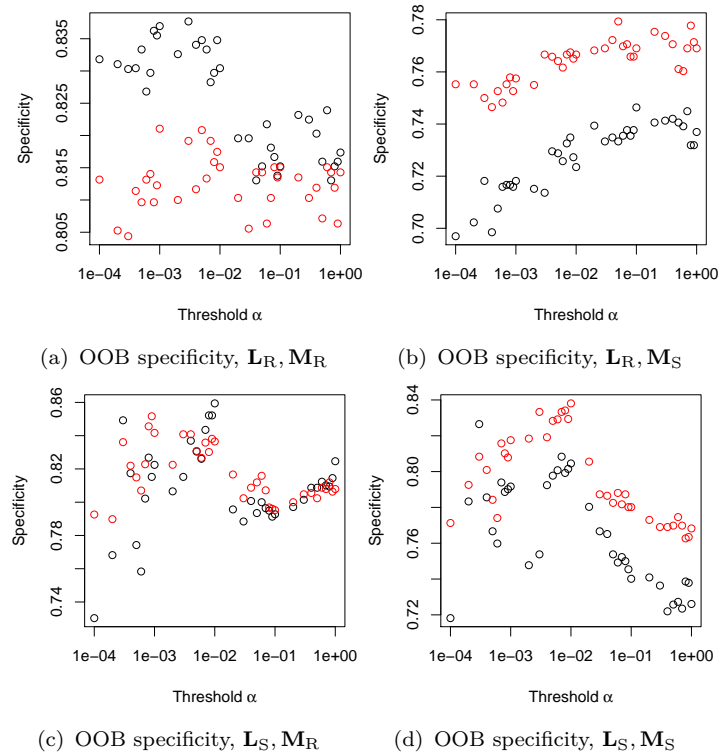


FIGURE 5.9: The out-of-bag (OOB) estimates of specificity of the disease classification using bagged support vector machines (SVMs) with varying thresholds in the landmark selection. Black circles: shape features from the Statistical Shape Model (SSM) only; red circles: shape features with additional volume features.

of education, in order to isolate the disease from these effects.

5.6.3 Disease classification using SSM

Using the SSM descriptors combining both size and shape information provided better discrimination than using only hippocampal volume to classify AD from NC. In general the descriptors of size-and-shape from \mathbf{M}_R outperformed features produced by \mathbf{M}_S , because volume alone is a good discriminant. Since the changes modeled by \mathbf{M}_S were driven by both size and shape, adding volume to the features extracted using \mathbf{M}_R and \mathbf{M}_S increased both of their accuracy, but to a much less extent for \mathbf{M}_R compared to \mathbf{M}_S . Using shape information therefore provides additional discrimination power to volumetry.

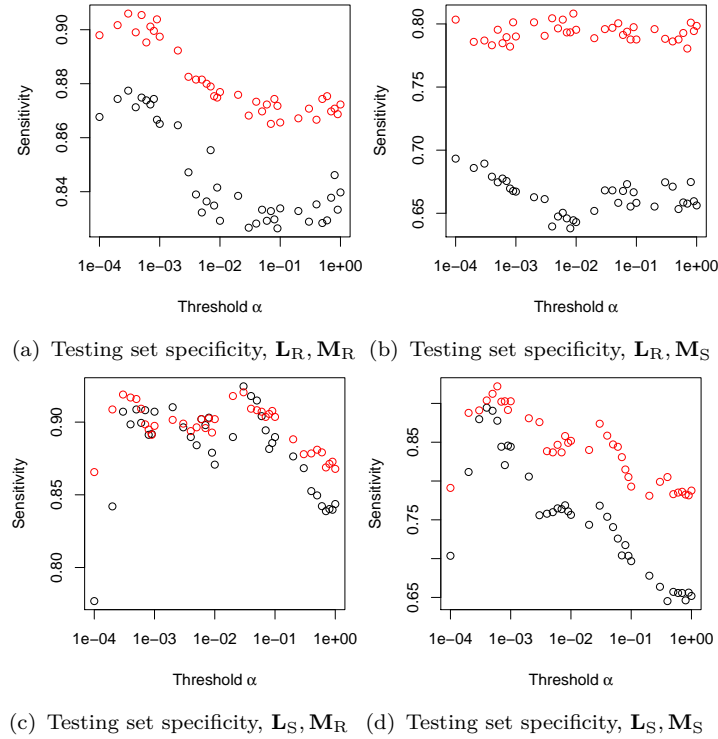


FIGURE 5.10: The specificity of the disease classification using bagged support vector machines (SVMs) with varying thresholds in the landmark selection on a separated testing set. Black circles: shape features from the Statistical Shape Model (SSM) only; red circles: shape features with additional volume features.

Restricting the analysis to the subregions affected by the disease increased the discrimination ability of the SSM approach by capturing localized differences between the subpopulations. Whole surface SSMs are able to describe the global shape or size-and-shape of the biological object, but are not sensitive to the deformations limited to specific areas on the object surface. Localizing the PCA to subregions with significant shape difference (\mathbf{L}_S) on the surface produced overall better discrimination between NC and AD than using all the points. When TIV normalized volume was added as additional features to the shape features, the best classification results were obtained using the SSM built using \mathbf{M}_R on the hippocampal subregions selected by \mathbf{L}_S .

In particular, using \mathbf{L}_S in the localization step gave more informative surface masks than \mathbf{L}_R when describing the atrophy pattern in the disease classification. Subregional masks derived from rigid-body aligned localization model \mathbf{L}_R tended to be predominantly representing changes in global scale due to the volume reduction.

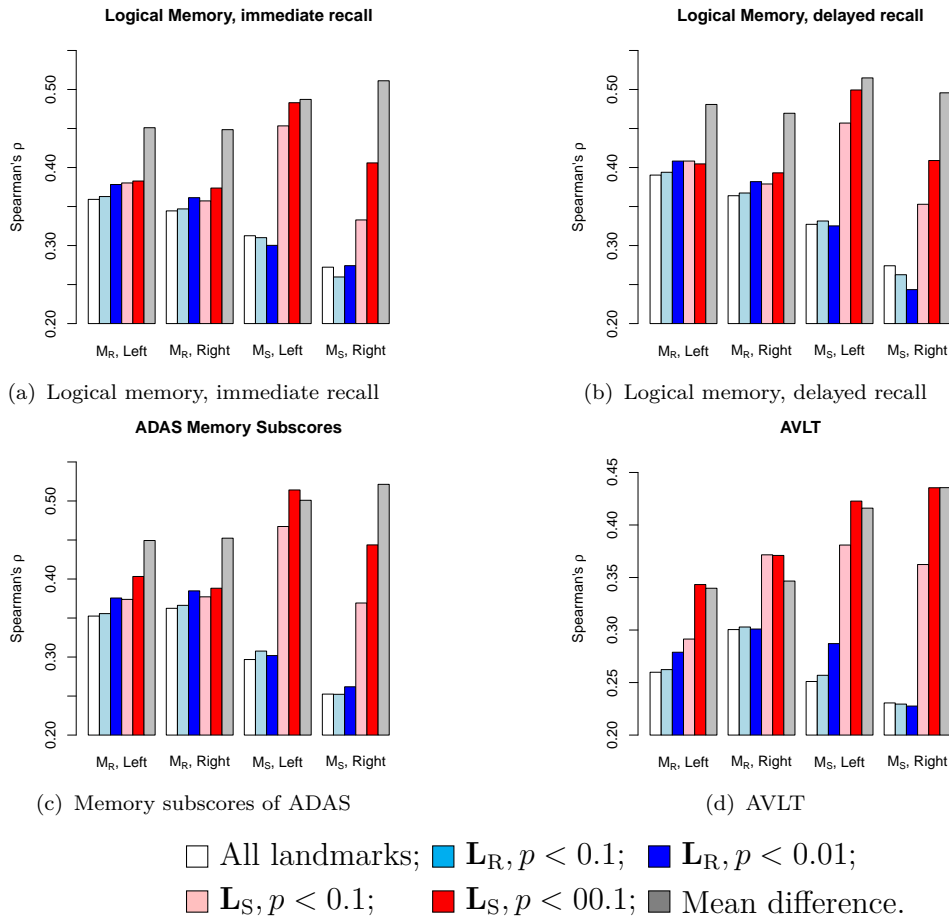


FIGURE 5.11: Bar plots of Spearman's ρ of the correlation between the memory indices and the principal components from each model. The correlation analysis is performed on the modes extracted from all landmarks, landmarks selected with thresholds at $\alpha = 0.1$, and landmarks thresholded at $\alpha = 0.01$. The component with strongest correlation with the memory score is plotted. The correlation of the shape component along the mean difference direction is also plotted.

Since the sizes of samples in L_S were normalized, the global difference in the size between subpopulations was filtered out. The resulting subregions found by L_S to be significantly different between AD and controls were more localized to subfields such as CA1 and subiculum.

The best classification performance was obtained by the models describing local size-and-shape variations ($L_S + M_R$). It is noticed that the shape changes may appear on a local scale as deformation involving both size and shape of the sub-region. The localized size-and-shape model M_R on hippocampal subregions can therefore detect the shape changes in the form of local volume change which were

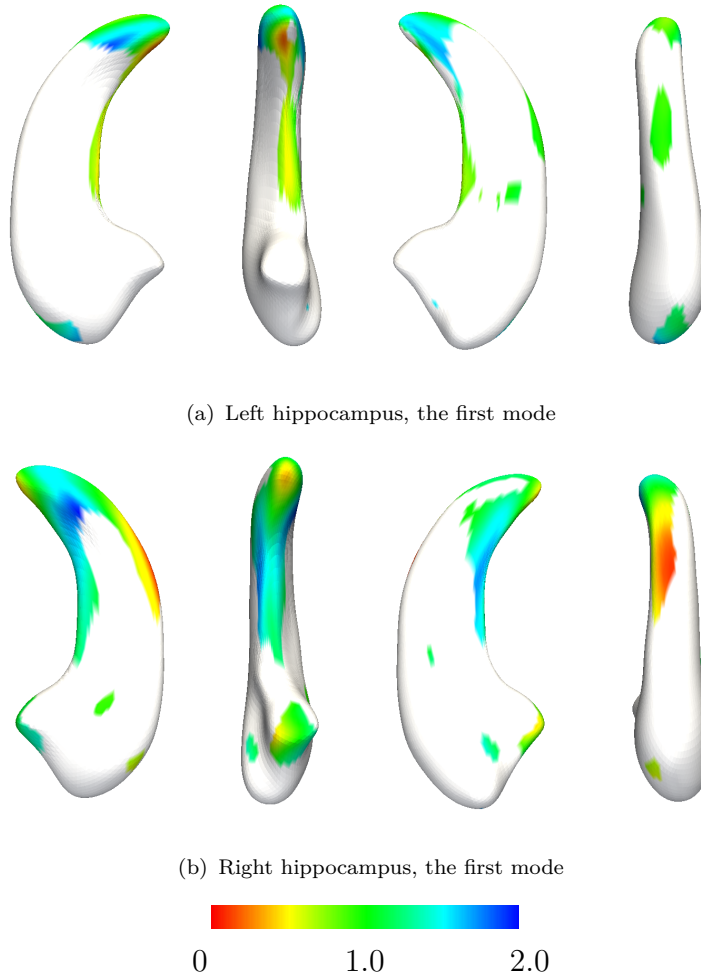


FIGURE 5.12: Variation modes captured by Principal Component Analysis (PCA) on hippocampal subregions best correlated to memory indices (logical memory, AVLT, ADAS memory), color-coded map showing the magnitude of variation described by the mode. \mathbf{L}_S , $\alpha = 0.01$, \mathbf{M}_S , mode 1. (From left to right: superior, medial, inferior, lateral)

filtered out in \mathbf{M}_S . This may explain the better performance local size-and-shape variations ($\mathbf{L}_S + \mathbf{M}_R$) than the shape models ($\mathbf{L}_S + \mathbf{M}_S$) on the local scale, in addition to the discriminant ability of the size factor present in \mathbf{M}_R .

In our experiments, the higher training error than the testing error might be due to the difference in the demographics between the training and the testing set. The average age of the AD subjects in the testing set is slightly older than in the training set, which may explain the lower testing error in the disease classification. The higher training error is also present when using only the volume as the feature for classification (77.6% OOB *vs* 83.5% on testing set).

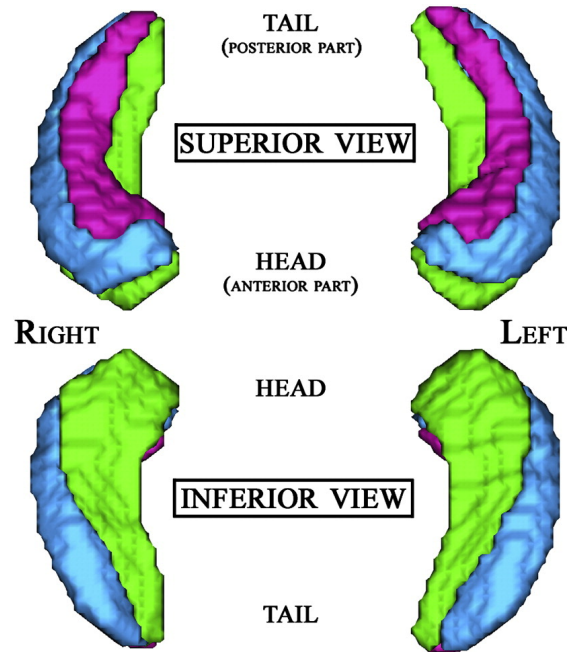


FIGURE 5.13: Three-dimensional representation of hippocampal subfields by La Joie et al. (2010): CA1 (blue), subiculum (green) and other (pink) subfields obtained by manual delineation of the three hippocampal subfields onto the DARTEL whole-brain group template, using landmarks adapted from Harding et al. (1998).

The current results demonstrate the potentiality in improving discrimination ability of SSM by localizing the model to hippocampal subregions. The optimal threshold selecting the landmarks on the training set does not give the optimal classification performance on the testing set, which calls for more targeted localization of the atrophy than simple thresholding. In addition to the statistical difference in the landmark position, histological and anatomical knowledge of hippocampus may be incorporated into the identification of regions in order capture the shape variation that is more closely linked to the AD pathology.

5.6.4 Correlation analysis

Since the accuracy of classification could possibly be the results of overfitting of the given data, the correlation analysis connects the link between shape components explaining most shape variations on the selected subregions and the memory decline in the disease, confirming that the subregional shape components displaying higher discrimination ability are related to the development of the disease.

The correlation between subregional shape components and the memory scores are comparable to the between mean difference. The variation modes extracted on the hippocampal subregions (Figure 5.12) are also consistent with the pattern along the mean difference direction in Figure 5.14.

In the correlation analysis, the \mathbf{M}_S models were able to identify the shape components with the maximum correlation higher than other shape or size-and-shape models, despite of the superiority of \mathbf{M}_R to \mathbf{M}_S in the disease classification. It is because more principal components from \mathbf{M}_R models are found to correlate with the memory decline, while to a less degree comparing to the fewer but higher correlations of \mathbf{M}_S components. Therefore using the features from \mathbf{M}_R though less correlated with the memory decline may contribute to the higher classification accuracy. The mean difference direction in the \mathbf{M}_S models are also more correlated with the memory scores than rigidly aligned models.

The correlation analysis was not designed to specify the involvement of one particular subfield in episodic memory processes, for instance in encoding and retrieval processes that are thought to preferentially engage different hippocampal subfields (Henson, 2005; Eldridge et al., 2005). Our findings however confirm the preferential implication of both CA1 and subiculum changes in episodic memory deficits in AD. The regions with variation of most significant correlation with the episodic memory index also mainly matches to the CA1 and subiculum subfields.

5.7 Summary

The shape of the hippocampus can provide valuable information for the diagnosis of AD. The principal components of the hippocampus among the population as modeled by the SSM can be used to classify AD against NC. The conventional PCA in SSM is performed on all the landmark points on the surface, which represents the original shape data in a lower dimensional subspace, but may be not discriminative between two groups. The whole-surface description of variation incorporating both hippocampal shape among the population may be not sensitive

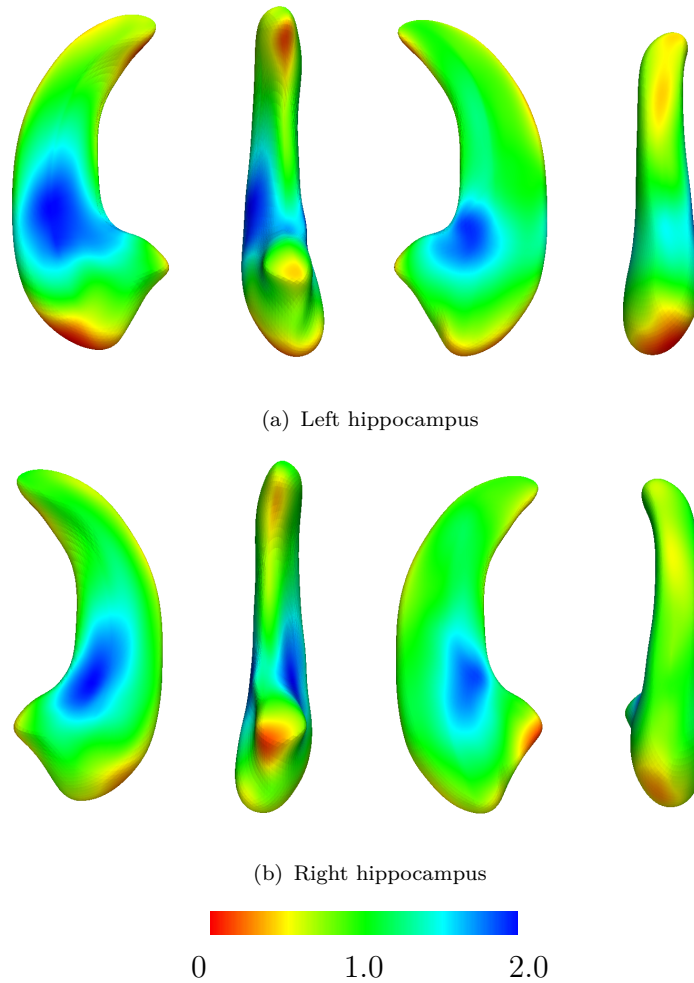


FIGURE 5.14: The variation along the direction of mean difference $\bar{X}_{\text{NC}} - \bar{X}_{\text{AD}}$ between the normal control (NC) group and the Alzheimer's disease (AD) group, color-coded map showing the magnitude of variation on the rigidly aligned model (\mathbf{M}_R). From left to right: superior, medial, inferior, lateral.

to the changes induced by the disease. By applying a statistical test on the landmark points in the SSM, we can identify the regions on the hippocampal surface which display more significant effect of the disease on the morphology and thus are more discriminative between AD and NC groups. The PCA performed on this subset produced variation modes which were used as features for the classification between these two groups. The principal variation modes on these regions were more sensitive to the shape change from NC to AD, and better correlated with the measurements of memory decline.

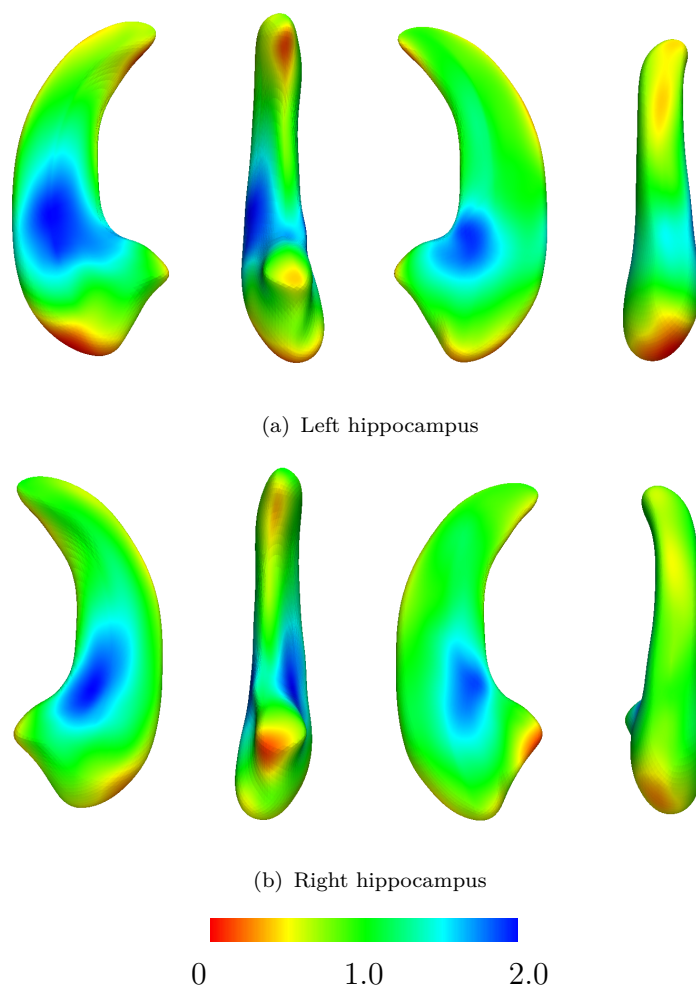


FIGURE 5.15: The variation along the direction of mean difference $\bar{X}_{\text{NC}} - \bar{X}_{\text{AD}}$ between the normal control (NC) group and the Alzheimer's disease (AD) group, color-coded map showing the magnitude of variation on the similarity aligned model (M_S). From left to right: superior, medial, inferior, lateral.

Conclusions

Topics in medical image analysis including image segmentation and shape analysis are explored in this thesis, with special applications to hippocampus in the context of Alzheimer’s disease (AD). As the conclusion of the thesis, we first summarize the contributions presented in the previous chapters, and then possible future developments based on the current state-of-the-art and the continuation of the current work are outlined.

6.1 Contributions of this thesis

The main contributions presented in this thesis lie in the segmentation and shape analysis of human hippocampi, especially those of AD patients, which is becoming of growing interest in the investigations into the neurodegenerative disease. We presented the work in the segmentation of hippocampus using multiple atlases, the construction of statistical shape models (SSMs), the establishment of correspondence across the shape data, and the detection shape changes of hippocampus in AD.

6.1.1 Multi-atlas based segmentation

We used the multi-atlas based segmentation propagation to segment the hippocampi from the brain MR images. We developed a supervised method to build a population specific atlas set by propagation from a smaller generic atlas set. The IBSR atlases of a general population were propagated to an elderly population to obtain atlas set of normal elderly subjects and AD patients. An atlas set of 40 well segmented images were built on the target elderly population using this method. A higher agreement of atlases is reached when propagating the population specific atlases to the target population than using the generic IBSR atlases.

We also investigated the issue of atlas selection in the multi-atlas based segmentation, when the locally weighted voting was used to combine the labelings of multiple atlases. In addition to the selection of atlases based on image similarity ranking, we took the redundancy into consideration of atlas selection, and introduced the diversity terms to re-rank the atlases according to the maximal marginal relevance (MMR) criterion. We also formulated the atlas selection problem as a variable selection problem in linear regression, and adopted the least angle regression (LAR) sequence for atlas selection. Alternative atlas selection strategies such as MMR and LAR provide more efficient ways for atlas selection, especially when the number of atlases to be fused in the subsequent step is limited by computational resources or out of cost-effectiveness concerns.

6.1.2 Statistical shape models

We built the SSMs of hippocampi from the shape data with correspondence by minimum description length (MDL) optimization. The optimization is carried out on the parameterization mapping of the shape surface to a shape image, which is a rectangular grid on the 2D plane, to facilitate the interpolation and reparameterization. The reparameterization of the shape surface is thus turned into the deformation of the shape image in conjunction with Dirichlet boundary condition, which is solved by a fast fluid registration algorithm.

Given the correspondence established on the hippocampal shape data in the SSM, we proposed a new method to extrapolate the SSM to unseen data, and propagate the correspondence over the SSM to the shape surface of the unseen case. An expectation-maximization iterative closest points (EM-ICP) algorithm is used to model the probabilistic correspondence between the model and the surface. The SSM parameters describing the shape surface is estimated given the expected correspondence. The symmetry between the model and the surface in the estimation is imposed by adding the consistent data term. The extension of maximum likelihood (ML) estimator to maximum *a posteriori* estimator by adding a Tikhonov regularization term is facilitated with the *a priori* shape distribution modeled by the SSM. The symmetric consistency improves the precision of the estimation in terms of a reconstruction of the shape from the model better fitting the point set data. The MAP estimator with regularization is shown to give more accurate estimation of shape parameters avoiding the effect of overfitting to the noisy data and foldings in the reconstruction.

6.1.3 Shape analysis of hippocampus in Alzheimer's disease

We used the SSM to model the shape variance of hippocampi among the elderly population consisting of both normal control subjects and patients diagnosed with AD. We used Hotelling's T^2 test on the aligned corresponding hippocampal landmarks between the normal and AD subpopulations to identify the regions affected by the atrophy due to the disease. The shape analysis was then localized to the regions exhibiting significant difference between the controls and AD, which was shown to improve the discrimination ability of the principal component analysis (PCA) based SSM. The principal components describing the localized shape variability among the population were also shown to display stronger correlation with the decline of episodic memory scores in the neurodegenerative process of AD.

6.2 Future works

In the future work, new methodologies and algorithms for brain image segmentation, shape modeling and analysis of neuroanatomical structures may be developed to extend the current work presented in this thesis.

6.2.1 Non-local approach to the atlas based image segmentation

Non-local approach has been developed to select patches of atlases similar to the target image. One advantage of this approach is its computational efficiency, since non-rigid registrations of the atlases images are no longer necessary in this approach. The label for each voxel is searched over the atlases, which provides a larger selection pool of candidate labeling. The current strategies for atlas selection and fusion may be extended to the patch selection and fusion in the non-local approach. In addition to the propagation of the anatomical labeling, demographic and diagnostic information of each atlas may also be propagated to the target image, thus localizing the effects of the pathology as well as normal physiology on a voxelwise basis.

6.2.2 Groupwise shape correspondence by optimization

The method for shape correspondence by optimization adopted and developed in this thesis applies a fluid regularization to the deformation, which is similar to the techniques widely used image registration. The current state-of-the-art in the field of image registration provides some important insight to the solution of the correspondence problem by optimization. A general algorithmic framework accommodating a wide range of registration techniques including fluid registration, elastic registration and Demons method may be implemented.

6.2.3 Shape analysis of biological objects

The localization of shape analysis shows promising results in detecting the effects of local and global changes in hippocampal shapes due to AD. The current work of hippocampal shape analysis identifies the subregions on the hippocampal surface affected by atrophy in the disease using a statistical test. More sophisticated approach incorporating anatomical labeling of hippocampal subfields given the development of higher resolution MR images may yield anatomically more meaningful results. In addition to the group information of diagnosis, other biomarkers associated to the pathological development of the disease may provide extra information in more accurate localization targeting the alternations in the hippocampal morphology linked to the disease progression.

List of publications

The following papers have been published during the preparation of this thesis:

- K. Shen, J. Fripp, F. Meriaudeau, G. Chetelat, O. Salvado, and P. Bourgeat, “Localization of hippocampal atrophy in Alzheimer’s disease,” *Alzheimer’s and Dementia*, vol. 7, no. 4, Supplement 1, pp. S17–S18, July 2011.
- A. Neubert, J. Fripp, K. Shen, C. Enstrom, R. Schwarz, L. Lauer, O. Salvado, and S. Crozier, “Automated segmentation of lumbar vertebral bodies and intervertebral discs from MRI using statistical shape models,” in *Proceedings of International Society for Magnetic Resonance in Medicine (ISMRM) Scientific Meeting*. Montréal, Canada, May 2011.
- K. Shen, P. Bourgeat, N. Dowson, F. Meriaudeau, and O. Salvado, “Atlas selection strategy using least angle regression in multi-atlas segmentation propagation,” in *2011 IEEE International Symposium on Biomedical Imaging: From Nano to Macro*. IEEE, Apr. 2011, pp. 1746–1749.
- K. Shen, P. Bourgeat, J. Fripp, F. Meriaudeau, and O. Salvado, “Detecting hippocampal shape changes in Alzheimer’s disease using statistical shape models,” in *Medical Imaging 2011: Image Processing*, vol. 7962. Lake Buena Vista, Florida, USA: SPIE, 2011, pp. 796 243–7.
- K. Shen, P. Bourgeat, F. Meriaudeau, and O. Salvado, “Atlas selection strategy in multi-atlas segmentation propagation with locally weighted voting

- using diversity-based MMR re-ranking,” in *Medical Imaging 2011: Image Processing*, vol. 7962. Lake Buena Vista, Florida, USA: SPIE, 2011, pp. 79 621B–6.
- K. Leung, K.-K. Shen, J. Barnes, G. Ridgway, M. Clarkson, J. Fripp, O. Salvado, F. Meriaudeau, N. Fox, P. Bourgeat, and S. Ourselin, “Increasing power to predict mild cognitive impairment conversion to Alzheimer’s disease using hippocampal atrophy rate and statistical shape models,” in *MICCAI 2010*, ser. LNCS, vol. 6362. Springer, 2010, pp. 125–132.
 - K. Shen, P. Bourgeat, J. Fripp, F. Meriaudeau, D. Ames, K. A. Ellis, C. L. Masters, V. L. Villemagne, C. C. Rowe, and O. Salvado, “Supervised method to build an atlas database for multi-atlas segmentation-propagation,” in *SPIE Medical Imaging 2010: Computer-Aided Diagnosis*, vol. 7624, San Diego, California, USA, 2010, pp. 76 241N–8.

The following papers have been accepted by a journal or an international conference for publication:

- K. Shen, P. Bourgeat, J. Fripp, F. Meriaudeau, and O. Salvado, “Consistent estimation of shape parameters in statistical shape model by symmetric EM algorithm,” *SPIE Medical Imaging 2012, In press*.
- K. Shen, J. Fripp, F. Meriaudeau, G. Chetelat, O. Salvado, and P. Bourgeat, “Detecting global and local hippocampal shape changes in Alzheimer’s disease using statistical shape models,” *NeuroImage*, 2012, *In press*.

The following paper to be submitted to *NeuroImage* is under preparation:

- K.-K. Shen, K. Leung, J. Barnes, G. Ridgway, M. Clarkson, J. Fripp, O. Salvado, F. Meriaudeau, N. Fox, P. Bourgeat, and S. Ourselin, “Predicting mild cognitive impairment conversion to Alzheimer’s disease using local hippocampal atrophy rate.”

Bibliography

- Abramoff, M. D., Magelhaes, P. J., and Ram, S. J. (2004). Image processing with ImageJ. *Biophotonics International*, 11(7):36–42. 2.1
- Acosta, O., Bourgeat, P., Zuluaga, M. A., Fripp, J., Salvado, O., and Ourselin, S. (2009). Automated voxel-based 3D cortical thickness measurement in a combined Lagrangian-Eulerian PDE approach using partial volume maps. *Medical Image Analysis*, 13(5):730–743. 5.3
- Alcantara, D., Carmichael, O., Delson, E., Harcourt-Smith, W., Sterner, K., Frost, S., Dutton, R., Thompson, P., Aizenstein, H., Lopez, O., Becker, J., and Amenta, N. (2007). Localized components analysis. In *Proceedings of the 20th international conference on Information processing in medical imaging*, pages 519–531, Kerkrade, The Netherlands. Springer-Verlag. 2.3.2
- Aljabar, P., Heckemann, R., Hammers, A., Hajnal, J., and Rueckert, D. (2009). Multi-atlas based segmentation of brain images: Atlas selection and its effect on accuracy. *NeuroImage*, 46(3):726–738. 2.1.2.3, 3.1.2, 3.2, 3.2.1
- Aljabar, P., Heckemann, R., Hammers, A., Hajnal, J. V., and Rueckert, D. (2007). Classifier selection strategies for label fusion using large atlas databases. In Ayache, N., Ourselin, S., and Maeder, A., editors, *Medical Image Computing and Computer-Assisted Intervention – MICCAI 2007*, volume 4791 of *LNCS*, pages 523–531, Berlin, Heidelberg. Springer. 2.1.2.3, 3.1.2, 3.2, 3.2.1

- Alzheimer, A. (1911). Über eigenartige Krankheitsfälle des späteren Alters. *Zeitschrift für die gesamte Neurologie und Psychiatrie*, 4(1):356–385. 1.1.1
- Alzheimer's Association (2011). 2011 Alzheimer's disease facts and figures. *Alzheimer's and Dementia*, 7(2):208–244. 1.1.1
- American Psychiatric Association (1994). *Diagnostic and Statistical Manual of Mental Disorders (DSM-IV)*. American Psychiatric Publishing, Inc. 1.1.1
- American Psychiatric Association and Task Force on DSM-IV (2000). *Diagnostic and statistical manual of mental disorders: DSM-IV-TR*. American Psychiatric Pub. 1.1.1
- Andersen, P., Bliss, T., and Skrede, K. (1971). Lamellar organization of hippocampal excitatory pathways. *Experimental Brain Research*, 13(2). 1.1.2
- Andersen, P., Morris, R., Amaral, D., Bliss, T., and O'Keefe, J. (2006). *The Hippocampus Book*. Oxford University Press, USA, 1 edition. 1.1.2
- Apostolova, L. G., Dinov, I. D., Dutton, R. A., Hayashi, K. M., Toga, A. W., Cummings, J. L., and Thompson, P. M. (2006). 3D comparison of hippocampal atrophy in amnesic mild cognitive impairment and Alzheimer's disease. *Brain*, 129(11):2867–2873. 2.3.2
- Apostolova, L. G., Thompson, P. M., Green, A. E., Hwang, K. S., Zoumalan, C., Jack, C. R., Harvey, D. J., Petersen, R. C., Thal, L. J., Aisen, P. S., Toga, A. W., Cummings, J. L., and DeCarli, C. S. (2010). 3D comparison of low, intermediate, and advanced hippocampal atrophy in MCI. *Human Brain Mapping*, 31(5):786–797. 5.6.2
- Artaechevarria, X., Munoz-Barrutia, A., and Ortiz-de-Solorzano, C. (2009). Combination strategies in Multi-Atlas image segmentation: Application to brain MR data. *Medical Imaging, IEEE Transactions on*, 28(8):1266–1277. 2.1.2.3, 3.1.3
- Ashburner, J. (2007). A fast diffeomorphic image registration algorithm. *NeuroImage*, 38(1):95–113. 2.1.2.3, 3.1.1.2

- Ashburner, J. and Friston, K. (2003). Morphometry. In Frackowiak, R., Friston, K., Frith, C., Dolan, R., Friston, K., Price, C., Zeki, S., Ashburner, J., and Penny, W., editors, *Human Brain Function*. Academic Press, 2nd edition. 2.3.1
- Ashburner, J. and Friston, K. J. (1999). Nonlinear spatial normalization using basis functions. *Human Brain Mapping*, 7(4):254–266. 2.1.2.3, 3.1.1.2
- Ashburner, J. and Friston, K. J. (2000). Voxel-based morphometry –the methods. *NeuroImage*, 11(6):805–821. 2.3.1
- Ashburner, J. and Friston, K. J. (2005). Unified segmentation. *NeuroImage*, 26(3):839–851. 2.1.2.3, 3.1.1.2
- Ashton, E. A., Parker, K. J., Berg, M. J., and Chen, C. W. (1997). A novel volumetric feature extraction technique with applications to MR images. *IEEE Transactions on Medical Imaging*, 16(4):365–371. 2.1.2.1
- Babalola, K. O., Patenaude, B., Aljabar, P., Schnabel, J., Kennedy, D., Crum, W., Smith, S., Cootes, T., Jenkinson, M., and Rueckert, D. (2009). An evaluation of four automatic methods of segmenting the subcortical structures in the brain. *NeuroImage*, 47(4):1435–1447. 2.1.2.2
- Babalola, K. O., Patenaude, B., Aljabar, P., Schnabel, J., Kennedy, D., Crum, W., Smith, S., Cootes, T. F., Jenkinson, M., and Rueckert, D. (2008). Comparison and evaluation of segmentation techniques for subcortical structures in brain MRI. In Metaxas, D., Axel, L., Fichtinger, G., and Székely, G., editors, *Medical Image Computing and Computer-Assisted Intervention – MICCAI 2008*, volume 5241 of *LNCS*, pages 409–416, Berlin, Heidelberg. Springer. 2.1.2.2, 2.1.2.3
- Babalola, K. O., Petrovic, V., Cootes, T. F., Taylor, C. J., Twining, C. J., and Mills, A. (2007). Automatic segmentation of the caudate nuclei using active appearance models. In *Proceedings of the workshop on 3D Segmentation in the clinic: a grand challenge at the 10th International Conference on Medical Image Computing and Computer-Assisted Intervention*, pages 57–64. 2.1.2.2

- Baillard, C., Hellier, P., and Barillot, C. (2001). Segmentation of brain 3D MR images using level sets and dense registration. *Medical Image Analysis*, 5(3):185–194. 2.1.2.3
- Ballard, C., Gauthier, S., Corbett, A., Brayne, C., Aarsland, D., and Jones, E. (2011). Alzheimer’s disease. *The Lancet*, 377(9770):1019–1031. 1.1.1
- Barkhof, F., Fox, N. C., Bastos-Leite, A. J., and Scheltens, P. (2011). *Neuroimaging in Dementia*. Springer Berlin Heidelberg, Berlin, Heidelberg. 1.1.3, 1.6, 2.5
- Barnes, J., Bartlett, J. W., van de Pol, L. A., Loy, C. T., Scahill, R. I., Frost, C., Thompson, P., and Fox, N. C. (2009a). A meta-analysis of hippocampal atrophy rates in Alzheimer’s disease. *Neurobiology of Aging*, 30(11):1711–1723. 1.1.3.2, 2.3.1
- Barnes, J., Boyes, R. G., Lewis, E. B., Schott, J. M., Frost, C., Scahill, R. I., and Fox, N. C. (2007). Automatic calculation of hippocampal atrophy rates using a hippocampal template and the boundary shift integral. *Neurobiology of Aging*, 28(11):1657–1663. 2.3.1
- Barnes, J., Ourselin, S., and Fox, N. C. (2009b). Clinical application of measurement of hippocampal atrophy in degenerative dementias. *Hippocampus*, 19(6):510–516. 2.3.1
- Barnes, J., Scahill, R. I., Boyes, R. G., Frost, C., Lewis, E. B., Rossor, C. L., Rossor, M. N., and Fox, N. C. (2004). Differentiating AD from aging using semiautomated measurement of hippocampal atrophy rates. *NeuroImage*, 23(2):574–581. 2.3.1
- Baron, J. C., Chételat, G., Desgranges, B., Perchey, G., Landeau, B., de la Sayette, V., and Eustache, F. (2001). In vivo mapping of gray matter loss with Voxel-Based morphometry in mild alzheimer’s disease. *NeuroImage*, 14(2):298–309. 2.3.1

- Barron, J. L., Fleet, D. J., and Beauchemin, S. S. (1994). Performance of optical flow techniques. *International Journal of Computer Vision*, 12(1):43–77. 3.1.1.2
- Beg, M. F., Miller, M. I., Trouvé, A., and Younes, L. (2005). Computing large deformation metric mappings via geodesic flows of diffeomorphisms. *International Journal of Computer Vision*, 61(2):139–157. 2.1.2.3, 3.1.1.2
- Bertram, L., McQueen, M. B., Mullin, K., Blacker, D., and Tanzi, R. E. (2007). Systematic meta-analyses of Alzheimer disease genetic association studies: the AlzGene database. *Nature Genetics*, 39(1):17–23. 1.1.1
- Besag, J. (1993). Towards bayesian image analysis. *Journal of Applied Statistics*, 20(5):107–119. 2.1.2.1
- Besl, P. J. and McKay, H. D. (1992). A method for registration of 3-D shapes. *IEEE Transactions on Pattern Analysis and Machine Intelligence*, 14(2):239–256. 2.2.2
- Bishop, C. A., Jenkinson, M., Andersson, J., Declerck, J., and Merhof, D. (2011). Novel fast marching for automated segmentation of the hippocampus (FMASH): method and validation on clinical data. *NeuroImage*, 55(3):1009–1019. 2.1.2.1
- Blennow, K., de Leon, M. J., and Zetterberg, H. (2006). Alzheimer’s disease. *The Lancet*, 368(9533):387–403. 1.1.1
- Blessed, G., Tomlinson, B. E., and Roth, M. (1968). The association between quantitative measures of dementia and of senile change in the cerebral grey matter of elderly subjects. *The British Journal of Psychiatry*, 114(512):797–811. 1.1.1
- Bobinski, M., de Leon, M. J., Tarnawski, M., Wegiel, J., Bobinski, M., Reisberg, B., Miller, D. C., and Wisniewski, H. M. (1998). Neuronal and volume loss in CA1 of the hippocampal formation uniquely predicts duration and severity of Alzheimer disease. *Brain Research*, 805(1-2):267–269. 2.3.2
- Bobinski, M., de Leon, M. J., Wegiel, J., DeSanti, S., Convit, A., Saint Louis, L. A., Rusinek, H., and Wisniewski, H. M. (1999). The histological validation

- of post mortem magnetic resonance imaging-determined hippocampal volume in Alzheimer's disease. *Neuroscience*, 95(3):721–725. 1.1.3.2
- Bookstein, F. (1991). *Morphometric tools for landmark data : geometry and biology*. Cambridge University Press, Cambridge, New York. 2.2
- Bookstein, F. L. (1978a). Linear machinery for morphological distortion. *Computers and Biomedical Research*, 11(5):435–458. 2.2
- Bookstein, F. L. (1978b). *The measurement of biological shape and shape change*. Springer-Verlag, Berlin, New York. 2.2
- Bookstein, F. L. (1986). Size and shape spaces for landmark data in two dimensions. *Statistical Science*, 1(2):181–222. 2.2
- Bookstein, F. L. (1996). Biometrics, biomathematics and the morphometric synthesis. *Bulletin of Mathematical Biology*, 58(2):313–365. 4
- Bouix, S., Pruessner, J. C., Collins, D. L., and Siddiqi, K. (2005). Hippocampal shape analysis using medial surfaces. *NeuroImage*, 25(4):1077–1089. 2.3.2
- Braak, H. and Braak, E. (1991). Neuropathological staging of Alzheimer-related changes. *Acta Neuropathologica*, 82(4):239–259. 1.1.2
- Brechtbühler, C., Gerig, G., and Kübler, O. (1995). Parametrization of closed surfaces for 3-D shape description. *Computer Vision and Image Understanding*, 61(2):154–170. 2.2.1, 2.2.3, 4.1.1, 5, 6, 4.2
- Breiman, L. (1996a). Bagging predictors. *Machine Learning*, 24(2):123–140. 5.3
- Breiman, L. (1996b). Out-of-bag estimation. Technical report, Statistics Department, University of California. 5.3
- Brett, A. D. and Taylor, C. J. (2000). A method of automated landmark generation for automated 3D PDM construction. *Image and Vision Computing*, 18(9):739–748. 2.2.3

- Bro-Nielsen, M. and Gramkow, C. (1996). Fast fluid registration of medical images. In Höhne, K. H. and Kikinis, R., editors, *Visualization in Biomedical Computing*, volume 1131, pages 265–276, Berlin/Heidelberg. Springer-Verlag. 4.1.3.3
- Busatto, G. F., Diniz, B. S., and Zanetti, M. V. (2008). Voxel-based morphometry in alzheimer’s disease. *Expert Review of Neurotherapeutics*, 8(11):1691–1702. 2.3.1
- Cahill, N. D., Noble, J. A., Hawkes, D. J., and Ray, L. A. (2007). Fast fluid registration with Dirichlet boundary conditions: A transform-based approach. In *4th IEEE International Symposium on Biomedical Imaging: From Nano to Macro, 2007. ISBI 2007*, pages 712–715. IEEE. 4.1.3.3, 8, 5
- Carbonell, J. and Goldstein, J. (1998). The use of MMR, diversity-based reranking for reordering documents and producing summaries. In *Proceedings of the 21st annual international ACM SIGIR conference on Research and development in information retrieval*, pages 335–336, Melbourne, Australia. ACM. 3.3.1
- Cardoso, J. (1999). High-order contrasts for independent component analysis. *Neural Computation*, 11(1):157–192. 2.2.4
- Carmichael, O. T., Aizenstein, H. A., Davis, S. W., Becker, J. T., Thompson, P. M., Meltzer, C. C., and Liu, Y. (2005). Atlas-based hippocampus segmentation in Alzheimer’s disease and mild cognitive impairment. *NeuroImage*, 27(4):979–990. 2.1.2.3
- Chen, M. (1999). *3-D Deformable Registration Using a Statistical Atlas with Applications in Medicine*. PhD thesis, Robotics Institute, Carnegie Mellon University, Pittsburgh, PA. 2.1.2.3
- Chen, Y. and Medioni, G. (1992). Object modelling by registration of multiple range images. *Image and Vision Computing*, 10(3):145–155. 2.2.2
- Chételat, G., Fouquet, M., Kalpouzos, G., Denghien, I., la Sayette, V. D., Viader, F., Mézenge, F., Landeau, B., Baron, J., Eustache, F., and Desgranges,

- B. (2008). Three-dimensional surface mapping of hippocampal atrophy progression from MCI to AD and over normal aging as assessed using voxel-based morphometry. *Neuropsychologia*, 46(6):1721–1731. 2.3.2, 5.6.2, 5.6.2
- Christensen, G. E. and Johnson, H. J. (2001). Consistent image registration. *IEEE Transactions on Medical Imaging*, 20(7):568–582. 2.1.2.3
- Christensen, G. E., Joshi, S. C., and Miller, M. I. (1997). Volumetric transformation of brain anatomy. *Medical Imaging, IEEE Transactions on*, 16(6):864–877. 3.4.2.1
- Christensen, G. E., Rabbitt, R. D., and Miller, M. I. (1996). Deformable templates using large deformation kinematics. *IEEE Transactions on Image Processing*, 5(10):1435–1447. 4.1.3.3, 4.1.3.4
- Chui, H. and Rangarajan, A. (2000). A feature registration framework using mixture models. In *Mathematical Methods in Biomedical Image Analysis, IEEE Workshop on*, volume 0, pages 190–197, Los Alamitos, CA, USA. IEEE Computer Society. 4.2
- Chupin, M., Gérardin, E., Cuingnet, R., Boutet, C., Lemieux, L., Lehericy, S., Benali, H., Garnero, L., and Colliot, O. (2009). Fully automatic hippocampus segmentation and classification in Alzheimer’s disease and mild cognitive impairment applied on data from ADNI. *Hippocampus*, 19(6):579–587. 2.1.2.1, 2.3.1
- Chupin, M., Mukuna-Bantumbakulu, A. R., Hasboun, D., Bardinet, E., Baillet, S., Kinkingnéhun, S., Lemieux, L., Dubois, B., and Garnero, L. (2007). Anatomically constrained region deformation for the automated segmentation of the hippocampus and the amygdala: Method and validation on controls and patients with Alzheimer’s disease. *NeuroImage*, 34(3):996–1019. 2.1.2.1
- Collignon, A., Maes, F., Delaere, D., Vandermeulen, D., Suetens, P., and Marchal, G. (1995). Automated multi-modality image registration based on information theory. In *Information Processing in Medical Imaging – IPMI ’95*, pages 263–274. 3.1.2

- Collins, D. L. (1994). *3D Model-based segmentation of individual brain structures from magnetic resonance imaging data*. PhD thesis, McGill University, Montreal. 2.1.1
- Collins, D. L. and Evans, A. C. (1997). ANIMAL: Validation and applications of nonlinear registration-based segmentation. *International Journal of Pattern Recognition and Artificial Intelligence*, 11:1271–1294. 2.1.2.3
- Collins, D. L., Holmes, C. J., Peters, T. M., and Evans, A. C. (1995). Automatic 3-D model-based neuroanatomical segmentation. *Human Brain Mapping*, 3(3):190–208. 2.1.2.3
- Collins, D. L. and Pruessner, J. C. (2010). Towards accurate, automatic segmentation of the hippocampus and amygdala from MRI by augmenting ANIMAL with a template library and label fusion. *NeuroImage*, 52(4):1355–1366. 2.1.2.3
- Combès, B. and Prima, S. (2010). An efficient EM-ICP algorithm for symmetric consistent non-linear registration of point sets. In Jiang, T., Navab, N., Plum, J. P. W., and Viergever, M. A., editors, *Medical Image Computing and Computer-Assisted Intervention – MICCAI 2010*, volume 6362 of *LNCS*, pages 594–601, Berlin, Heidelberg. Springer Berlin Heidelberg. 4.2
- Commowick, O., Warfield, S. K., and Malandain, G. (2009). Using Frankenstein’s creature paradigm to build a patient specific atlas. In Yang, G., Hawkes, D., Rueckert, D., Noble, A., and Taylor, C., editors, *Medical Image Computing and Computer-Assisted Intervention – MICCAI 2009*, volume 5762 of *LNCS*, pages 993–1000, Berlin, Heidelberg. Springer Berlin Heidelberg. 2.1.2.3
- Cootes, T., Taylor, C., Cooper, D., and Graham, J. (1992). Training models of shape from sets of examples. In *Proceedings of British Machine Vision Conference*, pages 9–18. 2.2.1, 2.2.4
- Cootes, T. F., Edwards, G. J., and Taylor, C. J. (2001). Active appearance models. *IEEE Transactions on Pattern Analysis and Machine Intelligence*, 23(6):681–685. 2.1.2.2

- Cootes, T. F., Taylor, C. J., Cooper, D. H., and Graham, J. (1995). Active shape Models-Their training and application. *Computer Vision and Image Understanding*, 61(1):38–59. 2.1.2.2
- Coupé, P., Manjón, J. V., Fonov, V., Pruessner, J., Robles, M., and Collins, D. L. (2010). Nonlocal Patch-Based label fusion for hippocampus segmentation. In Jiang, T., Navab, N., Pluim, J. P. W., and Viergever, M. A., editors, *Medical Image Computing and Computer-Assisted Intervention – MICCAI 2010*, volume 6363 of *LNCIS*, pages 129–136, Berlin, Heidelberg. Springer Berlin Heidelberg. 2.1.2.3
- Cox, R. W. (1996). AFNI: software for analysis and visualization of functional magnetic resonance neuroimages. *Computers and Biomedical Research*, 29(3):162–173. 2.1.2.3, 3.1.1.2
- Crum, W., Griffin, L., Hill, D., and Hawkes, D. (2003). Zen and the art of medical image registration: correspondence, homology, and quality. *NeuroImage*, 20(3):1425–1437. 2.1.2.3
- Crum, W. R., Scahill, R. I., and Fox, N. C. (2001). Automated hippocampal segmentation by regional fluid registration of serial MRI: validation and application in Alzheimer’s disease. *NeuroImage*, 13(5):847–855. 2.1.2.3
- Csernansky, J. G., Wang, L., Joshi, S., Miller, J. P., Gado, M., Kido, D., McKeel, D., Morris, J. C., and Miller, M. I. (2000). Early DAT is distinguished from aging by high-dimensional mapping of the hippocampus. *Neurology*, 55(11):1636–1643. 2.3.2
- Csernansky, J. G., Wang, L., Swank, J., Miller, J. P., Gado, M., McKeel, D., Miller, M. I., and Morris, J. C. (2005). Preclinical detection of Alzheimer’s disease: hippocampal shape and volume predict dementia onset in the elderly. *NeuroImage*, 25(3):783–792. 2.3.2
- Cuingnet, R., Gerardin, E., Tessieras, J., Auzias, G., Lehericy, S., Habert, M., Chupin, M., Benali, H., and Colliot, O. (2010). Automatic classification of

- patients with Alzheimer's disease from structural MRI: a comparison of ten methods using the ADNI database. *NeuroImage*, In Press, Corrected Proof. 2.3.2, 5.3, 5.5.3
- Dahlberg, B. E. J., Kenig, C. E., and Verchota, G. C. (1988). Boundary value problems for the systems of elastostatics in Lipschitz domains. *Duke Mathematical Journal*, 57(3):795–818. 4.1.3.3
- Dale, A. M., Fischl, B., and Sereno, M. I. (1999). Cortical Surface-Based analysis: I. segmentation and surface reconstruction. *NeuroImage*, 9(2):179–194. 2.1.2.2
- Davatzikos, C., Tao, X., and Shen, D. (2003). Hierarchical active shape models, using the wavelet transform. *IEEE Transactions on Medical Imaging*, 22(3):414–423. 2.2.1
- Davies, R., Twining, C., Cootes, T., Waterton, J., and Taylor, C. (2002). A minimum description length approach to statistical shape modeling. *Medical Imaging, IEEE Transactions on*, 21(5):525–537. 2.2.3, 4.1.3.2
- Davies, R., Twining, C., and Taylor, C. (2008a). *Statistical Models of Shape: Optimisation and Evaluation*. Springer, 1st edition. 2.2.3, 4.6
- Davies, R. H. (2002). *Learning shape: optimal models for analysing natural variability*. PhD thesis, Univeristy of Manchester. 2.3.2
- Davies, R. H., Twining, C. J., Allen, P. D., Cootes, T. F., and Taylor, C. J. (2003). Shape discrimination in the hippocampus using an MDL model. In Taylor, C. and Noble, J. A., editors, *Information Processing in Medical Imaging*, volume 2732 of *LNCS*, pages 38–50, Berlin, Heidelberg. Springer Berlin Heidelberg. 2.2.3, 2.3.2, 4.1.3.2, 4.1.4
- Davies, R. H., Twining, C. J., and Taylor, C. (2008b). Groupwise surface correspondence by optimization: Representation and regularization. *Medical Image Analysis*, 12(6):787–796. 2.2.3, 4.1.3, 4.5, 4.1.3.3, 4.1.3.3, 9, 5.2
- Dawant, B. M., Hartmann, S. L., Thirion, J. P., Maes, F., Vandermeulen, D., and Demaerel, P. (1999). Automatic 3-D segmentation of internal structures of the

- head in MR images using a combination of similarity and free-form transformations. i. methodology and validation on normal subjects. *IEEE Transactions on Medical Imaging*, 18(10):909–916. 2.1.2.3
- DeCarli, C., Frisoni, G. B., Clark, C. M., Harvey, D., Grundman, M., Petersen, R. C., Thal, L. J., Jin, S., Jack, C. R., Scheltens, P., and the Alzheimer’s Disease Cooperative Study Group (2007). Qualitative estimates of medial temporal atrophy as a predictor of progression from mild cognitive impairment to dementia. *Arch Neurol*, 64(1):108–115. 1.1.3.2
- Deschamps, T. and Cohen, L. D. (2000). Minimal paths in 3D images and application to virtual endoscopy. In Vernon, D., editor, *Computer Vision — ECCV 2000*, volume 1843 of *LNCS*, pages 543–557, Berlin, Heidelberg. Springer Berlin Heidelberg. 2.1.2.1
- di Sclafani, V., Truran, D. L., Bloomer, C., Tolou-shams, M., Clark, H. W., Norman, D., Hannauer, D., and Fein, G. (1998). Abstinent chronic crack-cocaine and crackcocaine/alcohol abusers evidence normal hippocampal volumes on MRI despite persistent cognitive impairments. *Addiction Biology*, 3(3):261–270. 2.1.1
- Dice, L. R. (1945). Measures of the amount of ecologic association between species. *Ecology*, 26(3):297–302. 2.1.3
- Dryden, I. L. and Mardia, K. V. (1998). *Statistical Shape Analysis*. Wiley. 2.4, 2.2, 2.2
- Du, A. T., Schuff, N., Amend, D., Laakso, M. P., Hsu, Y. Y., Jagust, W. J., Yaffe, K., Kramer, J. H., Reed, B., Norman, D., Chui, H. C., and Weiner, M. W. (2001). Magnetic resonance imaging of the entorhinal cortex and hippocampus in mild cognitive impairment and Alzheimer’s disease. *Journal of Neurology, Neurosurgery, and Psychiatry*, 71(4):441–447. 2.1.1
- Duara, R., Loewenstein, D. A., Potter, E., Appel, J., Greig, M. T., Urs, R., Shen, Q., Raj, A., Small, B., Barker, W., Schofield, E., Wu, Y., and Potter, H. (2008).

- Medial temporal lobe atrophy on MRI scans and the diagnosis of Alzheimer disease. *Neurology*, 71(24):1986–1992. 1.1.3.2
- Dubois, B., Feldman, H. H., Jacova, C., Dekosky, S. T., Barberger-Gateau, P., Cummings, J., Delacourte, A., Galasko, D., Gauthier, S., Jicha, G., Meguro, K., O'brien, J., Pasquier, F., Robert, P., Rossor, M., Salloway, S., Stern, Y., Visser, P. J., and Scheltens, P. (2007). Research criteria for the diagnosis of Alzheimer's disease: revising the NINCDS-ADRDA criteria. *Lancet Neurology*, 6(8):734–746. 1.1.1
- Duchesne, S., Pruessner, J., and Collins, D. (2002). Appearance-based segmentation of medial temporal lobe structures. *NeuroImage*, 17(2):515–531. 2.1.2.3
- Duvernoy, H. M. (2005). *The Human Hippocampus: Functional Anatomy, Vascularization and Serial Sections with MRI*. Springer, 3rd edition. 1.1.2, 1.4
- Ebmeier, K. P., Donaghey, C., and Dougall, N. J. (2005). Neuroimaging in dementia. *Neuroimaging, Part B*, Volume 67:43–72. 1.1.3
- Efron, B., Hastie, T., Johnstone, I., and Tibshirani, R. (2004). Least angle regression. *The Annals of Statistics*, 32(2):407–451. 3.3, 3.3, 4, 3.3.2
- Eldridge, L. L., Engel, S. A., Zeineh, M. M., Bookheimer, S. Y., and Knowlton, B. J. (2005). A dissociation of encoding and retrieval processes in the human hippocampus. *The Journal of Neuroscience*, 25(13):3280–3286. 5.6.4
- Ellis, K. A., Rowe, C. C., Villemagne, V. L., Martins, R. N., Masters, C. L., Salvado, O., Szoek, C., and Ames, D. (2010). Addressing population aging and Alzheimer's disease through the Australian Imaging Biomarkers and Lifestyle study: Collaboration with the Alzheimer's Disease Neuroimaging Initiative. *Alzheimer's and Dementia*, 6(3):291–296. 3.4.1.1
- Ericsson, A. and Åström, K. (2003). Minimizing the description length using steepest descent. In *Proceedings of British Machine Vision Conference*, volume 2, pages 93–102, Norwich, UK. 2.2.3, 4.1.3.2

- Evans, A. C., Collins, D. L., Mills, S. R., Brown, E. D., Kelly, R. L., and Peters, T. M. (1993). 3D statistical neuroanatomical models from 305 MRI volumes. In *Nuclear Science Symposium and Medical Imaging Conference, 1993., 1993 IEEE Conference Record.*, pages 1813–1817 vol.3. IEEE. 2.1.1
- Ferrarini, L., Olofsen, H., Palm, W. M., Buchem, M. A. v., Reiber, J. H. C., and Admiraal-Behloul, F. (2007). GAMEs: growing and adaptive meshes for fully automatic shape modeling and analysis. *Medical Image Analysis*, 11(3):302–314. 2.2.3
- Fischl, B., Salat, D. H., Busa, E., Albert, M., Dieterich, M., Haselgrove, C., van der Kouwe, A., Killiany, R., Kennedy, D., Klaveness, S., Montillo, A., Makris, N., Rosen, B., and Dale, A. M. (2002). Whole brain segmentation: Automated labeling of neuroanatomical structures in the human brain. *Neuron*, 33(3):341–355. 2.1.2.2, 2.1.2.3
- Fischl, B., Salat, D. H., van der Kouwe, A. J., Makris, N., Ségonne, F., Quinn, B. T., and Dale, A. M. (2004). Sequence-independent segmentation of magnetic resonance images. *NeuroImage*, 23(Supplement 1):S69–S84. 2.1.2.2
- Fischl, B., Sereno, M. I., and Dale, A. M. (1999). Cortical Surface-Based analysis: II: inflation, flattening, and a Surface-Based coordinate system. *NeuroImage*, 9(2):195–207. 2.1.2.2
- Fitzgibbon, A. W. (2003). Robust registration of 2D and 3D point sets. *Image and Vision Computing*, 21(13-14):1145–1153. 2.2.2
- Fleute, M. and Lavallée, S. (1998). Building a complete surface model from sparse data using statistical shape models: Application to computer assisted knee surgery. In Wells, W. M., Colchester, A., and Delp, S., editors, *Medical Image Computing and Computer-Assisted Intervention — MICCAI’98*, volume 1496 of *LNCS*, pages 879–887, Berlin/Heidelberg. Springer-Verlag. 2.2.3
- Fox, N., Scahill, R., Crum, W., and Rossor, M. (1999). Correlation between rates of brain atrophy and cognitive decline in AD. *Neurology*, 52(8):1687. 1.1.3.2

- Frangi, A. F., Niessen, W. J., Rueckert, D., and Schnabel, J. A. (2001). Automatic 3D ASM construction via Atlas-Based landmarking and volumetric elastic registration. In Insana, M. F. and Leahy, R. M., editors, *Information Processing in Medical Imaging*, volume 2082 of *LNCS*, pages 78–91, Berlin, Heidelberg. Springer Berlin Heidelberg. 2.2.3
- Frangi, A. F., Rueckert, D., Schnabel, J. A., and Niessen, W. J. (2002). Automatic construction of multiple-object three-dimensional statistical shape models: application to cardiac modeling. *IEEE Transactions on Medical Imaging*, 21(9):1151–1166. 2.2.3
- Free, S., Bergin, P., Fish, D., Cook, M., Shorvon, S., and Stevens, J. (1995). Methods for normalization of hippocampal volumes measured with MR. *AJNR Am J Neuroradiol*, 16(4):637–643. 2.3.1
- Freund, Y. and Schapire, R. (1995). A decision-theoretic [sic] generalization of on-line learning and an application to boosting. In Vitányi, P., editor, *Computational Learning Theory*, volume 904 of *LNCS*, pages 23–37. Springer Berlin / Heidelberg. 2.1.2
- Frisoni, G., Testa, C., Zorzan, A., Sabbatoli, F., Beltramello, A., Soininen, H., and Laakso, M. (2002). Detection of grey matter loss in mild alzheimer’s disease with voxel based morphometry. *Journal of Neurology, Neurosurgery, and Psychiatry*, 73(6):657–664. 2.3.1
- Frisoni, G. B., Fox, N. C., Jack, C. R., Scheltens, P., and Thompson, P. M. (2010). The clinical use of structural MRI in Alzheimer disease. *Nat Rev Neurol*, 6(2):67–77. 1.1.3.2, 1.5
- Frisoni, G. B., Ganzola, R., Canu, E., Rub, U., Pizzini, F. B., Alessandrini, F., Zoccatelli, G., Beltramello, A., Caltagirone, C., and Thompson, P. M. (2008). Mapping local hippocampal changes in Alzheimer’s disease and normal ageing with MRI at 3 Tesla. *Brain*, pages 3266–3276. 2.3.2

- Frisoni, G. B., Prestia, A., Rasser, P. E., Bonetti, M., and Thompson, P. M. (2009). In vivo mapping of incremental cortical atrophy from incipient to overt Alzheimer's disease. *Journal of Neurology*, 256(6):916–924. 1.1.3.2
- Friston, K. J., Ashburner, J., Frith, C. D., Poline, J. ., Heather, J. D., and Frackowiak, R. S. J. (1995). Spatial registration and normalization of images. *Human Brain Mapping*, 3(3):165–189. 2.1.2.3
- Garland, M. and Heckbert, P. S. (1997). Surface simplification using quadric error metrics. In *Proceedings of the 24th annual conference on Computer graphics and interactive techniques*, SIGGRAPH '97, page 209–216, New York, NY, USA. ACM Press/Addison-Wesley Publishing Co. 4.3.2
- Gerardin, E., Chételat, G., et al. (2009). Multidimensional classification of hippocampal shape features discriminates Alzheimer's disease and mild cognitive impairment from normal aging. *NeuroImage*, 47(4):1476–1486. 2.3.2, 5.3
- Gerig, G., Styner, M., Jones, D., Weinberger, D., and Lieberman, J. (2001). Shape analysis of brain ventricles using SPHARM. In *Proceedings of the IEEE Workshop on Mathematical Methods in Biomedical Image Analysis (MMBIA'01)*, page 171. IEEE Computer Society. 2.3.2
- Geuze, E., Vermetten, E., and Bremner, J. D. (2004). MR-based in vivo hippocampal volumetrics: 1. review of methodologies currently employed. *Molecular Psychiatry*, 10(2):147–159. 2.1.1
- Ghanei, A. and Soltanian-Zadeh, H. (2002). A discrete curvature-based deformable surface model with application to segmentation of volumetric images. *IEEE Transactions on Information Technology in Biomedicine*, 6(4):285–295. 2.1.2.1
- Ghanei, A., Soltanian-Zadeh, H., Elisevich, K., and Fessler, J. A. (2001). Knowledge-based deformable surface model with application to segmentation of brain structures in MRI. In *Medical Imaging 2001: Image Processing, Proceedings of SPIE*, volume 4322, pages 356–365, San Diego, CA, USA. 2.1.2.1

- Ghanei, A., Soltanian-Zadeh, H., and Windham, J. P. (1998). A 3D deformable surface model for segmentation of objects from volumetric data in medical images. *Computers in Biology and Medicine*, 28(3):239–253. 2.1.2.1
- Goedert, M. and Spillantini, M. G. (2006). A century of Alzheimer’s disease. *Science*, 314(5800):777–781. 1.2, 1.1.1
- Goodall, C. (1991). Procrustes methods in the statistical analysis of shape. *Journal of the Royal Statistical Society. Series B (Methodological)*, 53(2):285–339. 2.2.2
- Gosche, K. M., Mortimer, J. A., Smith, C. D., Markesbery, W. R., and Snowdon, D. A. (2002). Hippocampal volume as an index of Alzheimer neuropathology: Findings from the nun study. *Neurology*, 58(10):1476–1482. 1.1.3.2
- Gower, J. C. (1975). Generalized Procrustes analysis. *Psychometrika*, 40(1):33–51. 2.2.2, 5.1
- Gower, J. C. (2010). Procrustes methods. *Wiley Interdisciplinary Reviews: Computational Statistics*, 2:503–508. 2.2.2
- Gower, J. C. and Dijksterhuis, G. B. (2004). *Procrustes Problems*. Oxford University Press, USA. 2.2.2
- Granger, S. and Pennec, X. (2002). Multi-scale EM-ICP: a fast and robust approach for surface registration. In *Proceedings of the 7th European Conference on Computer Vision-Part IV, ECCV ’02*, pages 418–432, London. Springer-Verlag. 2.2.2, 4.2
- Gu, X., Wang, Y., Chan, T. F., Thompson, P. M., and Yau, S. (2004). Genus zero surface conformal mapping and its application to brain surface mapping. *IEEE Transactions on Medical Imaging*, 23(8):949–958. 2.2.3
- Gu, X. and Yau, S. (2003). Global conformal surface parameterization. In *Proceedings of the 2003 Eurographics/ACM SIGGRAPH symposium on Geometry processing, SGP ’03*, pages 127–137, Aachen, Germany. Eurographics Association. ACM ID: 882388. 2.2.3

- Gutman, B., Wang, Y., et al. (2009). Disease classification with hippocampal shape invariants. *Hippocampus*, 19(6):572–578. 2.3.2
- Haacke, E. M., Brown, R. W., Thompson, M. R., and Venkatesan, R. (1999). *Magnetic Resonance Imaging: Physical Principles and Sequence Design*. Wiley-Liss, 1st edition. 1.1.3.1
- Hachinski, V. C., Lassen, N. A., and Marshall, J. (1974). Multi-infarct dementia: A cause of mental deterioration in the elderly. *The Lancet*, 304(7874):207–209. 1.1.1
- Haker, S., Angenent, S., Tannenbaum, A., Kikinis, R., Sapiro, G., and Halle, M. (2000). Conformal surface parameterization for texture mapping. *IEEE Transactions on Visualization and Computer Graphics*, 6(2):181–189. 2.2.3
- Haller, J. W., Banerjee, A., Christensen, G. E., Gado, M., Joshi, S., Miller, M. I., Sheline, Y., Vannier, M. W., and Csernansky, J. G. (1997). Three-dimensional hippocampal MR morphometry with high-dimensional transformation of a neuroanatomic atlas. *Radiology*, 202(2):504–510. 2.1.2.3
- Haller, J. W., Christensen, G. E., Joshi, S. C., Newcomer, J. W., Miller, M. I., Csernansky, J. G., and Vannier, M. W. (1996). Hippocampal MR imaging morphometry by means of general pattern matching. *Radiology*, 199(3):787–791. 2.1.2.3
- Harding, A. J., Halliday, G. M., and Kril, J. J. (1998). Variation in hippocampal neuron number with age and brain volume. *Cerebral Cortex*, 8(8):710–718. 5.13
- Hartmann, S. L., Parks, M. H., Martin, P. R., and Dawant, B. M. (1999). Automatic 3-D segmentation of internal structures of the head in MR images using a combination of similarity and free-form transformations. II. validation on severely atrophied brains. *IEEE Transactions on Medical Imaging*, 18(10):917–926. 2.1.2.3

- Heckemann, R. A., Hajnal, J. V., Aljabar, P., Rueckert, D., and Hammers, A. (2006). Automatic anatomical brain MRI segmentation combining label propagation and decision fusion. *NeuroImage*, 33(1):115–126. 2.1.2.3
- Heimann, T. and Meinzer, H. (2009). Statistical shape models for 3D medical image segmentation: A review. *Medical Image Analysis*, 13(4):543–563. 2.2.1, 2.2.3, 2.2.4, 5.5.3
- Henson, R. (2005). A mini-review of fMRI studies of human medial temporal lobe activity associated with recognition memory. *The Quarterly Journal of Experimental Psychology. B, Comparative and Physiological Psychology*, 58(3-4):340–360. 5.6.4
- Heun, R., Mazanek, M., Atzor, K. R., Tintera, J., Gawehn, J., Burkart, M., Gänssicke, M., Falkai, P., and Stoeter, P. (1997). Amygdala-hippocampal atrophy and memory performance in dementia of Alzheimer type. *Dementia and Geriatric Cognitive Disorders*, 8(6):329–336. 5.4
- Hladůvka, J. and Bühler, K. (2005). MDL spline models: Gradient and polynomial reparameterisations. In Clocksin, W. F., Fitzgibbon, A. W., and Torr, P. H. S., editors, *BMVC '05*. British Machine Vision Association. 2.2.3, 4.1.3.2
- Hogan, R. E., Mark, K. E., Wang, L., Joshi, S., Miller, M. I., and Bucholz, R. D. (2000). Mesial temporal sclerosis and temporal lobe epilepsy: MR imaging deformation-based segmentation of the hippocampus in five patients¹. *Radiology*, 216(1):291–297. 2.1.2.3
- Horn, B. K. and Schunck, B. G. (1981). Determining optical flow. *Artificial Intelligence*, 17(1-3):185–203. 3.1.1.2
- Hsu, Y.-Y., Schuff, N., Du, A.-T., Mark, K., Zhu, X., Hardin, D., and Weiner, M. W. (2002). Comparison of automated and manual MRI volumetry of hippocampus in normal aging and dementia. *Journal of Magnetic Resonance Imaging*, 16(3):305–310. 2.1.1, 2.3.1, 3.4.2.1

- Hufnagel, H., Pennec, X., Ehrhardt, J., Ayache, N., and Handels, H. (2009). Computation of a probabilistic statistical shape model in a maximum-a-posteriori framework. *Methods of Information in Medicine*, 48(4):314–319. 2.2.3, 4.2
- Huxley, J. (1932). *Problems of Relative Growth*. Methuen, London. 2.2
- Hyvärinen, A., Karhunen, J., and Oja, E. (2001). *Independent Component Analysis*. Wiley-Interscience, 1 edition. 2.2.4
- Iosifescu, D. V., Shenton, M. E., Warfield, S. K., Kikinis, R., Dengler, J., Jolesz, F. A., and McCarley, R. W. (1997). An automated registration algorithm for measuring MRI subcortical brain structures. *NeuroImage*, 6(1):13–25. 2.1.2.3
- Ivnik, R. J., Malec, J. F., Smith, G. E., Tangalos, E. G., Petersen, R. C., Kokmen, E., and Kurland, L. T. (1992). Mayo’s older americans normative studies: Updated AVLT - norms for ages 56 to 97. *Clinical Neuropsychologist*, 6(1, Supplement 1):83–104. 5.4
- Jack, C., Shiung, M., Gunter, J., O’Brien, P., Weigand, S., Knopman, D., Boeve, B., Ivnik, R., Smith, G., Cha, R., Tangalos, E., and Petersen, R. (2004). Comparison of different MRI brain atrophy rate measures with clinical disease progression in AD. *Neurology*, 62(4):591–600. 1.1.3.2, 2.3.1
- Jack, C. R., Dickson, D. W., Parisi, J. E., Xu, Y. C., Cha, R. H., O’Brien, P. C., Edland, S. D., Smith, G. E., Boeve, B. F., Tangalos, E. G., Kokmen, E., and Petersen, R. C. (2002). Antemortem MRI findings correlate with hippocampal neuropathology in typical aging and dementia. *Neurology*, 58(5):750–757. 1.1.3.2
- Jack, C. R., Petersen, R. C., Xu, Y., O’Brien, P. C., Smith, G. E., Ivnik, R. J., Tangalos, E. G., and Kokmen, E. (1998). The rate of medial temporal lobe atrophy in typical aging and Alzheimer’s disease. *Neurology*, 51(4):993–999. 5.6.2
- Jack, C. R., Slomkowski, M., Gracon, S., Hoover, T. M., Felmlee, J. P., Stewart, K., Xu, Y., Shiung, M., O’Brien, P. C., Cha, R., Knopman, D., and Petersen,

- R. C. (2003). MRI as a biomarker of disease progression in a therapeutic trial of milameline for AD. *Neurology*, 60(2):253–260. 1.1.3.2
- Järvenpää, T., Laakso, M. P., Rossi, R., Koskenvuo, M., Kaprio, J., Rähkä, I., Kurki, T., Laine, M., Frisoni, G. B., and Rinne, J. O. (2004). Hippocampal MRI volumetry in cognitively discordant monozygotic twin pairs. *Journal of Neurology, Neurosurgery & Psychiatry*, 75(1):116–120. 2.3.1
- Jenkinson, M., Bannister, P., Brady, M., and Smith, S. (2002). Improved optimization for the robust and accurate linear registration and motion correction of brain images. *NeuroImage*, 17(2):825–841. 2.1.2.3
- Jian, B. and Vemuri, B. C. (2010). Robust point set registration using gaussian mixture models. *IEEE Transactions on Pattern Analysis and Machine Intelligence*. 4.2
- Johnston, D. and Amaral, D. G. (1997). Hippocampus. In Shepherd, G. M., editor, *The synaptic organization of the brain*, pages 417–458. Oxford University Press, New York. 1.1.2
- Jolicoeur, P. and Mosimann, J. E. (1960). Size and shape variation in the painted turtle. a principal component analysis. *Growth*, 24:339–354. 2.2
- Josephs, K. A., Whitwell, J. L., Ahmed, Z., Shiung, M. M., Weigand, S. D., Knopman, D. S., Boeve, B. F., Parisi, J. E., Petersen, R. C., Dickson, D. W., and Jack Jr, C. R. (2008). β -amyloid burden is not associated with rates of brain atrophy. *Annals of Neurology*, 63(2):204–212. 1.1.3.2
- Jost, T. and Hugli, H. (2003). A multi-resolution ICP with heuristic closest point search for fast and robust 3D registration of range images. In *Fourth International Conference on 3-D Digital Imaging and Modeling, 2003. 3DIM 2003. Proceedings*, pages 427–433. IEEE. 2.2.2
- Kelemen, A., Szekely, G., and Gerig, G. (1999). Elastic model-based segmentation of 3-D neuroradiological data sets. *IEEE Transactions on Medical Imaging*, 18(10):828–839. 2.1.2.2, 2.2.3

- Kendall, D. G. (1977). The diffusion of shape. *Advances in Applied Probability*, 9(3):428–430. 2.2
- Kendall, D. G. (1984). Shape manifolds, procrustean metrics, and complex projective spaces. *Bulletin of the London Mathematical Society*, 16(2):81–121. 2.2, 5.2
- Kendall, D. G. (1989). A survey of the statistical theory of shape. *Statistical Science*, 4(2):87–99. 2.2
- Kendall, D. G., Barden, D., Carne, T. K., and Le, H. (1999). *Shape and shape theory*. Wiley, New York. 2.2, 2.2
- Khan, A. R., Cherbuin, N., Wen, W., Anstey, K. J., Sachdev, P., and Beg, M. F. (2011). Optimal weights for local multi-atlas fusion using supervised learning and dynamic information (SuperDyn): validation on hippocampus segmentation. *NeuroImage*, 56(1):126–139. 2.1.2.3
- Khan, A. R., Wang, L., and Beg, M. F. (2008). FreeSurfer-initiated fully-automated subcortical brain segmentation in MRI using large deformation diffeomorphic metric mapping. *NeuroImage*, 41(3):735–746. 2.1.2.3
- Klemencic, J., Pluim, J., Viergever, M., Schnack, H., and Valencic, V. (2004). Non-rigid registration based active appearance models for 3D medical image segmentation. *Journal of Imaging Science and Technology*, 48(2):166–171. 2.1.2.3
- Kloppel, S., Stonnington, C. M., Chu, C., Draganski, B., Scahill, R. I., Rohrer, J. D., Fox, N. C., Jack, C. R., Ashburner, J., and Frackowiak, R. S. J. (2008). Automatic classification of MR scans in Alzheimer’s disease. *Brain*, 131(3):681–689. 5.3
- Kolmogorov, V. and Zabini, R. (2004). What energy functions can be minimized via graph cuts? *IEEE Transactions on Pattern Analysis and Machine Intelligence*, 26(2):147–159. 2.1.2.3

- Konrad, C., Ukas, T., Nebel, C., Arolt, V., Toga, A., and Narr, K. (2009). Defining the human hippocampus in cerebral magnetic resonance images—An overview of current segmentation protocols. *NeuroImage*, 47(4):1185–1195. 2.1.1
- Korf, E. S. C., Wahlund, L., Visser, P. J., and Scheltens, P. (2004). Medial temporal lobe atrophy on MRI predicts dementia in patients with mild cognitive impairment. *Neurology*, 63(1):94–100. 1.1.3.2
- Kotcheff, A. C. and Taylor, C. J. (1998). Automatic construction of eigenshape models by direct optimization. *Medical Image Analysis*, 2(4):303–314. 2.2.3
- Kovacevic, S., Rafii, M. S., and Brewer, J. B. (2009). High-throughput, fully automated volumetry for prediction of MMSE and CDR decline in mild cognitive impairment. *Alzheimer Disease & Associated Disorders*, 23(2):139–145. 1.1.3.2
- Kraepelin, E. (1910). *Psychiatrie: ein Lehrbuch für Studierende und Ärzte*. Barth, Leipzig. 1.1.1
- La Joie, R., Fouquet, M., Mézenge, F., Landeau, B., Villain, N., Mevel, K., Pélerin, A., Eustache, F., Desgranges, B., and Chételat, G. (2010). Differential effect of age on hippocampal subfields assessed using a new high-resolution 3T MR sequence. *NeuroImage*, 53(2):506–514. 5.6.2, 5.6.2, 5.13
- Laga, H., Takahashi, H., and Nakajima, M. (2006). Spherical wavelet descriptors for content-based 3D model retrieval. In *IEEE International Conference on Shape Modeling and Applications, 2006. SMI 2006*, pages 15–15. IEEE. 2.2.1
- Larsen, R., Eiriksson, H., and Stegmann, M. B. (2001). Q-MAF shape decomposition. In Niessen, W. J. and Viergever, M. A., editors, *Medical Image Computing and Computer-Assisted Intervention – MICCAI 2001*, volume 2208 of *LNCS*, pages 837–844, Berlin, Heidelberg. Springer Berlin Heidelberg. 2.2.2
- Leff, H. S. and Rex, A. F. (1990). Resource letter MD-1: Maxwell’s demon. *American Journal of Physics*, 58(3):201. 1

- Lein, E. S., Callaway, E. M., Albright, T. D., and Gage, F. H. (2005). Redefining the boundaries of the hippocampal CA2 subfield in the mouse using gene expression and 3-dimensional reconstruction. *The Journal of Comparative Neurology*, 485(1):1–10. 1.1.2
- Leung, K. K., Barnes, J., Ridgway, G. R., Bartlett, J. W., Clarkson, M. J., Macdonald, K., Schuff, N., Fox, N. C., and Ourselin, S. (2010). Automated cross-sectional and longitudinal hippocampal volume measurement in mild cognitive impairment and Alzheimer’s disease. *NeuroImage*, 51(4):1345–1359. 2.1.2.3
- Levitt, M. H. (2008). *Spin Dynamics: Basics of Nuclear Magnetic Resonance*. Wiley, 2 edition. 1.1.3.1
- Li, S., Shi, F., Pu, F., Li, X., Jiang, T., Xie, S., and Wang, Y. (2007). Hippocampal shape analysis of Alzheimer disease based on machine learning methods. *AJNR Am J Neuroradiol*, 28(7):1339–1345. 2.3.2
- Lorensen, W. E. and Cline, H. E. (1987). Marching cubes: A high resolution 3D surface construction algorithm. *SIGGRAPH Computer Graphics*, 21(4):163–169. 2.2.1, 4.1
- Lorente de Nó, R. (1934). Studies on the structure of the cerebral cortex. II. Continuation of the study of the ammonic system. *Journal für Psychologie und Neurologie*, 46:113–177. 1.1.2
- Lötjönen, J. M., Wolz, R., Koikkalainen, J. R., Thurfjell, L., Waldemar, G., Soininen, H., and Rueckert, D. (2010). Fast and robust multi-atlas segmentation of brain magnetic resonance images. *NeuroImage*, 49(3):2352–2365. 2.1.2.3
- Loughrey, J. and Cunningham, P. (2005). Overfitting in wrapper-based feature subset selection: The harder you try the worse it gets. In *Research and Development in Intelligent Systems XXI*, pages 33–43. 5.3
- Lynch, M. A. (2004). Long-term potentiation and memory. *Physiological Reviews*, 84(1):87–136. 1.1.2

- Mahony, R. and Manton, J. H. (2002). The geometry of the newton method on non-compact lie groups. *Journal of Global Optimization*, 23:309–327. 3.1.1.2
- Makris, N., Kennedy, D. N., Meyer, J., Worth, A., Jr., V. S. C., Seidman, L., Goldstein, J., Goodman, J., Hoge, E., Macpherson, C., Tourville, J., Klaveness, S., Hodge, S. M., Melrose, R., Rauch, S., Kim, H., Harris, G., Boehland, A., Glode, B., Koch, J., Segal, E., Sonricker, A., Dieterich, M., Papadimitriou, G., Normandin, J. J., Cullen, N., Boriel, D., and Sanders, H. (2004). *General Brain Segmentation: Method and Utilization*. Center for Morphometric Analysis, Massachusetts General Hospital. 2.1.1, 2.3, 3.2.1
- Malis, E. (2004). Improving vision-based control using efficient second-order minimization techniques. In *2004 IEEE International Conference on Robotics and Automation, 2004. Proceedings. ICRA '04*, volume 2, pages 1843–1848 Vol.2. IEEE. 3.1.1.2
- Malykhin, N. V., Bouchard, T. P., Camicioli, R., and Coupland, N. J. (2008). Aging hippocampus and amygdala. *NeuroReport*, 19(5):543–547. 5.6.2
- Martini, F. H., Timmons, M. J., and Tallitsch, R. B. (2002). *Human Anatomy*. Benjamin Cummings, 4th edition. 1.3
- Martucci, S. A. (1994). Symmetric convolution and the discrete sine and cosine transforms. *IEEE Transactions on Signal Processing*, 42(5):1038–1051. 4.1.3.3
- Maruyama, K., Nori, F., and Vedral, V. (2009). Colloquium: The physics of Maxwell’s demon and information. *Reviews of Modern Physics*, 81(1):1. 1
- Matheny, A. and Goldgof, D. B. (1995). The use of three- and four-dimensional surface harmonics for rigid and nonrigid shape recovery and representation. *IEEE Transactions on Pattern Analysis and Machine Intelligence*, 17(10):967–981. 2.2.1
- Maurer, K., Volk, S., and Gerbaldo, H. (1997). Auguste D and Alzheimer’s disease. *The Lancet*, 349(9064):1546–1549. 1.1.1

- Mazziotta, J., Toga, A., Evans, A., Fox, P., Lancaster, J., Zilles, K., Woods, R., Paus, T., Simpson, G., Pike, B., Holmes, C., Collins, L., Thompson, P., MacDonald, D., Iacoboni, M., Schormann, T., Amunts, K., Palomero-Gallagher, N., Geyer, S., Parsons, L., Narr, K., Kabani, N., Goualher, G. L., Boomsma, D., Cannon, T., Kawashima, R., and Mazoyer, B. (2001). A probabilistic atlas and reference system for the human brain: International consortium for brain mapping (ICBM). *Philosophical Transactions of the Royal Society of London. Series B: Biological Sciences*, 356(1412):1293–1322. 2.1.1
- McEvoy, L. K. and Brewer, J. B. (2010). Quantitative structural MRI for early detection of Alzheimer’s disease. *Expert Review of Neurotherapeutics*, 10(11):1675–1688. 1.1.3.2
- McKhann, G., Drachman, D., Folstein, M., Katzman, R., Price, D., and Stadlan, E. M. (1984). Clinical diagnosis of Alzheimer’s disease: report of the NINCDS-ADRDA work group under the auspices of department of health and human services task force on Alzheimer’s disease. *Neurology*, 34(7):939–944. 1.1.1
- Mercer, A., Trigg, H. L., and Thomson, A. M. (2007). Characterization of neurons in the CA2 subfield of the adult rat hippocampus. *The Journal of Neuroscience*, 27(27):7329–7338. 1.1.2
- Miller, M. I., Beg, M. F., Ceritoglu, C., and Stark, C. (2005). Increasing the power of functional maps of the medial temporal lobe by using large deformation diffeomorphic metric mapping. *Proceedings of the National Academy of Sciences of the United States of America*, 102(27):9685–9690. 2.1.2.3, 3.1.1.2
- Miller, M. I., Christensen, G. E., Amit, Y., and Grenander, U. (1993). Mathematical textbook of deformable neuroanatomies. *Proceedings of the National Academy of Sciences*, 90(24):11944–11948. 2.1.2.3
- Morra, J. H., Tu, Z., Apostolova, L. G., Green, A. E., Avedissian, C., Madsen, S. K., Parikshak, N., Hua, X., Toga, A. W., Jack Jr., C. R., Schuff, N., Weiner, M. W., and Thompson, P. M. (2009). Automated 3D mapping of hippocampal atrophy and its clinical correlates in 400 subjects with Alzheimer’s

- disease, mild cognitive impairment, and elderly controls. *Human Brain Mapping*, 30(9):2766–2788. 1.1.3.2
- Mosimann, J. E. (1970). Size allometry: Size and shape variables with characterizations of the lognormal and generalized gamma distributions. *Journal of the American Statistical Association*, 65(330):930–945. 2.2
- Mueller, S. G., Schuff, N., Yaffe, K., Madison, C., Miller, B., and Weiner, M. W. (2010). Hippocampal atrophy patterns in mild cognitive impairment and Alzheimer’s disease. *Human Brain Mapping*, 31(9):1339–1347. 5.6.2
- Mueller, S. G. and Weiner, M. W. (2009). Selective effect of age, Apo e4, and Alzheimer’s disease on hippocampal subfields. *Hippocampus*, 19(6):558–564. 2.3.2
- Munson, M. A. and Caruana, R. (2009). On feature selection, Bias-Variance, and bagging. In *Proceedings of the European Conference on Machine Learning and Knowledge Discovery in Databases: Part II*, pages 144–159, Bled, Slovenia. Springer-Verlag. 5.3
- Mura, T., Dartigues, J., and Berr, C. (2010). How many dementia cases in France and Europe? Alternative projections and scenarios 2010-2050. *European Journal of Neurology*, 17(2):252–259. 1.1.1
- Murgasova, M., Dyet, L., Edwards, D., Rutherford, M., Hajnal, J., and Rueckert, D. (2007). Segmentation of brain MRI in young children. *Academic Radiology*, 14(11):1350–1366. 2.1.2.3
- Murgasova, M., Dyet, L., Edwards, D., Rutherford, M., Hajnal, J. V., and Rueckert, D. (2006). Segmentation of brain MRI in young children. In Larsen, R., Nielsen, M., and Sporring, J., editors, *Medical Image Computing and Computer-Assisted Intervention – MICCAI 2006*, volume 4190 of *LNCS*, pages 687–694, Berlin, Heidelberg. Springer Berlin Heidelberg. 2.1.2.3
- Murphy, M. P. and LeVine, H. (2010). Alzheimer’s disease and the β -amyloid peptide. *Journal of Alzheimer’s disease*, 19(1):311–323. 1.1.1

- Nain, D., Haker, S., Bobick, A., and Tannenbaum, A. (2007). Multiscale 3-D shape representation and segmentation using spherical wavelets. *IEEE Transactions on Medical Imaging*, 26(4):598–618. 2.2.1
- Newman, T. S. and Yi, H. (2006). A survey of the marching cubes algorithm. *Computers & Graphics*, 30(5):854–879. 2.2.1
- O’Higgins, P. and Dryden, I. L. (1993). Sexual dimorphism in hominoids: further studies of craniofacial shape differences in pan, gorilla and pongo. *Journal of Human Evolution*, 24(3):183–205. 4
- Ourselin, S., Roche, A., Subsol, G., Pennec, X., and Ayache, N. (2001). Reconstructing a 3D structure from serial histological sections. *Image and Vision Computing*, 19(1-2):25–31. 3.1.1.1, 3.4.2.2, 5.3
- Patenaude, B., Smith, S. M., Kennedy, D. N., and Jenkinson, M. (2011). A bayesian model of shape and appearance for subcortical brain segmentation. *NeuroImage*, 56(3):907–922. 2.1.2.2
- Paulsen, R. R. and Hilger, K. B. (2003). Shape modelling using markov random field restoration of point correspondences. In Taylor, C. and Noble, J. A., editors, *Information Processing in Medical Imaging*, volume 2732 of *LNCS*, pages 1–12, Berlin, Heidelberg. Springer Berlin Heidelberg. 2.2.3
- Pérez de Alejo, R., Ruiz-Cabello, J., Cortijo, M., Rodriguez, I., Echave, I., Regadera, J., Arrazola, J., Avilés, P., Barreiro, P., Gargallo, D., and Graña, M. (2003). Computer-assisted enhanced volumetric segmentation magnetic resonance imaging data using a mixture of artificial neural networks. *Magnetic Resonance Imaging*, 21(8):901–912. 2.1.2
- Petersen, R., Jack, C., Xu, Y., Waring, S., O’Brien, P., Smith, G., Ivnik, R., Tangalos, E., Boeve, B. F., and Kokmen, E. (2000). Memory and MRI-based hippocampal volumes in aging and AD. *Neurology*, 54(3):581. 5.4

- Petersen, R. C., Smith, G. E., Waring, S. C., Ivnik, R. J., Tangalos, E. G., and Kokmen, E. (1999). Mild cognitive impairment: Clinical characterization and outcome. *Archives of Neurology*, 56(3):303–308. 1.1.1
- Pieper, S., Lorensen, B., Schroeder, W., and Kikinis, R. (2006). The NA-MIC kit: ITK, VTK, pipelines, grids and 3D slicer as an open platform for the medical image computing community. In *Biomedical Imaging: Nano to Macro, 2006. 3rd IEEE International Symposium on*, pages 698–701. 2.1
- Pitiot, A., Delingette, H., Thompson, P. M., and Ayache, N. (2004). Expert knowledge-guided segmentation system for brain MRI. *NeuroImage*, 23(Supplement 1):S85–S96. 2.1.2.2
- Pizer, S. M., Fletcher, P. T., Joshi, S., Thall, A., Chen, J. Z., Fridman, Y., Fritsch, D. S., Gash, A. G., Glotzer, J. M., Jiroutek, M. R., Lu, C., Muller, K. E., Tracton, G., Yushkevich, P., and Chaney, E. L. (2003). Deformable *M-Reps* for 3D medical image segmentation. *International Journal of Computer Vision*, 55:85–106. 2.2.1
- Pizer, S. M., Fritsch, D. S., Yushkevich, P. A., Johnson, V. E., and Chaney, E. L. (1999). Segmentation, registration, and measurement of shape variation via image object shape. *IEEE Transactions on Medical Imaging*, 18(10):851–865. 2.2.1
- Pluim, J. P., Maintz, J. B., and Viergever, M. A. (2003). Mutual-information-based registration of medical images: a survey. *IEEE Transactions on Medical Imaging*, 22(8):986–1004. 3.1.2.1
- Pohl, K. M., Fisher, J., Shenton, M., McCarley, R. W., Grimson, W. E. L., Kikinis, R., and Wells, W. M. (2006). Logarithm odds maps for shape representation. In Larsen, R., Nielsen, M., and Sporring, J., editors, *Medical Image Computing and Computer-Assisted Intervention – MICCAI 2006*, volume 4191 of *LNCS*, pages 955–963, Berlin, Heidelberg. Springer Berlin Heidelberg. 2.2.1

- Praun, E. and Hoppe, H. (2003). Spherical parametrization and remeshing. In *ACM SIGGRAPH 2003 Papers*, SIGGRAPH '03, pages 340–349, San Diego, California. ACM. 4.4, 4.1.3.1, 4.5
- Qiu, A., Fennema-Notestine, C., Dale, A. M., and Miller, M. I. (2009). Regional shape abnormalities in mild cognitive impairment and Alzheimer’s disease. *NeuroImage*, 45(3):656–661. 2.3.2
- Ramón y Cajal, S. (1911). *Histologie du Système Nerveux de l’Homme et des Vertébrés*, volume I and II. Maloine, Paris. 1.1.2
- Ramón y Cajal, S. (1968). *The structure of Ammon’s horn*. C.C. Thomas, Springfield Illinois. 1.1.2
- Ramón y Cajal, S. (1995). *Histology of the nervous system of man and vertebrates*. Oxford University Press, New York. 1.1.2
- Reunanen, J. (2003). Overfitting in making comparisons between variable selection methods. *J. Mach. Learn. Res.*, 3:1371–1382. 5.3
- Reyment, R. A., Blackith, R. E., and Campbell, N. A. (1984). *Multivariate morphometrics*. Academic Press, London, Orlando, second edition. 2.2
- Ridha, B. H., Anderson, V. M., Barnes, J., Boyes, R. G., Price, S. L., Rossor, M. N., Whitwell, J. L., Jenkins, L., Black, R. S., Grundman, M., and Fox, N. C. (2008). Volumetric MRI and cognitive measures in Alzheimer disease. *Journal of Neurology*, 255(4):567–574. 1.1.3.2
- Rohlfing, T., Brandt, R., Menzel, R., and Maurer, C. R. (2004a). Evaluation of atlas selection strategies for atlas-based image segmentation with application to confocal microscopy images of bee brains. *NeuroImage*, 21(4):1428–1442. 2.1.2.3
- Rohlfing, T., Russakoff, D., and Maurer, C. (2004b). Performance-based classifier combination in atlas-based image segmentation using expectation-maximization parameter estimation. *Medical Imaging, IEEE Transactions on*, 23(8):983–994. 2.1.2.3

- Rorden, C. and Brett, M. (2000). Stereotaxic display of brain lesions. *Behavioural Neurology*, 12(4):191–200. 2.1
- Rössler, M., Zarski, R., Bohl, J., and Ohm, T. G. (2002). Stage-dependent and sector-specific neuronal loss in hippocampus during Alzheimer’s disease. *Acta Neuropathologica*, 103(4):363–369. 2.3.2
- Roth, M., Tomlinson, B. E., and Blessed, G. (1966). Correlation between scores for dementia and counts of ‘senile plaques’ in cerebral grey matter of elderly subjects. *Nature*, 209(5018):109–110. 1.1.1
- Rueckert, D., Frangi, A. F., and Schnabel, J. A. (2003). Automatic construction of 3-D statistical deformation models of the brain using nonrigid registration. *IEEE Transactions on Medical Imaging*, 22(8):1014–1025. 2.2.3
- Rusinkiewicz, S. and Levoy, M. (2001). Efficient variants of the ICP algorithm. In *3D Digital Imaging and Modeling, International Conference on*, volume 0, page 145, Los Alamitos, CA, USA. IEEE Computer Society. 2.2.2
- Sabuncu, M. R., Yeo, B. T. T., Van Leemput, K., Fischl, B., and Golland, P. (2010). A generative model for image segmentation based on label fusion. *Medical Imaging, IEEE Transactions on*, 29(10):1714–1729. 2.1.2.3
- Scahill, R. I., Frost, C., Jenkins, R., Whitwell, J. L., Rossor, M. N., and Fox, N. C. (2003). A longitudinal study of brain volume changes in normal aging using serial registered magnetic resonance imaging. *Arch Neurol*, 60(7):989–994. 2.1.1
- Scheltens, P., Leys, D., Barkhof, F., Huglo, D., Weinstein, H. C., Vermersch, P., Kuiper, M., Steinling, M., Wolters, E. C., and Valk, J. (1992). Atrophy of medial temporal lobes on MRI in “probable” Alzheimer’s disease and normal ageing: diagnostic value and neuropsychological correlates. *Journal of Neurology, Neurosurgery & Psychiatry*, 55(10):967–972. 1.1.3.2
- Scher, A. I., Xu, Y., Korf, E. S. C., White, L. R., Scheltens, P., Toga, A. W., Thompson, P. M., Hartley, S. W., Witter, M. P., Valentino, D. J., and Launer,

- L. J. (2007). Hippocampal shape analysis in Alzheimer’s disease: A population-based study. *NeuroImage*, 36(1):8–18. 2.3.2
- Schölkopf, B., Smola, A., and Müller, K. (1998). Nonlinear component analysis as a kernel eigenvalue problem. *Neural Computation*, 10(5):1299–1319. 2.2.4
- Schölkopf, B. and Smola, A. J. (2002). *Learning with kernels: support vector machines, regularization, optimization, and beyond*. MIT Press. 5.3
- Schott, J., Crutch, S., Frost, C., Warrington, E., Rossor, M., and Fox, N. (2008). Neuropsychological correlates of whole brain atrophy in Alzheimer’s disease. *Neuropsychologia*, 46(6):1732–1737. 1.1.3.2
- Schott, J. M., Fox, N. C., Frost, C., Scahill, R. I., Janssen, J. C., Chan, D., Jenkins, R., and Rossor, M. N. (2003). Assessing the onset of structural change in familial alzheimer’s disease. *Annals of Neurology*, 53(2):181–188. 2.1.1
- Sdika, M. (2010). Combining atlas based segmentation and intensity classification with nearest neighbor transform and accuracy weighted vote. *Medical Image Analysis*, 14(2):219–226. 2.1.2.3, 3.3
- Sethian, J. A. (1996). A fast marching level set method for monotonically advancing fronts. *Proceedings of the National Academy of Sciences*, 93(4):1591–1595. 2.1.2.1
- Sharp, G. C., Lee, S. W., and Wehe, D. K. (2002). ICP registration using invariant features. *IEEE Transactions on Pattern Analysis and Machine Intelligence*, 24(1):90–102. 2.2.2
- Shelton, C. R. (2000). Morphable surface models. *International Journal of Computer Vision*, 38:75–91. 2.2.3
- Shen, D., Moffat, S., Resnick, S. M., and Davatzikos, C. (2002). Measuring size and shape of the hippocampus in MR images using a deformable shape model. *NeuroImage*, 15(2):422–434. 2.1.2.2

- Shen, K., Bourgeat, P., Fripp, J., Meriaudeau, F., Ames, D., Ellis, K. A., Masters, C. L., Villemagne, V. L., Rowe, C. C., and Salvado, O. (2010). Supervised method to build an atlas database for multi-atlas segmentation-propagation. In Karssemeijer, N. and Summers, R. M., editors, *SPIE Medical Imaging 2010: Computer-Aided Diagnosis*, volume 7624, pages 76241N–8, San Diego, California, USA. 2.1.2.3
- Shi, F., Liu, B., Zhou, Y., Yu, C., and Jiang, T. (2009). Hippocampal volume and asymmetry in mild cognitive impairment and Alzheimer’s disease: Meta-analyses of MRI studies. *Hippocampus*, 19(11):1055–1064. 1.1.3.2, 2.3.1
- Simon, D. A., Hebert, M., and Kanade, T. (1995). Techniques for fast and accurate intrasurgical registration. *Journal of Image Guided Surgery*, 1(1):17–29. 2.2.2
- Slichter, C. P. (1990). *Principles of Magnetic Resonance*. Springer. 1.1.3.1
- Sluimer, J. D., Bouwman, F. H., Vrenken, H., Blankenstein, M. A., Barkhof, F., van der Flier, W. M., and Scheltens, P. (2010). Whole-brain atrophy rate and CSF biomarker levels in MCI and AD: a longitudinal study. *Neurobiology of Aging*, 31(5):758–764. 1.1.3.2
- Sluimer, J. D., van der Flier, W. M., Karas, G. B., Fox, N. C., Scheltens, P., Barkhof, F., and Vrenken, H. (2008). Whole-Brain atrophy rate and cognitive decline: Longitudinal MR study of memory clinic patients¹. *Radiology*, 248(2):590–598. 1.1.3.2
- Small, C. G. (1996). *The statistical theory of shape*. Springer, New York. 2.2
- Smith, S. M., Jenkinson, M., Woolrich, M. W., Beckmann, C. F., Behrens, T. E., Johansen-Berg, H., Bannister, P. R., De Luca, M., Drobnjak, I., Flitney, D. E., Niazy, R. K., Saunders, J., Vickers, J., Zhang, Y., De Stefano, N., Brady, J. M., and Matthews, P. M. (2004). Advances in functional and structural MR image analysis and implementation as FSL. *NeuroImage*, 23(Supplement 1):S208–S219. 2.1.2.2

- Stéphan, A., Laroche, S., and Davis, S. (2001). Generation of aggregated β -amyloid in the rat hippocampus impairs synaptic transmission and plasticity and causes memory deficits. *The Journal of Neuroscience*, 21(15):5703–5714. 1.1.2
- Studholme, C., Hill, D., and Hawkes, D. J. (1996). Incorporating connected region labelling into automated image registration using mutual information. In *Mathematical Methods in Biomedical Image Analysis, 1996., Proceedings of the Workshop on*, pages 23–31. 3.1.2, 3.1.2.1
- Styner, M. and Gerig, G. (2001). Medial models incorporating object variability for 3D shape analysis. In *Proceedings of the 17th International Conference on Information Processing in Medical Imaging*, pages 502–516. Springer-Verlag. 2.3.2
- Styner, M., Lieberman, J. A., Pantazis, D., and Gerig, G. (2004). Boundary and medial shape analysis of the hippocampus in schizophrenia. *Medical Image Analysis*, 8(3):197–203. 2.3.2
- Styner, M., Oguz, I., Xu, S., Brechbühler, C., Pantazis, D., and Gerig, G. (2006). Framework for the statistical shape analysis of brain structures using SPHARM-PDM. In *Insight Journal, Special Edition on the Open Science Workshop at MICCAI*. 4.1.2, 4.3
- Styner, M., Oguz, I., Xu, S., Pantazis, D., and Gerig, G. (2007). Statistical group differences in anatomical shape analysis using hotelling t2 metric. In Plum, J. P. W. and Reinhardt, J. M., editors, *Medical Imaging 2007: Image Processing*, volume 6512, pages 65123Z–11, San Diego, CA, USA. SPIE. 5.2.1
- Subsol, G., Thirion, J., and Ayache, N. (1998). A scheme for automatically building three-dimensional morphometric anatomical atlases: application to a skull atlas. *Medical Image Analysis*, 2(1):37–60. 2.2.3
- Suinesiaputra, A., Üzümcü, M., Frangi, A. F., Kaandorp, T. A. M., Reiber, J. H. C., and Lelieveldt, B. P. F. (2004). Detecting regional abnormal cardiac contraction in Short-Axis MR images using independent component analysis. In

- Barillot, C., Haynor, D. R., and Hellier, P., editors, *Medical Image Computing and Computer-Assisted Intervention – MICCAI 2004*, volume 3216 of *LNCS*, pages 737–744, Berlin, Heidelberg. Springer Berlin Heidelberg. 2.2.4
- Talairach, J. and Tournoux, P. (1988). *Co-Planar Stereotaxic Atlas of the Human Brain: 3-D Proportional System: An Approach to Cerebral Imaging*. Thieme. 2.1, 2.1.1
- Tartaglia, M. C., Rosen, H. J., and Miller, B. L. (2011). Neuroimaging in dementia. *Neurotherapeutics*, 8(1):82–92. 1.1.3
- Taubin, G., Zhang, T., and Golub, G. (1996). Optimal surface smoothing as filter design. In Buxton, B. and Cipolla, R., editors, *ECCV '96*, volume 1064 of *LNCS*, pages 283–292. 4.3.2
- Taupin, P. (2008). *The Hippocampus: Neurotransmission and Plasticity in the Nervous System*. Nova Science Publishers. 1.1.2
- Testa, C., Laakso, M. P., Sabbatoli, F., Rossi, R., Beltramello, A., Soininen, H., and Frisoni, G. B. (2004). A comparison between the accuracy of voxel-based morphometry and hippocampal volumetry in alzheimer’s disease. *Journal of Magnetic Resonance Imaging*, 19(3):274–282. 2.3.1
- Thirion, J. (1998). Image matching as a diffusion process: an analogy with maxwell’s demons. *Medical Image Analysis*, 2(3):243–260. 2.1.2.3, 3.1.1.2
- Thirion, J. P. (1996). Non-rigid matching using demons. In *Proceedings CVPR '96, 1996 IEEE Computer Society Conference on Computer Vision and Pattern Recognition, 1996*, pages 245–251. IEEE. 3.1.1.2
- Thodberg, H. H. (2003). Minimum description length shape and appearance models. In Taylor, C. and Noble, J. A., editors, *Information Processing in Medical Imaging*, volume 2732 of *LNCS*, pages 51–62, Berlin, Heidelberg. Springer Berlin Heidelberg. 2.2.3, 4.1.3.2
- Thompson, D. (1917). *On Growth and Form*. The University Press, Cambridge, first edition. Revised ed., 1942. Abridged ed., 1961. 2.2

- Thompson, P. M., Hayashi, K. M., Zubicaray, G. I. D., Janke, A. L., Rose, S. E., Semple, J., Hong, M. S., Herman, D. H., Gravano, D., Doddrell, D. M., and Toga, A. W. (2004). Mapping hippocampal and ventricular change in Alzheimer disease. *NeuroImage*, 22(4):1754–1766. 1.1.3.2, 1.1.3.2, 2.3.2
- Tibshirani, R. (1996). Regression shrinkage and selection via the Lasso. *Journal of the Royal Statistical Society. Series B (Methodological)*, 58(1):267–288. 3.3.2
- Tomlinson, B. E., Blessed, G., and Roth, M. (1968). Observations on the brains of non-demented old people. *Journal of the Neurological Sciences*, 7(2):331–356. 1.1.1
- Tomlinson, B. E., Blessed, G., and Roth, M. (1970). Observations on the brains of demented old people. *Journal of the Neurological Sciences*, 11(3):205–242. 1.1.1
- Tsagaan, B., Shimizu, A., Kobatake, H., and Miyakawa, K. (2002). An automated segmentation method of kidney using statistical information. In Dohi, T. and Kikinis, R., editors, *Medical Image Computing and Computer-Assisted Intervention — MICCAI 2002*, volume 2488 of *LNCS*, pages 556–563, Berlin, Heidelberg. Springer Berlin Heidelberg. 2.2.1
- Tsagaan, B., Shimizu, A., Kobatake, H., Miyakawa, K., and Hanzawa, Y. (2001). Segmentation of kidney by using a deformable model. In *2001 International Conference on Image Processing, 2001. Proceedings*, volume 3, pages 1059–1062 vol.3. IEEE. 2.2.1
- Tsai, A., Yezzi, A., Wells, W., Tempany, C., Tucker, D., Fan, A., Grimson, W. E., and Willsky, A. (2003). A shape-based approach to the segmentation of medical imagery using level sets. *IEEE Transactions on Medical Imaging*, 22(2):137–154. 2.2.1
- Twining, C. J. and Taylor, C. J. (2001). Kernel principal component analysis and the construction of non-linear active shape models. In *IN PROC. BMVC*, pages 23–32. 2.2.4

- Tzourio-Mazoyer, N., Landeau, B., Papathanassiou, D., Crivello, F., Etard, O., Delcroix, N., Mazoyer, B., and Joliot, M. (2002). Automated anatomical labeling of activations in SPM using a macroscopic anatomical parcellation of the MNI MRI Single-Subject brain. *NeuroImage*, 15(1):273–289. 2.1.1
- Üzümcü, M., Frangi, A. F., Sonka, M., Reiber, J. H. C., and Lelieveldt, B. P. F. (2003). ICA vs. PCA active appearance models: Application to cardiac MR segmentation. In Ellis, R. E. and Peters, T. M., editors, *Medical Image Computing and Computer-Assisted Intervention - MICCAI 2003*, volume 2878 of *LNCS*, pages 451–458, Berlin, Heidelberg. Springer Berlin Heidelberg. 2.2.4
- van der Flier, W. M., van Straaten, E. C. W., Barkhof, F., Ferro, J. M., Pantoni, L., Basile, A. M., Inzitari, D., Erkinjuntti, T., Wahlund, L. O., Rostrup, E., Schmidt, R., Fazekas, F., and Scheltens, P. (2005). Medial temporal lobe atrophy and white matter hyperintensities are associated with mild cognitive deficits in non-disabled elderly people: the LADIS study. *Journal of Neurology, Neurosurgery & Psychiatry*, 76(11):1497–1500. 1.1.3.2
- van der Lijn, F., den Heijer, T., Breteler, M. M., and Niessen, W. J. (2008). Hippocampus segmentation in MR images using atlas registration, voxel classification, and graph cuts. *NeuroImage*, 43(4):708–720. 2.1.2.3
- van Rikxoort, E. M., Isgum, I., Arzhaeva, Y., Staring, M., Klein, S., Viergever, M. A., Pluim, J. P., and van Ginneken, B. (2010). Adaptive local multi-atlas segmentation: Application to the heart and the caudate nucleus. *Medical Image Analysis*, 14(1):39–49. 2.1.2.3
- Vapnik, V. (1995). *The Nature of Statistical Learning Theory*. Springer. 5.3
- Vemuri, P., Gunter, J. L., Senjem, M. L., Whitwell, J. L., Kantarci, K., Knopman, D. S., Boeve, B. F., Petersen, R. C., and Jr., C. R. J. (2008a). Alzheimer’s disease diagnosis in individual subjects using structural MR images: Validation studies. *NeuroImage*, 39(3):1186–1197. 5.3
- Vemuri, P., Whitwell, J. L., Kantarci, K., Josephs, K. A., Parisi, J. E., Shiung, M. S., Knopman, D. S., Boeve, B. F., Petersen, R. C., Dickson, D. W., and

- Jack, Clifford R, J. (2008b). Antemortem MRI based STructural abnormality iNDex (STAND)-scores correlate with postmortem braak neurofibrillary tangle stage. *NeuroImage*, 42(2):559–567. 1.1.3.2
- Vemuri, P., Wiste, H. J., Weigand, S. D., Shaw, L. M., Trojanowski, J. Q., Weiner, M. W., Knopman, D. S., Petersen, R. C., Jack, C. R., and the Alzheimer’s Disease Neuroimaging Initiative (2009). MRI and CSF biomarkers in normal, MCI, and AD subjects. *Neurology*, 73(4):294–301. 1.1.3.2
- Vercauteren, T., Pennec, X., Perchant, A., and Ayache, N. (2007). Non-parametric diffeomorphic image registration with the demons algorithm. In Ayache, N., Ourselin, S., and Maeder, A., editors, *Medical Image Computing and Computer-Assisted Intervention – MICCAI 2007*, volume 4792 of *LNCS*, pages 319–326, Berlin, Heidelberg. Springer Berlin Heidelberg. 3.1.1.2, 3.4.2.2
- Vercauteren, T., Pennec, X., Perchant, A., and Ayache, N. (2009). Diffeomorphic demons: Efficient non-parametric image registration. *NeuroImage*, 45(1, Supplement 1):S61–S72. 2.1.2.3, 3.1.1.2, 5.3
- Vermaak, J. and Perez, P. (2003). Constrained subspace modeling. In *Computer Vision and Pattern Recognition, 2003. Proceedings. 2003 IEEE Computer Society Conference on*, volume 2, pages 106–113. 2.3.2
- Villemagne, V. L., Rowe, C. C., Macfarlane, S., Novakovic, K. E., and Masters, C. L. (2005). Imaginem oblivionis: the prospects of neuroimaging for early detection of Alzheimer’s disease,. *Journal of Clinical Neuroscience*, 12(3):221–230. 1.1.3
- Viola, P. and Wells, W. M. (1995). Alignment by maximization of mutual information. In , *Fifth International Conference on Computer Vision, 1995. Proceedings*, pages 16–23. IEEE. 3.1.2
- Vitali, P., Migliaccio, R., Agosta, F., Rosen, H. J., and Geschwind, M. D. (2008). Neuroimaging in dementia. *Seminars in Neurology*, 28(4):467–483. 1.1.3

- Vos, F. M., de Bruin, P. W., Aubel, J. G., Streekstra, G. J., Maas, M., van Vliet, L. J., and Vossepoel, A. M. (2004). A statistical shape model without using landmarks. In *Proceedings of the 17th International Conference on Pattern Recognition, 2004. ICPR 2004*, volume 3, pages 714–717 Vol.3. IEEE. 2.2.3
- Walhovd, K., Fjell, A., Dale, A., McEvoy, L., Brewer, J., Karow, D., Salmon, D., and Fennema-Notestine, C. (2010). Multi-modal imaging predicts memory performance in normal aging and cognitive decline. *Neurobiology of Aging*, 31(7):1107–1121. 1.1.3.2
- Walsh, D. M. and Selkoe, D. J. (2004). Deciphering the molecular basis of memory failure in Alzheimer’s disease. *Neuron*, 44(1):181–193. 1.1.2
- Wang, H., Das, S. R., Suh, J. W., Altinay, M., Pluta, J., Craige, C., Avants, B., and Yushkevich, P. A. (2011). A learning-based wrapper method to correct systematic errors in automatic image segmentation: Consistently improved performance in hippocampus, cortex and brain segmentation. *NeuroImage*, 55(3):968–985. 2.1.2
- Wang, L., Miller, J. P., Gado, M. H., McKeel, D. W., Rothermich, M., Miller, M. I., Morris, J. C., and Csernansky, J. G. (2006). Abnormalities of hippocampal surface structure in very mild dementia of the Alzheimer type. *NeuroImage*, 30(1):52–60. 2.3.2
- Wang, L., Swank, J. S., Glick, I. E., Gado, M. H., Miller, M. I., Morris, J. C., and Csernansky, J. G. (2003). Changes in hippocampal volume and shape across time distinguish dementia of the Alzheimer type from healthy aging. *NeuroImage*, 20(2):667–682. 2.3.2
- Warfield, S., Zou, K., and Wells, W. (2004). Simultaneous truth and performance level estimation (STAPLE): an algorithm for the validation of image segmentation. *Medical Imaging, IEEE Transactions on*, 23(7):903–921. 2.1.2.3

- Watson, C., Andermann, F., Gloor, P., Jones-Gotman, M., Peters, T., Evans, A., Olivier, A., Melanson, D., and Leroux, G. (1992). Anatomic basis of amygdaloid and hippocampal volume measurement by magnetic resonance imaging. *Neurology*, 42(9):1743–1750. 2.1.1
- Weistrand, O. (2005). *Global Shape Description of Digital Objects*. PhD thesis, Uppsala University, Uppsala. 4.1.1.2
- West, M. J., Coleman, P. D., Flood, D. G., and Troncoso, J. C. (1994). Differences in the pattern of hippocampal neuronal loss in normal ageing and Alzheimer’s disease. *The Lancet*, 344(8925):769–772. 2.3.2
- Whitwell, J. L., Josephs, K. A., Murray, M. E., Kantarci, K., Przybelski, S. A., Weigand, S. D., Vemuri, P., Senjem, M. L., Parisi, J. E., Knopman, D. S., Boeve, B. F., Petersen, R. C., Dickson, D. W., and Jack, C. R. (2008). MRI correlates of neurofibrillary tangle pathology at autopsy. *Neurology*, 71(10):743–749. 1.1.3.2
- Wimo, A. and Prince, M. (2010). World Alzheimer report 2010: The global economic impact of dementia. 1.1.1
- Wolz, R., Aljabar, P., Hajnal, J. V., Hammers, A., and Rueckert, D. (2010). LEAP: learning embeddings for atlas propagation. *NeuroImage*, 49(2):1316–1325. 2.1.2.3
- Wolz, R., Aljabar, P., Rueckert, D., Heckemann, R. A., and Hammers, A. (2009). Segmentation of subcortical structures and the hippocampus in brain MRI using graph-cuts and subject-specific a-priori information. In *IEEE International Symposium on Biomedical Imaging, 2009 – ISBI ’09*, pages 470–473. IEEE. 2.1.2.3
- Woods, R. P., Grafton, S. T., Holmes, C. J., Cherry, S. R., and Mazziotta, J. C. (1998). Automated image registration: I. general methods and intra-subject, intramodality validation. *Journal of Computer Assisted Tomography*, 22(1):139–152. 2.1.2.3

- Woolrich, M. W., Jbabdi, S., Patenaude, B., Chappell, M., Makni, S., Behrens, T., Beckmann, C., Jenkinson, M., and Smith, S. M. (2009). Bayesian analysis of neuroimaging data in FSL. *NeuroImage*, 45(1, Supplement 1):S173–S186. 2.1.2.2
- Xie, J., Alcantara, D., Amenta, N., Fletcher, E., Martinez, O., Persianinova, M., DeCarli, C., and Carmichael, O. (2009). Spatially localized hippocampal shape analysis in late-life cognitive decline. *Hippocampus*, 19(6):526–532. 2.3.2, 5.1
- Yang, J. and Duncan, J. S. (2004). 3D image segmentation of deformable objects with joint shape-intensity prior models using level sets. *Medical Image Analysis*, 8(3):285–294. 2.1.2.2
- Yang, J., Staib, L. H., and Duncan, J. S. (2004). Neighbor-constrained segmentation with level set based 3-D deformable models. *IEEE Transactions on Medical Imaging*, 23(8):940–948. 2.1.2.2
- Yassa, M. A. and Stark, C. E. (2009). A quantitative evaluation of cross-participant registration techniques for MRI studies of the medial temporal lobe. *NeuroImage*, 44(2):319–327. 2.1.2.3, 3.1.1.2
- Yavuz, B. B., Ariogul, S., Cankurtaran, M., Oguz, K. K., Halil, M., Dagli, N., and Cankurtaran, E. S. (2007). Hippocampal atrophy correlates with the severity of cognitive decline. *International Psychogeriatrics*, 19(04):767–777. 2.3.1
- Yuan, Y., Gu, Z., and Wei, W. (2009). Fluorodeoxyglucose-positron-emission tomography, single-photon emission tomography, and structural MR imaging for prediction of rapid conversion to Alzheimer disease in patients with mild cognitive impairment: A meta-analysis. *AJNR Am J Neuroradiol*, 30(2):404–410. 1.1.3.2
- Yushkevich, P., Joshi, S., Pizer, S. M., and ad Lei E. Wang, J. G. C. (2003a). Feature selection for shape-based classification of biological objects. In *Information Processing in Medical Imaging*, pages 114–125. Springer-Verlag. 2.3.2

- Yushkevich, P., Thomas Fletcher, P., Joshi, S., Thall, A., and Pizer, S. M. (2003b). Continuous medial representations for geometric object modeling in 2D and 3D. *Image and Vision Computing*, 21(1):17–27. 2.2.1
- Yushkevich, P. A., Piven, J., Cody Hazlett, H., Gimpel Smith, R., Ho, S., Gee, J. C., and Gerig, G. (2006). User-guided 3D active contour segmentation of anatomical structures: Significantly improved efficiency and reliability. *Neuroimage*, 31(3):1116–1128. 2.1
- Zhang, Z. (1994). Iterative point matching for registration of free-form curves and surfaces. *International Journal of Computer Vision*, 13(2):119–152. 2.2.2
- Zhou, L., Lieby, P., Barnes, N., Réglade-Meslin, C., Walker, J., Cherbuin, N., and Hartley, R. (2009). Hippocampal shape analysis for Alzheimer’s disease using an efficient hypothesis test and regularized discriminative deformation. *Hippocampus*, 19(6):533–540. 2.3.2
- Zhou, L., Wang, L., Shen, C., and Barnes, N. (2010). Hippocampal shape classification using redundancy constrained feature selection. In Jiang, T., Navab, N., Pluim, J. P., and Viergever, M. A., editors, *Medical Image Computing and Computer-Assisted Intervention – MICCAI 2010*, volume 6362 of *LNCS*, pages 266–273. Springer. 2.3.2